University of Szeged

Albert Szent-Györgyi Medical School

Doctoral School of Multidisciplinary Medical Science

Developing integrated optical structures, with special respect to applications in medical diagnostics

Ph.D. Thesis

Dániel Petrovszki

Supervisors:

András Dér PhD, DSc; scientific advisor

Sándor Valkai PhD; research associate

Biological Research Centre

Institute of Biophysics

Biomolecular Electronics Research Group

Szeged

2023

List of publications

List of papers directly related to the subject of the thesis

I. **Petrovszki D,** Valkai S, Gora E, Tanner M, Bányai A, Fürjes P, & Dér A. An integrated electro-optical biosensor system for rapid, low-cost detection of bacteria. Microelectronic Engineering. 2021; 239,111523. IF: 2.662

II. **Petrovszki D*,** Krekic S*, Valkai, S, Heiner Z, & Dér A. All-Optical Switching Demonstrated with Photoactive Yellow Protein Films. Biosensors. 2021; 11(11),432. IF: 5.743

III. **Petrovszki D*,** Walter FR*, Vigh JP, Kocsis A, Valkai S, Deli MA, & Dér A. Penetration of the SARS-CoV-2 Spike Protein across the Blood–Brain Barrier, as Revealed by a Combination of a Human Cell Culture Model System and Optical Biosensing. Biomedicines. 2022; 10(1), 188. IF: 4.757

Total cumulative impact factor: 13.162

Table of contents

List of abbreviations

AC - alternating current

BBB - blood-brain barrier

BSA - bovine serum albumin

C - cover

Caco-2 - intestinal colon carcinoma derived epithelial cell line

CAD/CAM - computer aided design / manufacturing

CCD - charge coupled device

CFU - colony forming unit

CM - Clausius-Mossotti (factor)

CMOS - complementary metal-oxide semiconductor

COVID-19 - coronavirus disease 2019

DC - direct current

DEP - dielectrophoresis

DLW - direct laser writing

DMEM - Dulbecco's modified Eagle medium

E. coli - Escherichia coli

EIS - electrochemical impedance spectroscopy

ELISA - enzyme-linked immunosorbent assay

FBS - fetal bovine serum

G - guide (waveguide)

hEC - human umbilical cord stem cell-derived endothelial cell

HEPES - 4-(2-hydroxyethyl)-1-piperazineethanesulfonic acid

IC - integrated circuit

IO - integrated optics

LB - lysogeny broth

LOC - lab-on-a-chip

LOD - limit of detection

MERS - Middle East respiratory syndrome

MSE - mean square error

MZI - Mach-Zehnder interferometer

nDEP - negative dielectrophoresis

NLO - non-linear optics

OWLS - optical waveguide lightmode spectroscopy

PBS - phosphate-buffer saline

PC - bovine brain pericyte

PCR - polymerase chain reaction

pDEP - positive dielectrophoresis

PDMS - polydimethylsiloxane

PIC - photonic integrated circuit

PMT - photo multitube

POC - point-of-care

RH - Ringer–HEPES

S - substrate

SARS - severe acute respiratory syndrome

SARS-CoV-2 - severe acute respiratory syndrome coronavirus 2

SPR - surface plasmon resonance

TBS - tris-buffered saline

TE - transversal electric mode

TEER - trans-endothelial/epithelial electrical resistance

TIR - total internal reflection

TM - transversal magnetic mode

TRIS-HCl - tris(hydroxymethyl)aminomethane hydrochloride

UV - ultraviolet

Summary

In recent years, biosensors have been constantly developed for many purposes, in addition to pregnancy tests and blood glucose meters that are in common use. The importance of their application in medical diagnostics has also been demonstrated even since the global pandemic of the COVID-19 coronavirus disease. In this context, biosensors could play an important role as rapid point-of-care and 'on-site' tests, owing to their potential for rapid, sensitive, selective, and potentially label-free pathogen detection. Therefore, these devices provide a feasible and affordable alternative to traditional laboratory diagnostic techniques, even in rural environments, which is a key to both disease suppression and to early diagnosis and thus enabling early treatment. For such applications, label-free optical biosensors are suitable, which integrated optical form enables the pathogen detection in the desired miniaturized, portable, and sensitive way. The common operation principle among such devices is based on evanescent-field sensing, where the changes in the surroundings of the applied waveguiding structure can be detected. In my PhD studies, the aim was to create biosensors for pathogen detection from fluid samples via evanescent field, using polymer waveguide stripes designed and fabricated on glass substrates, in a combination with an integrated microfluidic channel.

As first application, an electro-optical biosensor was created for label-free, rapid, selective, and sensitive detection of living, non-virulent *Escherichia coli* bacteria in body fluids. The proof-of-concept detection technique included an initial dielectrophoretic (DEP) target-cell collection process, followed by the detection of these captured cells via the evanescent waves of light propagating in a multimode waveguide, and scattered by the bacteria. The quantitative measurements were based on changes of the scattered light pattern, related to bacteria movement in the detection region because of an external electrical stimulus. These changes were proved to be significant even when using objectives of moderate magnification (x10, x4.7). Thus, this method provides a possible cell detection method with low-cost cameras. The results were evaluated based on image processing approaches. The optimal frequency parameter of the alternating (AC) electric field applied for DEP-based cell collection was also determined. The practical usability of the biosensor is characterized by its limit of detection (LOD), which in this case was estimated to be ca. 10^2 CFU/ml bacteria concentration. This value is relevant for the concentration of typical pathogens in body fluids, e.g., urine. Although the biosensor was primarily used for non-specific detection of bacteria, the feasibility of size-selective detection by DEP-based cell collection was proven in several cases, which cell-collection method could be used in other high-sensitivity integrated optical sensor devices, as well. Based

on the operation principle and the design of this biosensor, the detection could be carried out rapidly, with fast detection time of about 10 minutes. Based on the demonstration of this proof-of-concept detection method, this biosensor design has some promising aspects regarding its sensitivity, low cost of fabrication, and rapid detection process. These could all contribute to its application as a point-of-care diagnostic test in the future.

For the second application of integrated optical structures, a miniature Mach-Zehnder interferometer (MZI)-based biosensor was made, providing rapid and sensitive detection of biological particles. Due to these favorable properties, the device was developed and applied for specific viral protein sensing, as part of a recent study carried out in collaboration with the members of the Biological Barriers Research Group of our institute. The topic is related to the neuroinvasion of severe acute respiratory syndrome coronavirus 2 (SARS-CoV-2), focusing on its surface spike protein's S1 subunit. This protein could circulate during infection and could possibly cross the blood-brain barrier (BBB) when reaching the brain, which was demonstrated with mice. Moreover, several gastrointestinal symptoms are associated with this disease, thus an intestinal barrier was also investigated. The medical relevance of the spike protein passage through biological barriers is of high importance. In the mentioned study, the penetration capability of the S1 subunit across biological barriers exposed to the infection, namely BBB and intestinal ones, was investigated. For this purpose, *in vitro* cell culture models of these barriers were used in a permeability assay. Then, the verification of the barrier-crossing of the protein was quantitatively measured with the integrated optical biosensor and an alternative traditional enzyme linked immunosorbent assay (ELISA). The specific detection of the amount of the barrier-crossed protein was performed by the biofunctionalization of the surface of the waveguide, used for the measuring arm of the interferometer. Prior to these measurements, the operating point of the interferometer was set to reach optimal, stable detection. For this purpose, a gold heater surface-structure was deposited near the interferometer reference arm, which resulted a change in the refractive index of the medium surrounding the waveguide via temperature modulation. The measurements with the biosensor provided accurate determination of the amount of S1 protein that passed through the barrier systems. Furthermore, it was established that the S1 protein could pass through the two types of barriers in different amounts. The results of the experiments with the biosensor were in agreement with the results of conventional immunological tests (ELISA) carried out in parallel. These findings can be valuable for further studies related to the pathological effects of SARS-CoV-2 on the human body. With the biosensor, the measurements took a few minutes, showing the applicability of this interferometric biosensing approach for such diagnostic purposes.

1. Introduction

1.1. Biosensors in point-of-care diagnostics

Biosensors have been part of the medical diagnostic toolbox since the middle of the last century. The first pioneering device was the development of an enzyme electrode. Since then, the field of biosensors has evolved enormously. Since the end of the last century, such devices have been in everyday use and have become dominant, whether we are talking about a disposable pregnancy test or a blood glucose meter. The progress is even more noticeable today, with applications in the food industry, water management, quality control and environmental monitoring against pollution, in addition to medical diagnostics [1]. Not surprisingly, since the 1990s, the number of scientific publications related to the term 'biosensor' has shown a quasi-exponential increase on PubMed [2]. This evolution is further confirmed by the number of biosensors that have been widely used in industry in recent years [3].

The purpose of biosensors is to detect an analyte, involved in a biological or biochemical reaction, using a given biological recognition element, providing a signal proportional to its concentration in the sample. This recognition can be reached selectively, specifically, and rapidly by means of different binding sites (e.g., immunological antigen antibody, or biochemical enzyme substrate, or receptor analyte). The generated signal is then converted by a transducer, and subsequently processed and detected. This process can be optical, electrical, magnetic, or mass-based, with the output being, for example, a color change or an electrical signal. These devices may also use labeling for their operation, such as nanodots or fluorophores. However, their label-free versions may also have a sufficiently high sensitivity and ensure cost-effective operation [4].

The clinical diagnostic use of these devices can in some cases provide an alternative in point-of-care testing (POC), facilitating the initiation of appropriate therapeutic treatment. There is a great need for it, as conventionally used, highly sensitive and specific microbiological cell-culture and immunoassays require laboratory conditions, a relatively large amount of time and trained staff. These techniques include, for example, polymerase chain reaction (PCR)-based procedures and various types of enzyme-linked immunosorbent assays (ELISAs). For a diagnostic tool to be used for POC testing, it must meet several requirements. The World Health Organization has determined these, so-called ASSURED criteria: affordable, sensitive, specific, user-friendly, rapid, and robust, equipment-free, and deliverable to end-users. These characteristics also apply to the diagnostic use of biosensors. These devices, in addition to the

selective and specific detection provided by biorecognition elements, also include fast and sensitive operation and reproducibility. The sensitivity of the biosensors, as one of their key features, can be characterized by the limit of detection (LOD). This describes the minimum reliable change in the parameter used to determine the analyte concentration during detection [4–6].

To implement all these features in a portable, easy-to-use and highly sensitive single chip platform, biosensors can be incorporated in lab-on-a-chip (LOC) devices for label-free and real-time 'on-chip' analysis. For the practical POC application of such miniature LOC systems, they must bear several functionalities. These involve handling of the target fluid, sample preparation (e.g., its filtration, homogenization, dilution, etc.), and the tasks related to biosensors, namely target detection and signal processing. For this purpose, microfluidic channels of reduced dimensions and volumes can be used, providing performance improvement of the whole LOC platform. Therefore, biological fluids of less volume, e.g., a drop of blood, that is commonly used for traditional laboratory tests, can be handled and analyzed. Due to the above-mentioned properties of LOCs, a wide range of such fast and efficient analytical platforms has been developed for the application as diagnostic tools during the recent years [7–10].

Biosensors can perform detection in different ways. In this context, one basis for differentiation can be whether labeling is used in the process of operating the device. Labeling techniques may use optical, radioactive, or magnetic markers, such as fluorophores or nanoparticles. The chemical procedure, required for their application, takes cost and time in a laboratory-intensive environment. Consequently, beside these techniques can achieve high sensitivity, the label-free versions can also perform their task at lower cost and with sufficient sensitivity [11,12]. Another basis of biosensor differentiation is based on the applied transducer, thus there are also optical, electrical, electrochemical, or magnetic devices[4].

Among the many label-free designs, electrical signal detection in electrochemical devices make up a large proportion of biosensors, alongside optical ones. Detection by these sensors can be based on amperometry, voltammetry, potentiometry, conductometry, or the most widely used electrochemical impedance spectroscopy (EIS). For this purpose, surface microelectrode systems are used in various layouts in a miniaturized form to ensure portability. In case of impedimetric biosensors, the impedance of the electrodes changes due to capturing target cells on their surface. Such devices could usefully assist clinical diagnostics. In this context, for example, many disease-indicator protein biomarkers can be measured from fluid samples with high accuracy [13]. Furthermore, the simplicity and adaptability of impedimetric detection allow the detection of many pathogens by EIS [14].

In addition to electrical signal-based sensing, optical biosensors are currently also prominent in POC diagnostic applications. This is due to the high sensitivity, selectivity, and real-time monitoring capabilities of these devices. Optical detection can be based on a change in a particular property of light, e.g., intensity, phase, resonance frequency. Currently, in a POC application-oriented way, the development of label-free, integrated optical construction is prevalent [4].

1.2. Integrated optics

In the second half of the 20th century, the demand for the miniaturization of optical systems was brought to life by the growing demand for information processing. The units of telecommunication systems implemented by traditional integrated circuits are provided by the transistor. Moore's law, which predicts an exponential increase in their number, is no longer fully applicable in the past decades. The need for high-speed signal transmission and signal processing in telecommunications encouraged the creation of analog systems with integrated circuits (IC). As a result, such systems were created in which, instead of electrons, light – with its intrinsic faster propagation speed – carries the information. In this way, photonic integrated circuits (PICs) have been created, which technology realizes the generation, transmission, and processing of light. In practice, it is necessary to implement them in a compact and miniaturized form on a single chip, applying the technology of integrated optics (IO). Notably, further technological advances are required for developing all-optical systems for practical use, thus only hybrid (opto-electronic) systems with electronic signal generation and processing have been realized, so far. In parallel, regarding the label-free POC diagnostic application of optical biosensors, their integrated optical (IO) constructions have been widely investigated due to the advantages provided by this technology (for more details see 1.3. section). In this context, such IO biosensor devices can offer possible label-free methods for biological particle detection with high sensitivity, realized in a miniaturized and mechanical stable platform. Additionally, due to the design of such IO structures, the fabrication of these optical biosensors can be performed by the commonly used complementary metal-oxide semiconductor (CMOS) technology, allowing their mass production. Last, but not least, the vast majority of the recently developed integrated optical biosensors perform evanescent-field detection, which is based on the intrinsic feature of such IO systems (see more details in 1.2.2. section). These label-free integrated optical devices are also surveyed later (1.3. section) [4,15,16].

1.2.1. Optical waveguide theory

To understand the working principle of the integrated optical biosensors as promising candidates for label-free POC testing applications, first the characteristic features of light propagation in these structures are needed to be described. In integrated optical circuits, light is confined as a 'guided-wave' by optical waveguide structures, also known as 'dielectric' waveguides. In practice, optical fibers are the most widely used, cylindrical waveguide constructions as telecommunication signal transmitters. In contrast, in IO systems the focus is on planar structures, which can be realized on a single chip supporting the aim of the miniaturization [17].

The simplest model for describing the theory of optical waveguiding is provided by the construction of the planar slab waveguide, shown in Figure 1 with the directions (x, y, z). In this system, light propagates in the dielectric layer of the waveguide (G) by total internal reflections (TIR) from the boundaries with substrate (S), on which it is located, and with a cover layer (C). As the geometrical optics theory states, the basic condition for reaching TIR, the refractive index of the guide (n_g) must be greater than that of the surrounding media ($n_s < n_g > n_c$) at the wavelength (λ_0) of the light coupled to the waveguide. In case of a three-layer slab waveguide construction, the extension of the waveguide could be considered semi-infinite in the plane (y-z) parallel to the direction of the light propagation in the guide. Meanwhile, in IO systems the wavelength of the applied light is comparable with the thickness of the guiding layer (t_g) in the x direction, perpendicular to the y-z plane, which is typically in the micron scale. In this regime, in contrast to the geometrical optics theory, the continuous TIRs lead to interferences of the propagating light waves in the waveguide. This phenomenon limits the number of waves being able to propagate in the waveguide. To achieve the guiding of the light waves in such a structure, the interference must be constructive, which is called the self-consistency criterion. It lays the basics of the 'zig-zag' model of the propagating light in such systems [17]. In other words, the phase of the traveling wave must remain in phase with itself after double TIRs. Moreover, based on the criterion of TIRs, defined by Snell's law, light waves with discrete incident angles, relative to the normal to the interfaces, could propagate in the guiding layer. In that case, the above-mentioned angles must exceed the corresponding critical angles (θ_c) for each interface [4]:

$$\theta = \sin^{-1}\left(\frac{n_{s,c}}{n_g}\right) \qquad\qquad (Eq.1.)$$

where θ is the angle of incidence (direction of the propagation), $n_{s,c}$ and n_g are the refractive indices of the corresponding surrounding medium and the guiding layer, respectively. In contrast, for coupling light into the waveguide, the coupling angle must be lower than a discrete value (θ_{in}), otherwise the guiding could not take place and the incident light radiates to the surrounding media.
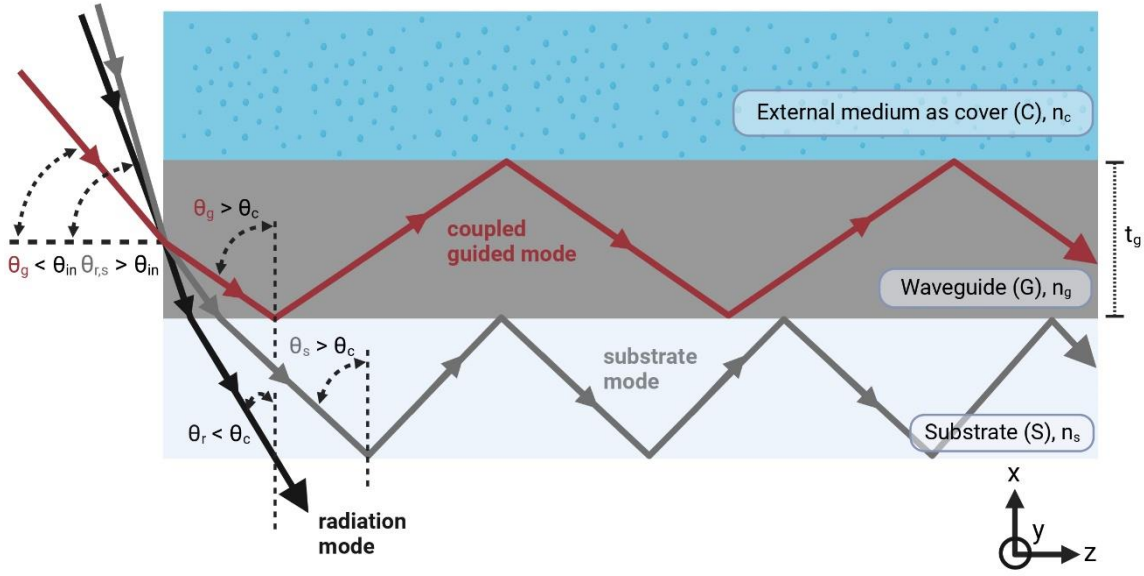

Figure 1. Schematic illustration of optical wave coupling to a slab waveguide with the light propagation in it. The incident angle of the guiding light, relative to the direction of the propagation (z), must be less than a discrete angle (θ_{in}) for its efficient incoupling to the slab waveguide with t_g thickness. Then the light mode could be guided by total internal reflections (TIRs) in the slab. Based on Snell's law, the regarding incident angle must be greater than a critical angle (θ_c), defined by the refractive indices of the corresponding media ($n_s < n_g > n_c$). Otherwise, depending on the coupling angles, the light could be confined in the substrate as a substrate mode (θ_s), and also it could radiate out of the system (θ_r). The figure was created with Biorender.com, adapted from a figure of a recent study [4].

Due to the self-consistency, only a discrete set of waveguiding states exist in such planar waveguide systems. These are called the modes of propagation. Based on these boundary conditions and the Maxwell equations in case of such dielectric layers of a slab waveguide [4], the optical waveguiding and the modes can be further characterized. Applying the zig-zag model, the light propagates in the z direction, while it is confined (t_g) in the transverse direction (x). Both the light and the waveguide can be considered uniform. The light waves are coherent and monochromatic, which can be characterized by a wavevector **k**$*n_g$, describing its propagation in the direction of the wave normal. The absolute value of **k** is:

$$k = \frac{2 \cdot \pi}{\lambda_0} = \frac{\omega}{c_0} \qquad \text{(Eq.2.)}$$

where ω is the angular frequency, λ_0 and c_0 are the wavelength and velocity of light in vacuum. Due to the zig-zag propagation of a wave in the guide, the tangential component of **k** (k_t) must be continuous across an interface based on Snell's law. Consequently, it can be described by a value, by the effective refractive index (N), which equals to k_t/k for planar waveguides, and it is between the indices of the waveguide and the surrounding media (n_s, $n_c < N < n_g$). k_t is also called propagation constant (β):

$$\beta = \frac{\omega}{v_p} = k \cdot n_g \cdot \sin \theta \qquad \text{(Eq.3.)}$$

where v_p is the related phase velocity. This connection shows the angle dependency of the self-consistent propagation. Regarding the self-consistency, because of the constructive interference, the phase shift due to the reflections must be an integer of the multiple of 2π. This condition can be described, taking the above-mentioned light propagation properties into consideration, giving the mode equation:

$$2 \cdot k \cdot n_g \cdot t_g \cdot \cos \theta - 2 \cdot \phi_{s,g} - 2 \cdot \phi_{g,c} = 2 \cdot \pi \cdot m \qquad \text{(Eq.4.)}$$

where $\phi_{s,g}$ and $\phi_{g,c}$ are the phase shifts resulting from the reflections from each interface, which is a function of the corresponding θ angles, as (Eq.1.) describes, and m refers to the order of the modes (0, 1, 2, …). In planar waveguides, modes with only two polarizations can be excited, based on the plane wave solutions of Maxwell equations for these structures. This leads to two orthogonal sets of functions, where even the total electric or total magnetic field oscillates in the plane of the interfaces. Therefore, modes can be divided into transversal electric (TE) and transversal magnetic (TM) at an order (eg. the zeroth order TE_0, TM_0, and first order TE_1, TM_1 and so on). The order of the modes starts with zero, and it refers to the wavefronts of the corresponding electromagnetic-field distribution profiles in the cross-section in the guide (Figure 3a) [18]. As it is depicted in Eq.4., the number of modes, which propagation is supported by the waveguide, depends on the thickness of the guiding layer (t_g), as well. The guiding of modes of an order (e.g., the 0th fundamental TE and TM) can only take place, if that thickness is greater than the corresponding minimum or so-called 'cut-off' value. If that value is only slightly larger than the cut-off thickness at a given wavelength, only fundamental modes can propagate. In this case, we can talk about single mode waveguides. In other cases, where thicker guides are considered, multiple modes can be guided in multimode waveguides. With

decreasing t_g, and refractive index contrast between substrate and guide, and with increasing wavelength, the number of guided modes decreases. Therefore, the opposite is also true, in case of a light with a frequency lower than the cut-off frequency given by the geometry and the material of the waveguide, it cannot propagate in the waveguide [4,17,19,20].

If the waveguide structure does not fulfill the above-mentioned requirements, various undesired modes can be observed. These could even propagate in the substrate layer, as a substrate mode, or radiate and could be coupled out of the system and travel in the surrounding media, as a radiation mode (Figure 1) [17].

The waveguiding theory can be extended to further rectangular and planar waveguide structures, as well. Consequently, a wide range of these constructions have been utilized as passive elements in IO systems for transmitting information coded by light. Beside the slab waveguide detailed above, there can be found the 'rib' and 'ridge' structures, fabricated on a substrate. In contrast, there are ones, especially 'buried' and 'strip-loaded' where the guide is embedded in the substrate. Nevertheless, the list of the mentioned designs represents only the main types, besides these, many more have been designed and used in various applications [4,17].
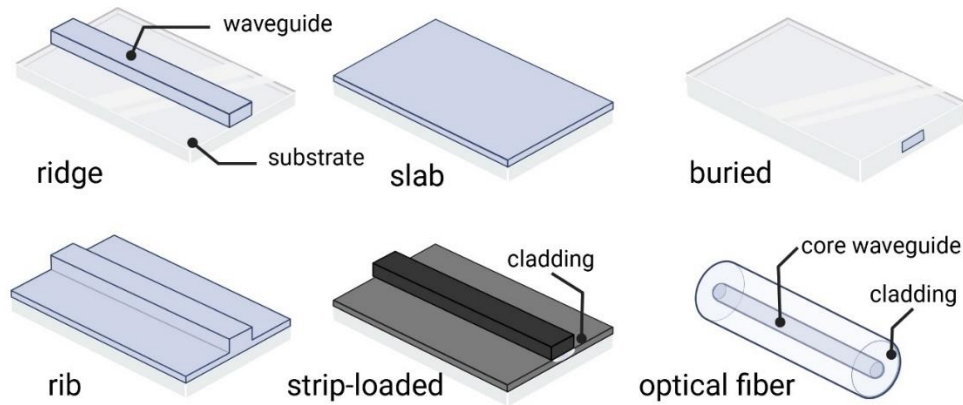

Figure 2. Schematic illustration of different waveguide types and the optical fiber. The figure was created in Biorender.com, adapted from a figure of a recent study [4].

Such waveguides can be made up of various materials, which determines the transmission spectra of the guided light, thus their application even in visible and near infrared wavelengths. Therefore, glass, silicon, e.g., Si, Si_3N4, SiON; polymer, or III-V compounds or lithium-niobate structures can be realized [21].

The above-mentioned perspectives are necessary to be considered, along with the wavelength of the transmitted light, for designing integrated optical waveguide structures. Consequently, IO systems for various applications ranging from telecommunication, biosensing and quantum communication can be realized [4,17].

1.2.2. Evanescent field

The light propagates in the waveguide by TIRs, following the above-described 'zig-zag' model, where the flow of its energy, as electromagnetic field distribution, can be examined from a wave-optical point of view. From this perspective, it is shown that the light suffers a lateral shift (Goos-Hänchen shift) compared to the incident ray when it is reflected from the boundary of the 'dielectric' waveguide. This phenomenon indicates that the light ray can penetrate the adjacent medium before its reflection. Meanwhile, the light intensity shows a gradual attenuation perpendicular to its direction of propagation (x in Figure 1) in the medium, starting from the interface (Figure 3). This decay shows an exponential trend regarding the power of the electric field (Figure 3). Therefore, such waves in the near-field from the boundaries of the guide, are called evanescent waves, and the field, in which they are located, is the evanescent field. The extension of this field can be described by the penetration depth (d_p). This is defined by the distance from the interface of the guiding layer and the adjacent medium, where the electric field intensity is decayed to $1/e$ part of its initial value (Figure 3). The d_p depends on the refractive-index contrast between the two media (n_g, n_c), the effective refractive index and the wavelength of the propagating light. Its value can be in the range of 30-150 nm, typically for visible light waves [4]. Nonetheless, by optimizing the opto-geometrical design of the waveguide, it can be extended. For this purpose, the waveguide symmetry, regarding the refractive indices, can be reversed. Such an approach was applied in a study [22], achieving a great increase in the extension of the evanescent field to about 1 μm.

The phenomenon of evanescent waves also implies that any changes in the local refractive index in this evanescent field alters the effective refractive index, as well. This also shifts the phase of the light propagating in the waveguide, which can be detected (Figure 3b) [4,17].

Due to this characteristic property of the optical waveguides, the evanescent field is of particular importance. It provides a way to probe the vicinity of such waveguides, which has been utilized in optical microscopy, e.g., as a powerful technique (total internal reflection fluorescence – TIRF) [23,24], and has paved the way for a widespread biosensing applications [4,25].
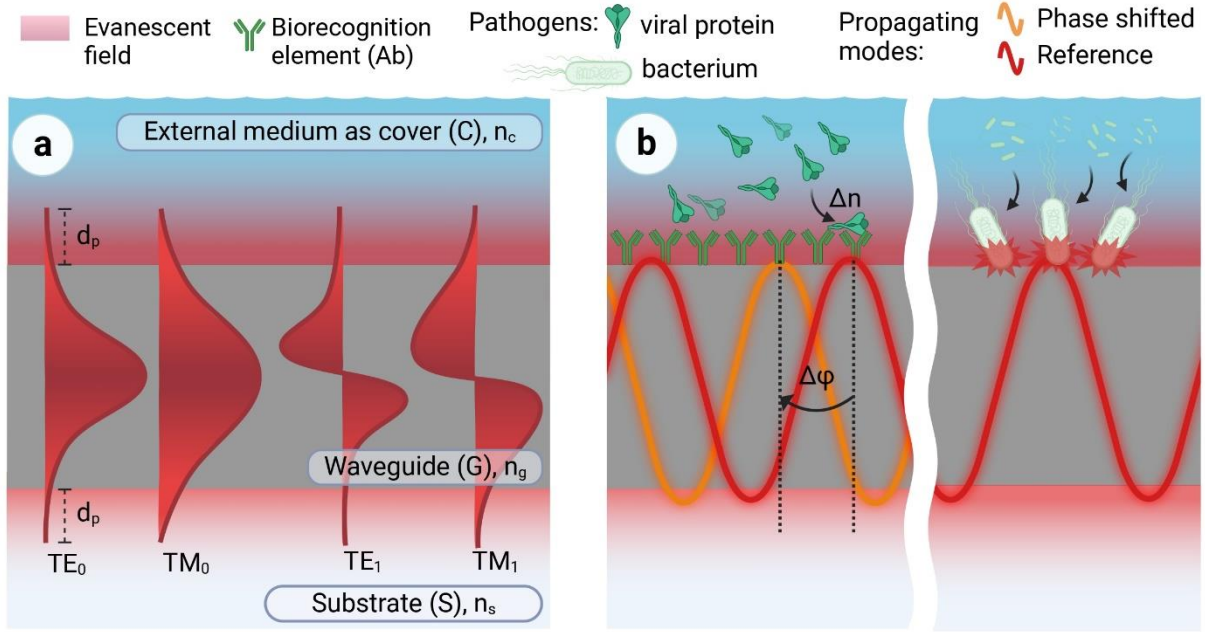
Figure 3. (a) Schematic illustration of propagation modes (0th and 1st) for different polarizations – transversal electric (TE) and magnetic (TM) – in a planar waveguide with their field-distribution. These propagating modes penetrates to the surrounding media at a limited extent – penetration depth (d_p) – , which is called the evanescent field. **(b)** Any change in the local refractive index (Δn) in this field, e.g., the adsorption of a viral protein on the antibody (Ab) covered waveguide surface, results a change in the phase ($\Delta \varphi$) of the propagating mode. Moreover, the evanescent waves of this mode can even scatter on cells. These phenomena can be used in various ways for biosensor applications. The figure was created with Biorender.com, adapted from a figure of a recent study [4].

1.2.3. Integrated optical components

As it was mentioned, integrated optics intends to implement systems analogous to electrical integrated circuits. Accordingly, many electronic components also have an integrated optical counterpart. These include passive ones as well as active ones that require energy for their operation. For example, in this case, waveguides correspond to the transmission of signals in an analogous manner to electric wires as passive elements. Optical signals can also be handled by IO lenses, gratings, light couplers, and distributed using Y branches or other beam splitters. The intensity and phase of the light guided by these structures can be modified by active elements. In this case, the local extinction or effective refractive index of the waveguide's environment is modified under the influence of an external stimulus, which can be electrical, magnetic, or thermal. In case of the latter, DC current can be applied on a heating wire, thus changing the local refractive index near the waveguide, causing phase modulation of the guided light [26–28].

By assembling the above elements, complex, active photonic integrated circuit devices, such as decoders/multiplexers, switches, and intensity modulators can be realized, which play a key

role in signal processing. In such systems, these active components were made up of non-linear optical (NLO) materials, such as chromoproteins.

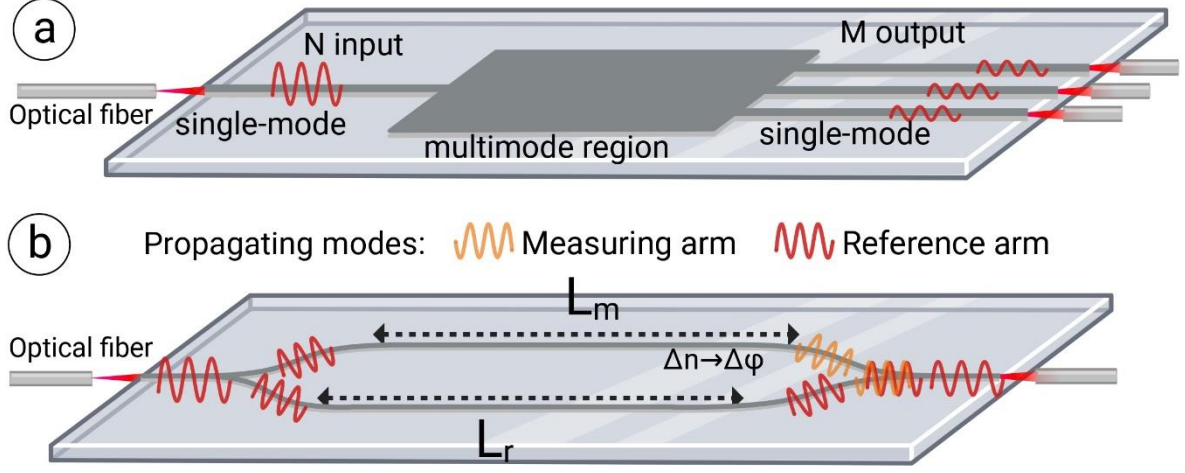In the following, two interferometric devices are detailed [17,29].

Figure 4. Schematic illustration of integrated optical multimode (MMI) **(a)** and Mach-Zehnder interferometer (MZI) **(b)** structures. For the MMIs, the light propagates in N (equals 1 on the figure) single-mode waveguide(s), then it reaches the multimode region. There an interference pattern is created, which determines the light intensities of the M (equals 3 on the figure) output single-mode structures. This can be used for light intensity distribution, multiplexing, and demultiplexing. In the Mach-Zehnder interferometer **(b)**, the light is coupled to a single-mode structure that splits into two arms, the reference and measuring ones with equal length (L_r, L_m), which then join. The interference of the light waves, propagating in these arms, determines the output intensity. Any change in the refractive index of the measuring arm (Δn) results a phase shift ($\Delta \varphi$) in the light, compared to that of the reference arm, which can be detected through the modulation of the output light intensity. The figure was created with Biorender.com.

Multimode interferometer (MMI)

If multiple equal distribution, for example the multiplexing or demultiplexing of the light power, had to be implemented, the use of nested Y branch structures would not be efficient. The reason for this is that there would be a significant loss in the branches due to their geometries with various branch angles. To reduce such power loss, multimode interferometer (MMI) beam splitters can be applied. With such structures, the light intensity from any N inputs can be distributed equally among M outputs (Figure 4). Its operation is based on the interference of the coherent and monochromatic waves entering the multi-mode device from single-mode inputs, which gives a standing-wave pattern, the so-called Talbot-pattern. Therefore, by designing the geometry, M nodes of outputs can be positioned at a given cross-section of the structure such a way that the output intensity can be maximized and the power can be balanced among them. Such MMIs can provide the basis of IO array-waveguide gratings (AWG), which

could be used in fiber-optic communication systems as wavelength division multiplexers [30,31].

Mach-Zehnder interferometer (MZI)

In photonic integrated circuits, light switches play a decisive role in terms of operating speed. Such switches can be created by modulating the light intensity. The integrated optical Mach-Zehnder interferometer is especially suitable for this purpose. The original concept of this device was developed by Mach and Zehnder for optical systems at the end of the 19th century. They showed that a change in the optical properties of a sample can be detected using the wave nature of light through the change in the refractive index between collimated beams of a light source. The current integrated optical design of this device is made up of waveguides. In these systems, monochromatic, collimated, polarized light propagates in a single-mode waveguide, whose structure splits into two arms of equal length, the measuring arm, and the reference arm. Then they join again. Interference, resulting from the superposition of the light beams propagating in the arms, occurs at the point of the joint. The light then exits the device through an output single-mode structure, which can be detected by a photodetector or CCD camera. If the optical path length of the two arms is the same and the environmental parameters are also common for them (temperature, humidity), the input and output light intensities are equal. The former occurs if they have equal refractive indices and lengths. In this case, maximum amplification is achieved between the interfering waves. However, if the refractive index changes in the vicinity of the measuring arm, a phase shift occurs in the light propagating in it, due to the interaction of the evanescent field. This means that the optical path length changes in that arm, and a phase difference arises for the light waves propagating in the two arms. Therefore, the output light intensity also changes due to the interference between the measuring and reference arms of intensities I_m and I_r, respectively. This intensity (I) is a periodic sinusoidal function of the phase shift ($\Delta\varphi$); therefore, it can be calculated as follows:

$$I = I_m + I_r + 2 \cdot \sqrt{I_m * I_r} \cdot \cos \Delta\varphi \qquad \text{(Eq.5.)}$$

Meanwhile, the phase shift, causing the intensity modulation, arises from the refractive index difference observed by the beams propagating along the lengths of the two arms (L_m, L_r). Its value can be determined by the following equation:

$$\Delta\varphi = k \cdot \left(\int_{L_m} n(\underline{r}) d\underline{r} - \int_{L_r} n(\underline{r}) d\underline{r} \right) \qquad \text{(Eq.6.)}$$

where k is the wave number (Eq.2.), n($\underline{r}$) is the refractive index of the medium at $\underline{r}$ point. Based on these calculations, such integrated optical Mach-Zehnder interferometer (IO MZI) devices

have been utilized for refractive index measurements for optical and biosensing purposes. Depending on the layout and the materials of the waveguide, refractive index unit (RIU) detection limit of ca. 10^{-7} can be achieved. Such sensitivity and design with the possibility of evanescent field detection support the application of such construction for biosensing purposes [4,21,29].

1.3. Label-free integrated optical biosensors

In integrated optical biosensors, a waveguide provides the main component for the label-free detection. The evanescent field-based sensing technique associated with optical waveguides is the main method among these sensors. In this case, the change in the refractive index of the waveguide's vicinity results in a variation in the phase of the light propagating in the structure. This can be exploited to detect biochemical reactions with bio-recognition elements placed on the surface of the waveguide, thus enabling rapid, sensitive, and specific detection of a given analyte. There are several techniques that use this detection principle in different ways. These include, for example, optical waveguide light-mode spectroscopy (OWLS) based on grating gating and resonance frequency shift detection. In addition, surface plasmon resonance (SPR) techniques are widely investigated, where plasmons are induced in a surface metal layer, and the evanescent field of the plasmon waves is used to detect microstructural changes in the surface vicinity. Although these are highly sensitive devices, their in/out-coupling design may limit their LOC integration and portability. In this respect, IO interferometric sensors have the advantage of offering more possibilities for light coupling, e.g., by coupling an optical fiber or lens to the end of the waveguide. The most common representative of these devices is the IO Mach-Zehnder interferometer, where the evanescent waves of the light, propagating in the measuring arm, interact with the liquid sample, so that the adhesion of a potential analyte on the surface can be detected via a change in intensity due to interference between the waves guided by the two arms.

Such biosensors have shown good performance in the detection of several pathogens. In addition to optical detection methods, an unconventional technique may be based on image processing of scattered light. Using this approach, a 30x surface-pre-enrichment of pathogen bacteria was achieved by applying an external electric field. Then these bacteria have been identified and detected with fluorescent labeled antibodies from fluid samples by first light scattering and then by fluorescence, recorded by a CCD camera [32]. Another, commercially available optical system uses such a scattered evanescent light-based method for detection of bacteria from fluid samples. Starting from the above-mentioned techniques, such biosensors,

where larger (a few µm size) surface-bound pathogens are desired to be detected by scattering evanescent waves on them, may be applicable [6,33].

Table1. Comprehensive review of evanescent-field sensing based label-free biosensor constructions, regarding the limit of detection (LOD), and the target pathogen microorganisms

Sensor type	LOD	Target pathogen	Sample	Refs.
OWLS	60 cells/mm^2	E. coli[1] K12	buffer	[34]
OWLS	$1.3 \cdot 10^4$ CFU/ml	Legionella pneumophila	water	[35]
SPR	10^3 CFU/ml	MRSA[2], E. coli O157:H7	buffer	[36]
MZI	10^6 CFU/ml	E. coli	buffer	[37]
MZI	10^5 CFU/ml	Listeria monocytogenes	buffer	[38]
Light scattering (MIT 1000)	10-50 CFU/assay	E. coli, Cryptosporidium, Giardia	cells from colony	[39]

As it was mentioned above, the IO technology enables miniaturization and portability of these IO-structure based devices, which can be then easily incorporated into LOC systems. This allows the creation of a complete sensor architecture, including microfluidic and signal readout units, so that even a non-expert can perform POC testing of body fluids [5].

The importance of applying such biosensors in healthcare has been shown in many situations in everyday life, especially during the recent pandemic period. Nowadays, nosocomial infection during hospitalization, food poisoning or disease spreading in rural places are urgent issues. Considering these topics biosensors as portable POC devices, performing the desired rapid, selective, and sensitive detection of target bacteria, such as the fecal coliform *Escherichia coli (E. coli)*, the spore *Salmonella,* and the food borne *Shigella* or other strains, can play an important role. These bacteria could cause serious infection even at low concentration in various body fluids (e.g., urine, saliva, or blood). For example, this means an infection dose of 10-100 colony forming unit (CFU), related to microbiological cell-culturing technique in case of two, diarrhea-causing bacteria strains *E. coli* (enteroinvasive, 0157:H17) and *Shigella* [40,41]. However, a larger number of cells is required for infecting a host for *Staphylococcus aureus*, which can be varying in the range of 10^3-10^8 cells [40]. Sticking further to medical diagnostics, beyond the health crises caused by bacteria, in this term the discussion of viruses is also relevant. In the last decade, 5 different pandemics have emerged worldwide, severe acute

---

[1] *Escherichia coli*
[2] *Methicillin resistant Staphylococcus aureus (MRSA)*

respiratory syndrome (SARS), swine flu, Middle East respiratory syndrome (MERS), Zika, and the coronavirus disease 2019 (COVID-19), according to the WHO. Consequently, biosensors have a key role to play in mitigating the spread of epidemics, in addition to the rapid and accurate 'on-site' detection of viral infections. This was also evident in the testing during the consecutive waves in the pandemic of COVID-19, caused by SARS-COV-2, where rapid diagnosis could be a lifesaver [5]. This disease still poses serious health risks. Thereby, several problems affecting various organs in long-covid syndromes, arising in the case of severe infections [42]. These may include neurological symptoms such as dizziness, brain fog, headache, fever, anxiety/depression, and vascular problems of similar severity such as cerebrovascular-endothelial injury, hypoxia/ischemia [42]. In this regard, biological barrier systems composed of epithelial and endothelial cells play a key role in the spread of the virus throughout the body after it enters the oral cavity or nasal cavity during infection [43,44]. Such systems are present in the lungs, capillaries, nasal cavities, and intestines, which are exposed to infection. Through these, the virus, or its components, could reach the blood-brain barrier (BBB) via the bloodstream [44]. For example, the surface spike protein of the virus, or its subunit (S1), that is important in cell-surface receptor-recognition process, can detach from the virion by enzymes or heat shock, and spread throughout the body [45,46]. It can thus trigger pathological processes on its own. The presence of S1 has been identified in rodent brain tissue where it was administered intranasally, thus the protein could cross the BBB [47]. The use of biosensors in the study of pathologies associated with this type of disease could also play a key role in gaining a thorough understanding of the infection [5,48–50].

1.4. Dielectrophoresis

For accurate impedimetric detection of the amount of analytes in a fluid sample flowing in microfluidic systems, a higher proportion of the analytes must be deposited on the surface of the electrodes, in the detection field. For this purpose, impedimetric biosensors often apply the phenomenon of dielectrophoresis (DEP), where dielectric particles (e.g., cells, polystyrene beads), suspended in the medium, can be polarized, and manipulated by a spatially non-uniform electric field, typically alternating (AC) electric field. In such biosensor systems, this field is applied to the measuring surface electrodes. During dielectrophoresis, a dipole is induced in the cells depending on the frequency of the AC field, which causes their motion in the sample according to the physical parameters of the medium and the cells. This movement is determined by the permittivity (ε), conductivity (σ), and dielectric parameters of the particles and the

medium [51]. Based on these properties, the arising dielectrophoretic force (F$_{DEP}$), acting on spherical particles, can be given as follows [52]:

$$F_{DEP} = 2 \cdot \pi \cdot r^3 \cdot \varepsilon_m \cdot Re\left[\frac{\varepsilon_p^* - \varepsilon_m^*}{\varepsilon_p^* + 2 \cdot \varepsilon_m^*}\right] \cdot \nabla E_{rms}^2 \qquad (Eq.7.)$$

where r is the radius of the sphere, ε_p^*, ε_m^* are the complex permittivity of the particle and the medium, respectively, in the real part of the Clausius-Mossotti (CM) factor, describing the relative polarizability of the particle as $\frac{\varepsilon_p^* - \varepsilon_m^*}{\varepsilon_p^* + 2 \cdot \varepsilon_m^*}$, and ∇E_{rms}^2 is the gradient of the root-mean-square of the applied electric field [53]. Each complex permittivity shows the influence of the radial frequency (ω) of the AC field on this effect, as it is given by:

$$\varepsilon^* = \varepsilon + \frac{\sigma}{j \cdot \omega} \qquad (Eq.8.)$$

where ε represents the permittivity, σ the conductivity, ω the radial frequency of the AC field, and j equals to $\sqrt{-1}$. According to the equation (Eq.7.), based on the CM factor (+ / -), the force can be directed towards the maximum value of the electric field strength, collecting the cells on the surface of the electrodes. This is called positive dielectrophoresis (pDEP). In the opposite case, a force pointing towards the minimum of the field strength repels the cells from the electrodes, which is called negative dielectrophoresis (nDEP). A transition between the two cases also occurs because of the frequency dependency of the F$_{DEP}$. This can be characterized by the cross-over frequency for a given condition particle in the fluid medium, where the CM factor, therefore F$_{DEP}$, is zero [33,54].

Due to the above-mentioned properties and the wide range of possibilities, DEP can be used in a variety of ways in such microfluidic systems. For example, cells can be sorted [55], separated, or collected and/or concentrated [56]. In this way, pathogen bacterial cells, mentioned above, can be collected on electrodes. The use of DEP-based bacterial concentration with biosensors can provide an efficient performance enhancement by reducing the number of lost pathogens to be detected at low flow rates [54,57,58].

Objectives

The scientific work was primarily aimed at the design, fabrication, and application of integrated optical structures. In this context, the focus was particularly on current topics in medical diagnostics, namely for practical point-of-care (POC) use as rapid clinical tests.

In the first proof-of-concept project, the goal was to create an optical biosensor device based on an integrated optical polymer waveguide structure, and evanescent field sensing for label-free, rapid, selective, and sensitive detection of *Escherichia coli* bacteria in body fluids. To this end, the evanescent waves of red light, scattered on the target cells, provide a scattering pattern that can be used for biosensing. The sensitivity of such a device can be increased by using dielectrophoresis, which exploits the polarizability of the cells by collecting them on the surface of electrodes placed near the waveguide, using an alternating electric field. This way an electro-optical biosensor can be realized, consisting of surface electrodes and microfluidic channels placed in the vicinity of a polymer waveguide stripe on a glass substrate. Itwas intended to be used to detect the concentration of bacteria in the suspension, previously collected on the waveguide surface, by analyzing the scattering pattern of evanescent waves, using a microscope objective of different magnifications, a CCD camera and image analysis.

In a second application, the aim was to develop a miniature Mach-Zehnder interferometer-based biosensor, to detect proteins. It can be achieved by using its interferometric measurement principle, providing the speed, accuracy and specificity required for the detection of such biological particles. To reach optimal, stable detection with the device, the bias-point adjustment of the sinusoidal transfer function of the interferometer can be used. To this end, I wanted to thermo-optically modulate the refractive index of the medium in the proximity of the waveguide. This can be achieved by applying a direct current (DC) to a gold microheater structure placed near the reference arm of the interferometer. The device was intended to be used in a current topic, namely, to study the neuroinvasion of SARS-CoV-2 coronavirus particles. The medically relevant aspect of this is in connection with the ability of the surface spike protein (S1 subunit) of this virus to cross biological barriers of the human body. We wanted to investigate this phenomenon, in collaboration (cell culturing, permeability assay, ELISA) with the members of Biological Barriers Research Group of our institute, in case of blood-brain barrier and intestinal barrier models, since both systems are highly exposed to the infection. For this purpose, permeability assays were planned to be performed. Then, from the fluids, derived from these assays, the S1 subunit could be detected specifically by two techniques, with the biosensor and a traditional laboratory assay (ELISA).

2. Materials and Methods

The integrated optical waveguide-based biosensing applications discussed in this thesis perform evanescent-field detection. While they are distinct sensor constructions, and differ in the application, quantification and readout techniques, the methods required to fabricate them are almost the same. Indeed, both constructions were designed for rapid, selective, and sensitive detection of analytes of fluid samples. The electro-optical biosensor, however, integrates a dielectrophoretic technique to increase the sensitivity for size-selective and unspecific detection of bacteria, while the IO MZI is designed for specific target-protein sensing. In the following, first the fabrication of these two devices, the tools and methods used to perform tests for the measurement of medical diagnostically relevant analytes will be described. Then, regarding the liquid samples to be detected, the preparation of *E. coli* bacterial samples used in electro-optical biosensor measurements will be described.

As one of the focuses of the current dissertation is on the adaptation of the interferometric optical biosensing approach to determine the passage of the spike protein subunit S1 through the barrier systems. The related processes are described as parts of the workflow of the corresponding study (Figure A1) [49]. In this context, the barrier system models that play a key role in this scientific work, the assay that models the passage of the spike protein across them, and the alternative traditional detection ELISA technique that quantitatively characterizes it are also detailed, to give a comprehensive overview of this project. Notably, the related research activities (described in the 2.4. and 2.5. sections), and the evaluation of the corresponding tests (see Annex) were carried out by our colleagues of the Biological Barriers Research Group.

2.1. Device designs and fabrication

Both biosensor constructions were built from the same components. On a microscope coverslip substrate, gold surface microstructures and polymer waveguides were integrated with a silicon microfluidic channel. Their fabrication procedure was based on a previous process used in a study of our research group, where an IO MZI integrated optical biosensor was realized for *E. coli* bacteria detection in suspension [37]. However, this protocol has been improved, and its applied techniques have been expanded. It is important to note that differences in the construction of each recent device can be found due to their application specificity. As a pre-fabrication step in the procedure, the layout of the structures and the channels were designed with CAD/CAM software (Layout Editor, juspertor GmbH, Unterhaching, Germany) originally used for printed circuit board design. Such patterns of the microstructures (electrodes,

waveguides, masks) were realized by UV lithography, namely by maskless, direct laser writing (DLW) technique utilizing a micro pattern generator (μPG-101 machine, λ = 375 nm, Heidelberg Instruments GmbH., Heidelberg, Germany). For this purpose, epoxy-based, UV-sensitive polymer layers, the so-called 'photoresists' or 'photopolymers' were used. Two types of them are known, according to the names used in photographic processes, positive photoresists when cross-links are disrupted in the layer by illumination, and negative ones when cross-links are formed. Accordingly, the structuring of these materials followed the manufacturers protocols.

2.1.1. Gold microstructures

In the case of the two biosensors, the electro-optical and the IO MZI, gold microstructures were fabricated on the surface of the glass substrate to perform different tasks.

For the former, it meant dielectrophoretic cell collection on the waveguide surface. Thereby, these cells could create elementary scattering points through their interaction with the evanescent waves of light propagating in the waveguide. To realize this, pairs of tilted surface gold electrodes were designed to provide a non-uniform, inhomogeneous electric field. Thus, a waveguide could be made in the gap between the tips of the electrodes where the electric field maxima were located. The layout of this electrode system was inspired by a design previously used to focus bacteria in a microfluidic channel [59].

For the other, IO MZI, the thermo-optical bias point setup required the creation of a surface gold heating wire structure. By applying a direct current to it, a change in refractive index of the reference arm and its surroundings could be achieved. The structure was positioned so as to provide a stable function, while leaving enough room for dissipation, avoiding heating of the measuring arm or the liquid sample. The first application of this biasing technique was tested for an IO MZI biosensor, where all-optical switching based on photoexcitation of a protein of nonlinear optical properties was demonstrated using a waveguide-based interferometer [60].

The preparation of the above-mentioned different gold microstructures on glass substrates represented the first major step in the construction of both biosensors (Figure A2 for heater in Annex). In this process, the electrode or heater structure was formed by lift-off lithography. In the first part of this, the pattern was created in a sacrificial layer, as a mask. First, a 2 μm thick positive photoresist, S1818 (micro resist technology GmbH., Berlin, Germany) layer was spincoated (3000 RPM, 60 s) on a cleaned 24x50x0.17 mm (width x length x thickness) coverslip (Menzel-Gläser, Thermo Fisher Scientific, Waltham, Massachusetts, USA). This was followed by soft-baking (115 °C, 1 min). The layer was then exposed by the above-mentioned

DLW machine to form the pattern of the desired electrode or heating wire structures. The sample was then immersed in the developer solution (MICROPOSIT MF-319 solution, Kayaku Advanced Materials, Inc., Westborough, Massachusetts, USA) corresponding to the photoresist, followed by washing with deionized (18.2 MΩ) MilliQ water (Synergy® UV Water Purification System, Merck-Millipore, Burlington, Massachusetts, USA) to remove the exposed parts. Thus, the mask for the gold microstructures was prepared. The next steps in lift-off lithography were to deposit gold onto the sample by sputtering, directly onto the glass according to the pattern in the mask layer. In that process, first the mask was repeatedly exposed to UV light of the i-line of a mercury lamp (Oriel 97,435 UV lamp, λ ≈ 365 nm, Newport Corp., Irvine, California, USA) so that the sacrificial polymer layer could be removed by subsequent development. It was followed by sputtering, where an adhesion promoter thin (10 nm) Cr layer was also deposited prior to the homogeneous gold layer. The thickness of this gold layer was 30 nm for the electrode system and 20 nm for the heater wire structure. During the sputtering under high vacuum ($8*10^{-2}$ mbar), sputtering ions were generated using Ar gas to provide the deposition.

Once coated, the mask was removed from the sample by subsequent immersion in the developer solution for a longer period (2 days) as described above. Finally, after washing again in deionized water (MilliQ) and drying, the coverslip contained gold structures corresponding to the desired pattern. Thus, a 2 mm long system of 10 µm wide electrode pairs with 15 µm adjacent spacing and 10 µm gap was prepared for the electro-optical biosensor. For the MZI, biasing 10 µm wide heating wire of about 350 µm length with wider outlet sections was realized (1kΩ resistance) [60]. The resulting sample, including gold microstructures on the coverslip, served as a substrate in the subsequent steps of the device fabrication.

2.1.2. Polymer waveguides

To achieve integrated optical waveguiding, the waveguiding strip structures, for both biosensors, were made of low-optical-loss negative photoresists with nearly identical refractive indices (n = 1.591 & n = 1.584 @ 670 nm). These two materials were EpoCore for electro-optical biosensor, and SU-8 for the IO MZI structure (EpoCore_2 & SU-8 2002, micro resist technology GmbH., Berlin, Germany), optically transparent at both visible and telecommunication near-infrared wavelengths (e.g., 1330 nm and 1550 nm) [61–64]. Their fabrication differs only in the baking steps. In the case of the two biosensors, the waveguides made of each material were formed in a layer of 2 µm thickness. The width of the strip in the case of the electro-optical biosensor was 8 µm, matching the electrode-pair gap, thus forming

an MMI structure. That of the IO-MZI was 2 µm, achieving single-mode waveguiding for the interference-based detection, where the length of both arms was 1 cm.

The fabrication process of the waveguide is very similar to that of the sacrificial layer of the mask used for gold microstructures (Figure A2 in Annex). Due to the narrower structure of single-mode waveguides, in such cases first a thin (sub-µm), negative photoresist adhesion promoter (Surpass 3000, micro resist technology GmbH, Berlin, Germany) was coated on the glass substrate, covering with the gold microstructure, by dip coating, following the protocol of the manufacturer. Afterwards, the microscope coverslip was spincoated (3000 RPM, 60s) with the current negative photoresist and then baked. This soft-baking was done in one step (95 °C 1 min) for SU-8, while for EpoCore it consisted of several steps, initially at 50 °C for 2 mins followed by uniform heating and finally at 90 °C for 2 mins. Once the sample had cooled to room temperature, it was exposed to the pattern according to the designed layout of the different waveguides using the DLW technique with UV light. This was followed by post exposure bake, also consisting of several steps for Epocore, initially at 50 °C 2 mins then uniform heating and finally 85 °C 3 mins, while for SU-8 this was done in one step (95 °C 2 mins). As soon as the coverslips had cooled down to room temperature, they were immersed in a developing solution (90 s), which was the same solution for both photoresists (mr-Dev 600, micro resist technology GmbH., Berlin, Germany). Thus, after washing with isopropanol and drying, the components essential for detection of the biosensors were prepared.

2.1.3. Microfluidic channel

To detect target analytes from a low-volume fluid sample, it is necessary to integrate the device with a microfluidic channel. Thereby, an adequate, continuous flow of the liquid sample can be achieved, which ensures, for example, in the case of the electro-optical biosensor, the dielectrophoretic cell-collection, while in the case of the IO MZI, the specific protein detection. The process of such channel preparation (Figure5 in Annex) followed a protocol established by our research team, described in a previous study[37]. The design of the channel system was originally adapted for MZI, but can be equally applied to these recent biosensing applications. In the case of such a design, there are two parallel channels separated by 1 cm, made up of a silicone material, polydimethylsiloxane (PDMS). Each has a 1 cm long, 250 µm wide section that can be applied, while the channel height is 30 µm. Such a channel can be prepared using a soft lithography technique. The first step in the process was the preparation of a mold from SU-8 negative photoresist capable of creating a structure of the appropriate thickness (SU-8 2015). As a first step, a layer of photoresist of the desired thickness (30 µm) was spincoated (1200

RPM, 60 s) on a microscope coverslip. This was followed by a soft-bake step (95°C, 300 s). The resist layer was then exposed to UV light through a photomask (Oriel 97,435 UV lamp, λ ≈ 365nm, Newport, Corp., Irvine, California, USA). Exposure was followed by post-exposure bake (95 °C, 5 mins), then development in a solution (5 mins). To finish the preparation of the master mold, it was washed with isopropanol and then dried. A degassed liquid PDMS prepolymer in a mixture of 1:10 (Sylgard 184, Dow Corning, Midland, Michigan, USA) was then poured onto this surface and cured for 30 mins at 80°C. Thus, it formed a silicone stamp. Then, by peeling off this silicone and cutting holes (with 1 mm diameter) for the channel inlets and outlets, it became suitable for integration into the device. Therefore, both its surface and the surface of the microscope coverslip containing the biosensor components was activated with oxygen plasma with parameters (29.6 W, 400 mTorr, 60 s) (PDC-002, Harrick Plasma). As a result, the two units could be bonded together covalently to create the corresponding biosensor device, considering the correct positioning of the channels. To flow the applied fluids in channels, the sample in a syringe is injected by a pump (SP210IWZ syringe pump, World Precision Instruments Inc., Sarasota, FL, USA) through silicone tubes to the inlets via pipette tips attached to them, and the used, waste fluid is removed from the outlets in an analogous way [37].

2.2. Waveguide surface biofunctionalization

The specific recognition of the S1 subunit of the spike protein by the IO MZI biosensor was achieved by the immunological antigen-antibody interaction on the waveguide surface of the measuring arm, coated with protein-specific antibodies (Figure5 in Annex). During this process, fluid samples of 1 ml volume were used. First, the channels were cleaned by flowing ethanol through them. Next, they were filled with antibody activating reagent, stock solution (Mix&Go™ (AnteoBind™) Biosensor, AnteoTech Ltd., Brisbane, Australia) diluted 1:20 with MilliQ deionized water and incubated (room temperature, 30 mins). The system was then washed with standard phosphate-buffer saline (PBS) solution (1x, pH = 7.4). The waveguide surfaces of the MZI were functionalized with the antibody solution (MonoRab™ SARS-CoV-2 Neutralizing Antibody (BS-R2B2), monoclonal antibodies, Rabbit, GenScript, Piscataway, NJ, USA, diluted with 1×PBS at a final concentration of 5 μg/ml) and incubated overnight (4 °C). Prior to measurements, both the washing of unbound antibodies and the local refractive index matching of both MZI arms vicinity were performed by flowing the buffer solution (0.1% bovine serum albumin (BSA)–Ringer–HEPES (RH) buffer (150 mM of NaCl, 5.2 mM of KCl,

2.2 mM of CaCl2·2H2O, 0.2 mM of MgCl2·6H2O, 6 mM of NaHCO3, 2.8 mM of D-glucose, 5 mM of HEPES, pH = 7.4)) in the microfluidic channel system.

2.3. Preparation of fluid samples containing *Escherichia coli* bacteria

The detection concept, optimization and performance of the electro-optical biosensor were tested with cultured suspensions containing different concentrations of live *E. coli* bacterial cells (non-virulent Dh5α strain). Initially, a single culture of cells were pipetted from initial bacterial cultures, grown, and stored (4 °C) on agar plates, into growth media (lysogeny broth, LB) of 3 ml in sterile polystyrene tubes then left overnight in a shaker incubator (30 °C). The next day, the cell cultures were backdiluted (100x, 3 ml of LB medium) and incubated again until reaching the growth phase of their reproduction curve (OD_{600}=0.4). This was followed by the preparation of bacterial suspensions. The low conductivity of the sample, relevant for dielectrophoretic (pDEP) cell collection, was achieved by diluting the cell culture with a master dilution solution (1:9) in an Eppendorf tube (1.5 ml). The master dilution solution was prepared considering the maintenance of cell viability during the measurements. The concentration of bacteria in the undiluted bacterial culture fluid sample was determined (CFU/ml values) by plate counting technique. Prior to measurements, a serial dilution was made with the master dilution solution in the desired cell concentration range.

An artificial urine sample containing a mixture of living somatic and bacterial cells was also used to test the selectivity of the DEP-based cell collection technique and the practical application of the electro-optical biosensor. The suspension preparation procedure was the same as mentioned above. Here, negative artificial urine (pH = 5.94) was used instead of LB in the master dilution solution with the same ratio (1:9). The preparation of the artificial urine was carried out by modifying the base solution of the protocol of 'CaseA', described in a study [65] (2:1 mixture of 1.3609 g KH_2PO_4 (0.1 M) dissolved in 100 ml MilliQ water and 2.2823 g K_2HPO_4 (0.1 M) dissolved in 100 ml MilliQ water). For the preparation of the cell mixture, endothelial cells (hCMEC/D3, Human Cerebral Microvascular Endothelial Cell Line), grown in an incubator and backdiluted, were added to the *E. coli* cell culture. Prevention of endothelial cell aggregation in the measurement cell mixture was achieved by the addition of Tween-20 (7.5 mg to 150 ml solution).

2.4. *In vitro* human biological barrier cell culture models

As it was mentioned, the integrated optical interferometric biosensor was developed to ascertain the ability of the S1 subunit of the SARS-COV-2 spike protein to cross two human

tissue barriers exposed to infection. Human models of these biological systems included *in vitro* BBB co-cultures (human endothelial cells and pericytes) and intestinal epithelial cell (Caco-2) cultures.

2.4.1. Blood-brain barrier

In accordance with previous studies [66,67]), cell culture of the BBB model consisted of two cell types, human umbilical cord stem cell-derived endothelial cells (hECs) and bovine brain pericytes (PCs). Both cell types were cultured in a corresponding supplemented medium in 0.2% gelatin (Sigma, part of the Merck Group, Darmstadt, Germany)-coated dishes (Corning Costar; Corning, NY, USA). Therefore, the hECs endothelial culture medium (ScienCell, Carlsbad, CA, USA) also contained 5% fetal bovine serum (FBS; Sigma), 1% endothelial cell growth supplement (ECGS, ScienCell) and gentamycin (Sigma, 50 μg/ml). While the PC cell culturing was performed in Dulbecco's modified Eagle's medium (DMEM, Life Technologies, Thermo Fisher Scientific, Waltham, MA, USA) with 20% FBS (Sigma), 1% Glutamax (Life Technologies Co., Carlsbad, CA, USA) and gentamicin (50 μg/mL). Trypsinization followed to round up both cells once they reached confluency. As soon as this occurred the trypsin was removed, and the cells were collected in hEC culture medium and counted. BBB co-culturing and assemble was performed in cell culture inserts (Millicell Millipore, MCSP24H48, PET, 3 μm pore size, 24-well format). In these, both sides of the porous membrane were treated. The upper compartment, the apical side, was coated with a 1:48 ratio of growth factor-reduced Matrigel (Corning) in DMEM (1 h, room temperature), while the lower compartment, the basolateral side, with 0.2% gelatin (20 min, 37 ∘C). The inserts were then dried and inoculated with cells. This was initially performed by PCs (5×10^3 cells/insert) to the bottom of the inserts. The inserts were turned into a 24-well plate (Greiner, Kremsmünster, Austria) after adhesion of these cells. hECs (1.3×10^4 cells/insert) were then seeded into the upper compartment. Finally, they were fed every two days during co-culturing (4 days).

hECs were derived from the blood sample, which procedure was approved by the French Ministry of Higher Education and Research (CODECOH Number DC2011-1321). The study was performed according to the World Medical Association Declaration of Helsinki with the informed parental consent of the infants (Béthune Maternity Hospital, Béthune, France). The sample containing hECs was received via passage 5 and the dishes were subsequently used with passage number 7.

2.4.2. Intestinal barrier

The other biological barrier prone to be affected by the coronavirus infection is formed by epithelial cells in the host's intestinal tract. The *in vitro* model of this was realized by using cells from human CaCo-2 epithelial cell line (ATCC cat. No. HTB-37; Manassas, VA, USA). Here, the cell culture medium of DMEM and stable glutamine (Life Technologies) was supplemented with 10% FBS (PANBiotech GmbH, Aidenbach, Germany) and gentamycin (50 µg/ml). CaCo-2 cells (3×10^4 Caco-2 cells/insert) were seeded into model cell culture inserts of the same type as above (2.4.1. section), where each culture surface was pre-coated with 0.05 % collagen I in sterile distilled water. These cells were left to grow in the inserts for an extended period of 12 days, with feeding at two days intervals.

2.4.3. Barrier integrity measurements

In *in vitro* cell culture models, the process of barrier formation was monitored prior to medium exchange. The trans-endothelial/epithelial electrical resistance (TEER) parameter is suitable for this purpose, which was measured in these cell culture models every two days during this period using an EVOM Volt/Ohm Meter with a 24-well plate chamber setup (ENDOHM-6G; World Precision Instruments, Sarasota, FL, USA). To eliminate fluctuations due to temperature changes, the cell plates were placed on a heating pad at 37°C. The TEER values ($\Omega \times cm^2$) were calculated using a method described previously [68]. This involved subtracting the background, the values of the cell-free inserts ($60 \ \Omega \times cm^2$), proportional to the surface area of the cell cultures ($0.33 \ cm^2$), and then correcting the resulting values for the shunt resistance of the inserts.

2.5. Verification and determination of spike protein S1 subunit capability of barrier model penetration

2.5.1. Permeability assays

The passage of the SARS-COV-2 spike protein S1 subunits across both barrier cell cultures (described in sections 2.4.1 and 2.4.2) follows the path of the proteins in the buffer solution (0.1% BSA-RH, detailed in section 2.2) from the top to the bottom compartments of the cell culture inserts. All the used surfaces were preincubated with BSA with this buffer prior to the measurements to prevent spike protein adhesion, including used low-bind pipette tips, internal plastic surfaces of the inserts, microcentrifuge tubes and plate wells. Assays could be started with cells from the two cell cultures once their TEER values reached the desired value, which was $34.6 \pm 1.9 \ \Omega \times cm^2$ for BBB and $367.76 \pm 36.8 \ \Omega \times cm^2$ for the intestinal one. At the

beginning of the permeability assays, spike protein subunit S1 proteins in buffer (200 µg/ml, 70 µl) were inserted in the top compartment of these inserts, while the bottom compartment was filled with low-bind pipette buffer (530 µl). To ensure the minimization of unstirred water layer on the cell layers during the process (30 mins), the assays were performed on horizontal shakers (150 RPM, Biosan, Riga, Latvia). Finally, TEER values were determined on the inserts after the assays, which were used for the proper interpretation of the results obtained by the optical biosensing and ELISA approaches. Control permeability assays were also performed. In the case of negative control, buffer, lacking the target spike S1 protein, was added to the cell culture system in the inserts. In positive control assays, the spike protein sample of the buffer, at initial protein concentration, was passed through cell culture-free inserts from the upper to the lower compartment and subsequently detected. To confirm the barrier integrity, buffer containing fluorescent markers was added to the cells in the negative control setup.

2.5.2. ELISA

The main method for the determination of the spike protein S1 subunit passage through BBB and intestinal barrier was the interferometric optical biosensing approach (section 2.6.2). However, a traditional indirect ELISA was also performed at room temperature for this purpose, following the process, described in a previous publication [69]. First, pretreatment of Nunc MaxiSorp flat-bottom plates (Life Technologies) was required, which was carried out with 10% AnteoBind Biosensor solution (AnteoTech) for 30 min. Next, the solution was washed with a wash buffer (tris-buffered saline (TBS) buffer and BSA, 10 mM TRIS-HCl, 150 mM NaCl and 0.5% BSA at pH = 7.4), used as a standard solution in the process between incubation steps. A dilution series from the SARS-CoV-2 spike protein stock solution, as well as samples from spike protein treated and control inserts from the lower compartment of the wells in triplicates (50 µl/well) were also added to the plates. This was followed by incubation of the latter samples at 4°C overnight, unlike the default room temperature. Dilution was performed in carbonate buffer (45.3 mM of $NaHCO_3$ and 18.2 mM of Na_2CO_3 in distilled water, pH = 9.6) at a protein concentration of 0-20 µg/ml. The next day, the blocking of the wells was achieved with 1% BSA-5% normal goat serum in TBS buffer for 2 hours. This was followed by the binding of the target protein to the primary antibody (MonoRab SARS-CoV-2 Neutralizing Antibody (BS-R2B2), 1 µg/ml, Genscript, A02051) after incubation (2h), and then secondary, biotin conjugated goat anti-rabbit antibody (0.3 µg/ml, Vector Laboratories Ltd., Burlingame, CA, USA, antibody ID: AB_2313606) was bound to this complex after 1 hour of incubation. The binding and hence protein detection was performed with extravidin peroxidase (0.5 µg/ml,

Vector Laboratories Ltd.). During this process, each well was loaded with this reagent for 30 min. Then, a substrate solution was added to the volume of each well (100 µl/well). For the preparation of this solution, ELISA substrate tablets containing o-phenylenediamine dihydrochloride (Life Technologies) were dissolved in 10 ml citrate buffer (63 mM Na_2HPO_4-$2H_2O$, 26.6 mM citric acid in distilled water, pH = 6) to which 3% H_2O_2 solution (25 µl) was added. After the addition of the substrate solution, a yellow color was formed within 10 min in the reaction, which was then stopped by adding 4 M H_2SO_4 (50 µl/well). A multi-well plate reader (Fluostar Optima, BMG Labtech, Ortenberg, Germany) was then used to detect this color change based on light absorbance at 492 nm. After the processing of the results obtained, the concentration of the spike protein subunit S1 was determined from the calibration curve of the dilution series.

2.6. Optical biosensing experimental setups

For the measurements with the integrated optical biosensor systems, the particular sensor was placed on a motorized stage with a micropositioner (DC-3K, Märzhäuser Wetzlar GmbH & Co. KG, Germany) of an inverted microscope (Zeiss Axiovert 200, Jena, Germany). A CCD camera was connected to this system and to a personal computer to monitor the ongoing processes. The continuous flow of the samples was provided by the microfluidic apparatus, the same way as it was done for the functionalization step of the IO MZI biosensor (for more details see section 2.1.3.). In case of both sensors, electric wires were connected to outlet contact pads of the surface gold microstructures (microheater or electrode system) by droplets of conducting epoxy (CW2400 CircuitWorks® Conductive Epoxy, Chemtronics, Kennesaw, GA, USA), through which the external electric field could be applied. Regarding the optical connections of the waveguides for both biosensors, red light of a laser diode, at a corresponding wavelength, was transmitted between elements of the optical system by single-mode optical fibers (S630-HP, Thorlabs). In this context, the light-coupling was performed based on end-coupling technique. This process was carried out using the instrumentation and procedure detailed in a previous publication of our research group [37].

As a first step in the light-coupling process, proper facets of the waveguides input and output were realized by cleaving the microscope coverslip sensor substrate, with the waveguide on it, with a diamond cutter (S90W, Thorlabs Inc.) at the proper positions. Next, the substrate was attached to a microscope slide by an optical adhesive (NOA-81, Norland Products Inc., USA) and then glued by exposing this adhesive by the UV light of a mercury arc lamp (100W, HBO 100 Zeiss, Jena, Germany). The light-coupling was performed by coupling the measuring red

light to one end of the above-mentioned optical fiber, and then positioning its other end to the corresponding facet of the waveguide (inlet or outlet). For this purpose, the micropositioner of the microscope setup was used. When the optimal position was reached, it was fixed with a photopolymer adhesive (OP-66-LS, Dymax Europe GmbH, Germany). Consequently, the ready-to-use version of the corresponding biosensor device was realized [33,37,70].

Due to the difference in the measurement concepts of the two biosensors, different instrumentation was used in their experimental setups (Figure 6), in connection with the detection and the application of the surface gold microstructures.
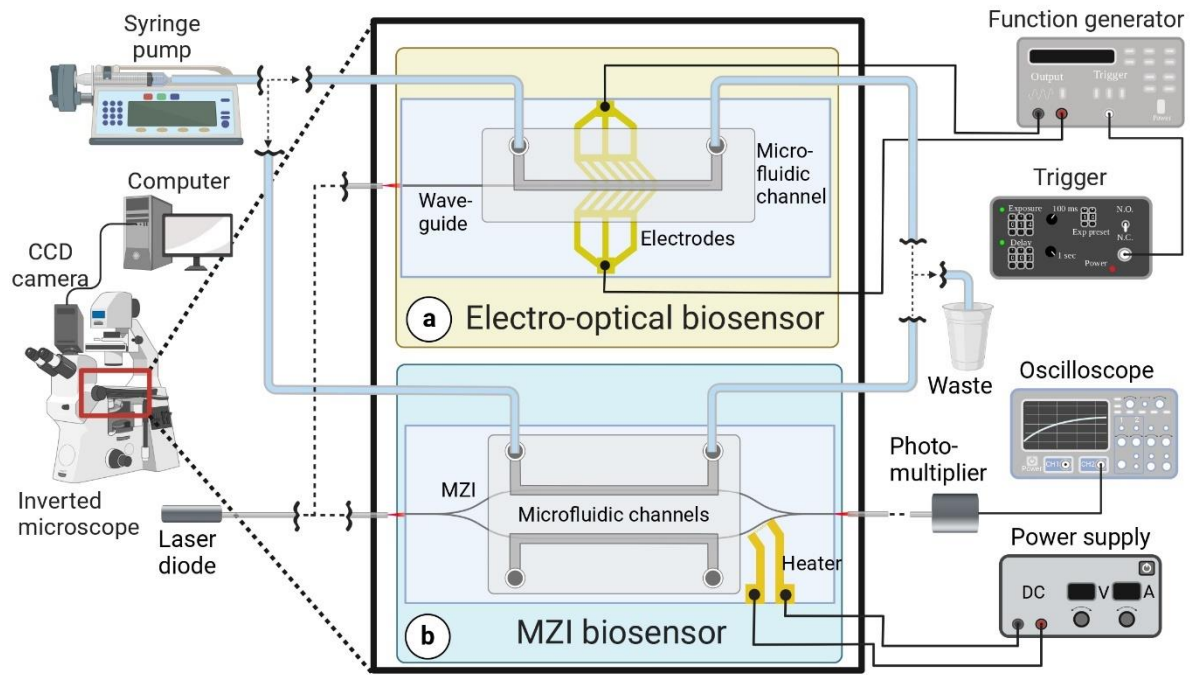
Figure 6. Experimental setups of the developed biosensors, the electro-optical **(a)** and the integrated optical Mach-Zehnder interferometer (MZI) **(b)** devices. During the measurements the corresponding device was placed on a motorized stage of an inverted microscope, where it was monitored with a CCD camera. The fluid sample was pumped through the PDMS microfluidic channel-system of the corresponding biosensor, where silicone tubes were used. The measuring red light of a laserdiode was transmitted between the light source, the waveguide structure of the corresponding biosensor, and the photodetector with single-mode optical fibers. In case of the electro-optical biosensor **(a)** the signal of a function generator, triggered by a shutter driver, provided the alternating electric field for the electrodes. For the MZI biosensor **(b)**, to perform the thermo-optical biasing, direct current of a power supply was added to the microheater structure.
The figure was created with Biorender.com.

2.6.1. Integrated electro-optical biosensor

In case of the detection concept of the electro-optical sensor, the CCD camera was also employed to acquire the scattered-light intensity images, which were the basis for the detection of the target bacteria. In this case, the red light of a laser diode (670 nm) was used. In this application the DEP-based cell collection played a crucial role. It was achieved by applying sinusoidal alternating (AC) electric field of different frequencies to the electrodes, utilizing the

signal of a function generator (20 MHz model 8020, Tabor Electronics). For triggering a square wave signal (1.4 s 'ON' and 3.0 s 'OFF') from a timer (Uniblitz VS14S2ZM1R1-21, Vincent Associates) was used.[33].

2.6.2. IO MZI biosensor

During the interferometric detection, the light at the output of the interferometer was transmitted to a photomultiplier (H5783-01, Hamamatsu). Its signal was then delivered to and recorded by an oscilloscope (LeCroy 9310-L, LeCroy). For measuring light, visible red light of a laser diode (658 nm, 100 mW, RLT650-100MGS, Roithner Lasertechnik GmbH, Vienna, Austria) was used. To perform optimal, stable measurements with the interferometer, its bias point was needed to be adjusted, which could drift easily due to, e.g., differences in the structures of the waveguides, or in the light-coupling. For this purpose, thermo-optical biasing can be applied, which technique has been widely studied and utilized for IO MZI structures [26,27]. The first step in the process was to adjust the thermoelectric effect of the microheater prior to the measurements. At this point, the phase change and the resulting modified signal level were set for a given DC voltage. To achieve this effect, namely, to adjust the sensor response signal to the inflection point on the transmission function, the voltage of the heating wire was varied between 0–4.6 V. The DC electric field on the surface gold microheater structure was provided by a DC power supply (VLP 2403pro, Conrad Electronic, Hirschau, Germany) [49,70].

2.7. Data analysis and statistics

MATLAB software (versions of 2017b and then 2020b, MathWorks, Natick, MA, USA) was used to analyze the results of experiments with both integrated optical biosensor devices and to potentially visualize them. In these cases, the image processing toolbox functions: corr2() and immse() were applied. This software was also used to study and compare the scattered light intensity images of the electro-optical measurement concept [33,49].

In permeability assays and ELISAs used to study the passage of spike protein through barrier models (more details in section 2.5.), the measured data were plotted and analyzed by our colleagues using Excel (Microsoft, Redmond, WA, USA) and GraphPad Prism 5.0 softwares (GraphPad, San Diego, CA, USA). These results were shown as means ± SEM wherever it was relevant [49].

All the experiments, related to these two applications of different integrated optical biosensing approaches, were repeated at least twice [33,49].

3. Results and discussion

3.1. Electro-optical biosensor for bacteria detection

3.1.1. Dielectrophoretic cell collecting

To increase the sensitivity of bacterium detection by the electro-optical biosensor, DEP-based cell collection was performed. This technique was optimized prior to detection, with a construction consisting of thin-film surface-electrode pairs placed in the microfluidic channel. Initially, the pDEP-based particle collection capability and size-dependent selectivity (Eq.3) of this electrode system were studied in case of microbeads. For this purpose, MilliQ deionized water suspensions of the mixture of polystyrene microbeads of different diameters (1 μm, 9 μm) was used. During these experiments, the liquid sample was flowed through the channel at a rate of 5 μl/min while the current of a high AC electric (30 V peak-to-peak amplitude (V_{p-p}), 5 MHz) field was applied. These parameters, together with the low ionic strength of the applied liquid medium, assured that the desired positive dielectrophoretic collection could be achieved for these target particles. The obtained results demonstrated the usability of this method. Thus, a size-dependent, selective particle collection (Eq.7.) was achieved for polystyrene beads. In this case, beads with the desired diameter of 1 μm were moved to the surface of the gap between the electrodes, while the movement of the 9-μm beads was not affected by the applied electric field in the suspension of the mixture of beads of different diameters.

Based on the promising findings of these measurements, the next step was to collect the target bacterial cells, instead of polystyrene beads, from samples diluted with deionized water. Here, the difference in dielectric properties between non-virulent, live *Escherichia coli* cells and microbeads was needed to be considered. The experimental protocol followed the above-mentioned one, used in case of polystyrene beads. Different dilutions of bacterial suspensions were used to evaluate the performance of the cell-collection electrode system. During the process, the *E. coli* bacterial suspension was pumped through the channels at a flow rate of 5 μl/min, while using an alternating electric field for collecting the cells. As a first, general approach (used, e.g., for the optimization of the experimental parameters, see 3.1.2. section), bacteria were collected for 30 minutes by this technique. Nonetheless, subsequent studies were also carried out to further optimize, and reduce this period (for more details see 3.1.3. section). The cell-collection capability of the electrode system was tested with a bacterial suspension at a concentration of 10^6 CFU/ml. An efficient cell collection was observed in the flowing fluid sample, shortly after the application of the AC electric field. This was followed by experiments

with various further dilutions of *E. coli* samples (for further details, see calibration studies in 3.1.3. section). Even with a dilute bacterial suspension at a concentration of 10^4 CFU/ml, a high proportion of the cells were collected. Therefore, samples corresponding to this lower concentration were subsequently used in some steps of the optical detection process. For example, quantitative measurements were performed with such samples to optimize the crucial parameters of the detection system. This includes the selection of the applicable magnification and the frequency of the applied AC electric field.

3.1.2. Optimization of detection based on scattered evanescent waves

The dielectrophoretically captured bacteria were detected after the cell-collection step, based on the evanescent waves scattered on them. In this process, the alternating electric field was switched off ('OFF state') and then on ('ON state') periodically to modify the adhesion contact between the waveguide surface and the target cells. For this purpose, short, 1.4 s-long pulses were given with 3 s-long pauses to the AC field, applied to the electrodes. This resulted in a pattern change in the scattered light intensity images, which was recorded and analyzed, providing the basis for detection. Microscopic observations revealed that these differences were correlated, and they were associated with the movement of the bacteria caused by the switching of the alternating electric field. Here, it is important to note that several factors contributed to the successful bacteria detection. Firstly, appropriate pulse-timings were chosen so that the electric field offsets did not result the escape of the collected bacteria from the detection space. On the other hand, during these experiments, the fluid sample contained only bacteria (except the pilot test for selective bacteria detection, where somatic cells were also included (section 3.1.4.)). This technique (Figure 7) provided the basis for quantitative detection of bacterium cells with the device. To achieve this, the measurement process was followed by image acquisition from the same cross-section of the biosensor. During this step, image pairs were captured at different states of the system (OFF and ON). Considering the above-mentioned approaches, with a general cell collection time of 30 minutes, the total detection took around 40 minutes. Using this technique, image processing methods were applied to obtain quantitative results. For this purpose, variables were calculated to characterize the similarities and differences between patterns of scattered light intensity images registered in different states of the system. In this context, correlation and mean square error (MSE) values were found to be good candidates. Thus, these were calculated for each pair of captured images to describe the similarities between them in a script and a function, written in MATLAB2017b. The same calculations were performed to determine whether the scattered light intensity patterns changed

significantly between the OFF and ON conditions, using different images captured in the same state of the biosensor system, which images served as a control group. After describing the detection and analysis techniques, in the following, the different optimization tests are detailed.
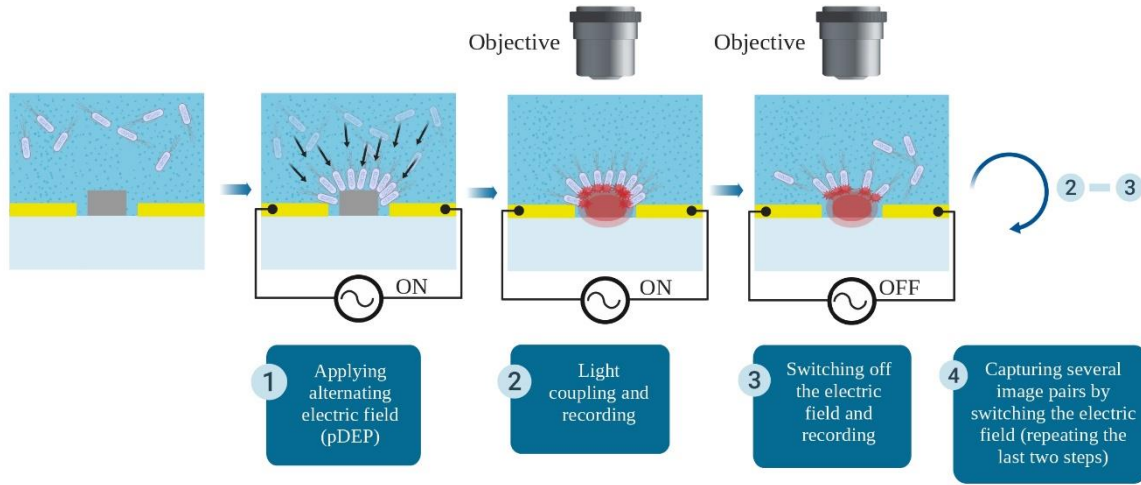

Figure 7. The detailed scheme of the electro-optical biosensor operation principle. The quantitative measurement is based on the analysis of the scattered evanescent wave intensity images, recorded during the switching of the inhomogeneous alternating electric field, inducing bacteria movement. Thus, a difference in the scattered image patterns is achieved, which can be used for image processing-based detection. The figure was created with BioRender.com.

Generally, the measurements were performed by microscopic observation of the system with an objective of 20x magnification. However, further tests were carried out to determine the applicable resolution at which the difference in the patterns of the recorded scattered light images could still be considered significant. For this purpose, these images were captured and analyzed using different magnification objectives (x4.7, x10, x20) (Figure 8). For demonstration purposes, the test sample was a diluted (10^4 CFU/ml) bacterial suspension, resulting in a large scattered light intensity pattern difference during detection. Analytical results of these images (number of image pairs: n = 5-12) showed that compared to the within-control group differences (Figure 9: 'Group'), there were significant between-group differences (Figure 9: 'Pairwise') in MSE values for image pairs (OFF-ON images) (Figure 9a-b). Furthermore, this high MSE value fluctuation was also maintained for images acquired with objectives of less magnification (x4,7, x10) (Figure 9a).

As a further optimization test of the electro-optical biosensor, the frequency selection of the alternating electric field applied in the pDEP-based cell collection process was examined to maximize the number of captured bacteria and thus the sensitivity. Therefore, to select the ideal frequency, experiments with its variation were performed, in the range between 100 kHz and 5 MHz, relevant for bacterial pDEP collection. In this study, using the quantitative image processing protocol (number of image pairs: n = 5-12), the frequency of 5 MHz gave the best

results for this purpose, which finding supported the sensitivity of the detection (Figure 9b). Consequently, cell collection in subsequent studies was performed with the applied electric field at this particular frequency (30 V_{p-p}, 5 MHz, sinusoidal signal).
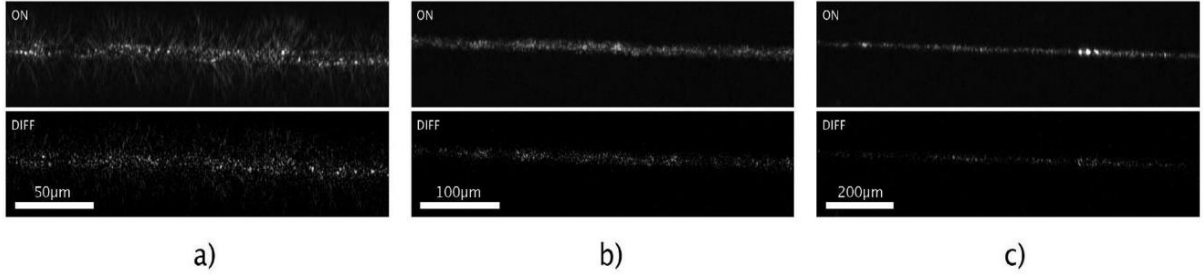

Figure 8. Captured scattered light intensity images during the optimization process, providing the basis of the quantitative measurements. After the cell-collecting step (10^4 CFU/ml *E. coli* suspension), images were taken at the corresponding state of the system during the electric field switch ('ON' state with applied AC field and 'OFF' state without it). For detection, objectives of different magnifications (x20 **(a)**, x10 **(b)**, and x4.7 **(c)**) were used. The scattered light intensity patterns of ON state images were then compared to that of the OFF ones by image processing, resulting an intensity difference ('DIFF').
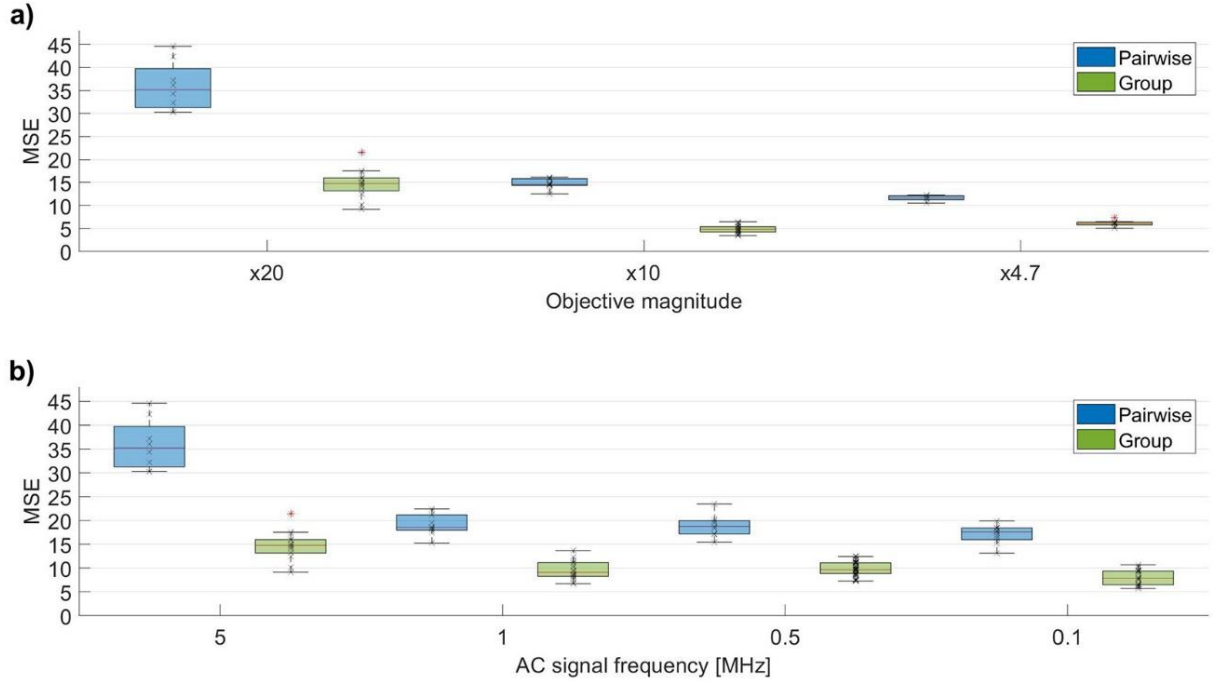
Figure 9. Quantitative results of the bacteria detection. Image analysis of the optimization processes: applicable objective magnifications **(a)** and AC frequencies **(b)** at a given *E. coli* concentration (10^4 CFU/ml). Image similarities for between-group values of image pairs as 'Pairwise', and for in-group values of image pairs as 'Group' were evaluated at the corresponding states (OFF - ON) of the system with the applied AC field (30 V_{p-p}, 5 MHz), at the same region of the system (n = 5–12). For quantification, the statistical value of mean-squared errors (MSE) was used for comparing the scattering patterns (x20 objective). The frequency optimization was performed with AC signal of 30 V_{p-p} amplitude and 0.1–5 MHz frequency range.

3.1.3. Detection limit of the electro-optical biosensor

Given the optimized measurement parameters (x20 objective, 30 V_{p-p}, 5 MHz, sinusoidal AC electric field), tests were performed to estimate the detection limit of the biosensor device. To this end, a dilution series of suspensions containing bacterial cells at a concentration of 10^2-10^6 CFU/ml was prepared. In parallel, further studies were also performed , using these samples, so as to determine a reduced cell-collection time for DEP, compared to the standard case of 30 mins, for which the most efficient detection of cells could be achieved. Consequently, scattered light intensity images were acquired for all bacterial suspensions in the dilution series. For this purpose, the cell collection times were: reference as 0 (n = 5), 1 (n = 10), 3 (n = 6-10), 10 (n = 19-20) and 30 (n = 20) minutes prior to optical detection. The obtained images were analyzed, and MSE image similarity values were calculated. This calculation was performed for each pair of images ('OFF' and 'ON' state) in connection with different states of the system ('Pairwise') showing between-group variation, and for each pair of group images related to a certain state of the system (only 'OFF' or only 'ON') indicating within-group variation ('Group'). A minimal cell-collection time of 10 min was estimated based on image processing results obtained during cell collection kinetic studies. Accordingly, this cell collection time was also used in the detection limit studies for the serially diluted bacterial samples.

In these measurements, the image processing results obtained for each suspension (n = 19-20) clearly indicated a significant difference between the MSE values of the 'Pairwise' images and the 'Group' images, even at the lowest bacterial concentration of 10^2 CFU/ml (Figure 10a). This MSE-value difference is indicative of the number of the collected bacteria. Consequently, the calibration of the biosensor could be achieved based on the parameter of mean MSE value difference (the difference between the 'Pairwise' and 'Group' means).The experiments were performed on the same biosensor for all bacterial suspensions, so that scattered light intensity images (n = 19-20) were recorded in both states of the system ('OFF' and 'ON') as a first step of the measurement process with a given device without cell collection (0 min cell-collection). Thus, a reference MSE value was determined (based on reference 'Pairwise' and 'Group' images) and used for calibration. Subsequently, this reference value was subtracted from each MSE value difference (Figure 10b). Finally, the calibration function could be determined by fitting a power-law function (multiplicative factor: 0.6152, exponent: 0.2228) to the obtained MSE difference values. It showed a good fit ($R^2 = 0.91$), thus it could be considered as a suitable curve for the calibration of the biosensor (Figure 10c).
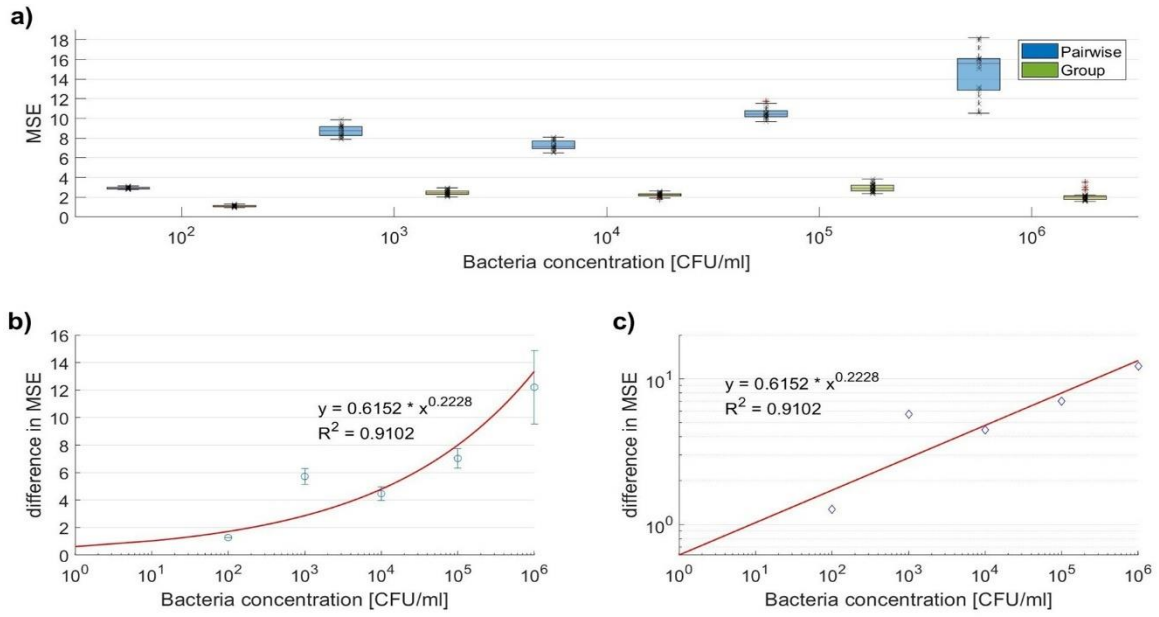
Figure 10. Results of the detection limit and calibration experiments. Image similarities for between-group values of image pairs as 'Pairwise', and for in-group values of image pairs as 'Group' were evaluated at the corresponding states (OFF - ON) of the system with the applied AC field of 30 V_{p-p} and 5 MHz, at its same region (n = 19-20, x20 objective). For the experiments images (n = 19–20) were taken in case of each sample of the serial diluted bacteria suspension ($10^2 - 10^6$ CFU/ml). As a quantitative descriptor of the image differences, mean-squared error (MSE) values between the scattering patterns were used **(a)**. **(b)** MSE values difference (mean±standard deviation) between 'Pairwise' and 'Group' images were calculated, which can be considered significant for the most diluted bacteria sample (10^2 CFU/ml), defining the detection limit of this novel biosensing method. Calibration curve could be defined by fitting a power-law function to the data ($R^2 = 0.91$). **(c)** Log-log representation of **(b)**, showing the goodness of the calibration curve fit.

3.1.4. Experiments with artificial urine containing somatic cells

The practical applicability of the DEP-based bacterium cell collection method was also tested in a medium modeling inflammatory urine infected with bacteria, and containing other somatic cell types, too. Therefore, the focus of this pilot study was on the selectivity of the cell collection procedure, where the system also contained the waveguide structure. For these measurements, artificial urine containing a mixture of *E. coli* (10^4 CFU/ml) and hCMEC/D3 endothelial cell suspensions was used. Also in these experiments, the alternating electric field was applied with the parameters mentioned above (30 V_{p-p}, 5 MHz). At the beginning of the process, the influence of the dielectrophoresis generated by the applied field on individual cells was investigated. Meanwhile, the fluid sample was pumped through the microfluidic channel at a slower flow rate of 0.1 µl/min over a few-minutes period. During this test, the effect occurred as expected. It was observed that the dielectrophoresis, due to its size and frequency dependence, had distinct effects on cells of different sizes for the selected frequency and ionic strength. Bacteria (~2 µm) were collected on the electrode surfaces, while endothelial cells (~10 µm) were repelled. In the second phase of the test, selective bacteria collection was performed

from this cell-mixture sample. At this time, a relatively higher flow rate of 3 µl/min was used. During the process, only bacterial cells were captured in large numbers at the end of the electrodes on the surface of the waveguides, whereas no endothelial cells were observed. The results of the pilot test demonstrated the ability of size-dependent selection of this DEP-based cell-collection method, whereby bacteria were collected in the detection region of the biosensor.

3.2. IO MZI biosensor for the detection of SARS-COV-2 spike protein (S1) permeability across *in vitro* human biological barrier models

The integrated optical biosensor was developed to ascertain the passage of the SARS-CoV-2 spike protein S1 subunit through a human brain endothelial cell culture BBB model [49]. The scientific topic of the passage of the virus and its subunits across biological barriers is a very actual and intensively researched topic in the context of the virus. Accordingly, the related research has not focused on the mechanism of virus or virus protein crossing the barrier systems, as this has been previously investigated. In BBB, spike protein treatment has previously been shown to alter barrier integrity and induce endothelial cell activation [71,72]. Nevertheless, the short-term spike protein S1 subunit treatment, detailed here, did not alter the resistance of the BBB model in the assays [49].

It was recently found that SARS-CoV-2 transcellularly crosses mouse and hamster primary brain endothelial cell-culture models without altering the expression of tight junctions [73]. It was suggested that the S1 subunit in mice passes through the BBB via adsorption-mediated transcytosis [47]. Additionally, for brain uptake in mice, ACE2 receptors were also shown to be important [47]. Previously, our colleagues found that only very low levels of ACE2 were expressed by the hECs in the present model [66,67].

As COVID-19 is also associated with gastrointestinal symptoms, a gut barrier culture system was implemented in the experimental setup. Therefore, as it was shown previously, Caco-2 cells express ACE2 receptor, thus providing a suitable model for studying spike protein with this biological barrier system [74]. Regarding TEER, it was found that its value was not altered after short-term treatment with spike protein in this epithelial model.

3.2.1. Thermo-optical bias-point adjustment

Thermo-optical bias-point tuning was applied to the Mach-Zehnder interferometer, based on a process first used and described in detail in a previous study of our research group [60]. This involved the initial investigation of the sinusoidal transfer function of the MZI. Then the voltage applied to the heating wire was steadily increased from 0 V to 4.6 V, while the light intensity

of the interferometer output was measured at the wavelength of the incident light. This was 633 nm for initial trials and 532 nm for practical measurements in the reported study [60]. In contrast, the current viral protein detection was carried out at the wavelength of 670 nm. As a result, in the above-mentioned process, a heating voltage of 0-4.6V at a wavelength of 532nm was able to tune the working point for the whole period of the output signal (Figure 11). In this technique, the heating causes a change in the local temperature of the waveguide environment, which leads to a modulation of the output light intensity by shifting the phase of the light propagating in the reference arm of the MZI (described in detail in section 1.2.3. of the introduction). The sensitivity of the interferometer is proportional to the first derivative of its sinusoidal transfer function, so that it is smaller at the extremes and largest at the inflection point. Thus, the offset voltage can be used to artificially set the output to the average light-level ('zero-intensity points' in Figure 11) prior to the measurements, where the derivative is largest, and hence the sensitivity, too. The power output of the heater can be then fine-tuned by setting this bias point to one of the points of maximum sensitivity. In addition to artificial heating, changes in the environmental conditions (such as temperature and humidity) can also cause baseline drift, the effects of which will result in a decrease in the responsivity of the detection. However, the bias-point adjustment can compensate for these. With applying appropriate direct current and taking the environmental parameters into account, the baseline drift can be kept to negligible levels during the protein detection time (on the scale of a few minutes). Hence, results obtained with such devices of slightly different sensitivity could be compared [49].
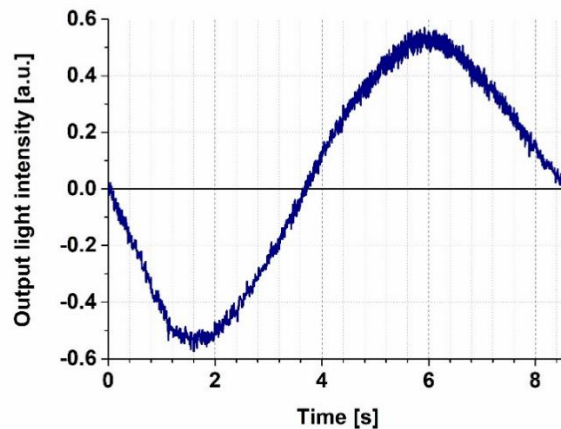

Figure 11. IO MZI response, showing its transmission function during thermo-optical biasing prior to each experiment. The output signal was recorded by a 532 nm probe light, while the bias point was adjusted to the zero level. In the process, heating voltage was increased steadily from 0 to 4.6 V. In case of viral protein detection (at 670 nm wavelength measuring light) 1-1.5 V was applied to the microheater for biasing, typically.

3.2.2. Measurements with the optical biosensor

The microchannels were first filled with a buffer solution (30 µl/min) prior to the measurements. Meanwhile the operating point of the integrated optical MZI was adjusted by applying adirect current to the heating wire as a starting point. Then, the measurements were performed by flowing the target protein solutions through the microchannel of the interferometer (3 µl/min). For this purpose, the upper or lower arm of the MZI was used, while the other remained intact as a reference. By using two distinct arms for measuring, the output signal of the biased interferometer varied with a different sign, so that the results obtained with different measurements were evaluated with the same positive sign (Figure 12). As an initial step of the measurements, two control samples with specific spike protein concentrations (2 and 20 µg/ml in 0.1% BSA-RH buffer, Figure 12) were used to calibrate the corresponding biosensor. Subsequently, the detection of the S1 subunit of the target spike protein (Figure 12) was performed from fluid samples obtained from the lower insert compartments of the permeability assays for both cell culture models (BBB co-culture and Caco-2 cell culture). Additional permeability-assay control samples were also measured, such as protein-free buffer solution ('0.1% BSA-RH' on Figure 12) for the Caco-2 model as a negative control, and the sample from cell-free inserts ('empty control' on Figure 12) for the BBB model, containing spike proteins at the initial concentration, as a positive control.
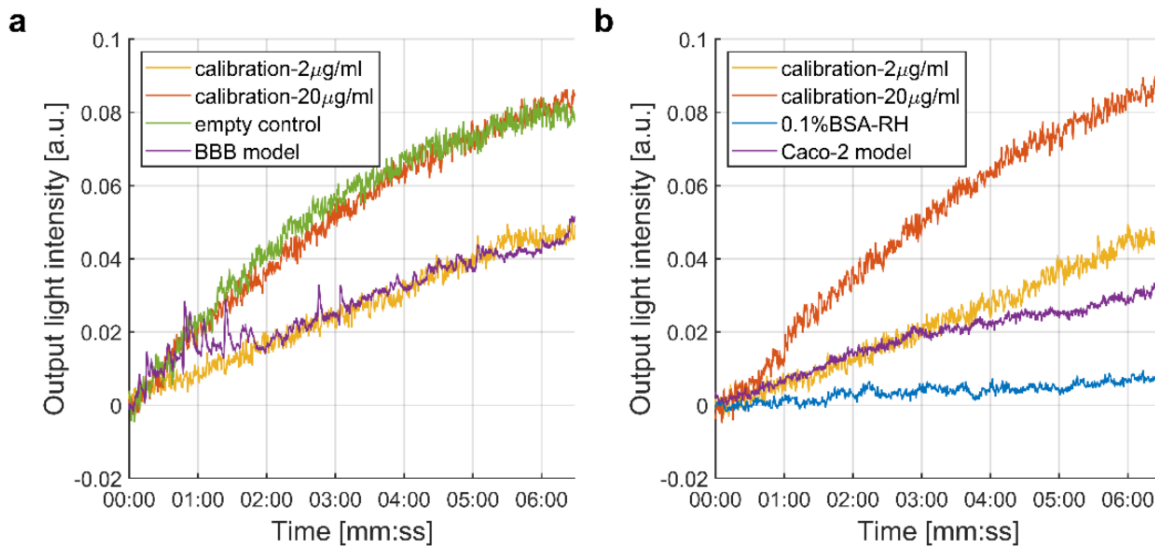

Figure 12. Integrated optical MZI biosensing results of barrier-crossed spike S1 amounts for BBB **(a)** and Caco-2 monolayer **(b)**. For device calibration, samples of different protein concentrations (2 and 20 µg/mL) were used. While signals were also detected in case of control samples: for positive control samples (BBB model), obtained for cell-free cell culture inserts ('empty control'); and for negative control samples (Caco-2 model) from buffer (0.1% BSA-RH).

The negative-control buffer solution (Figure 12b: 0.1% BSA-RH), containing no target protein, resulted background signals as it did not cause a significant change in the output intensity. While for the positive control, cell-free cell-culture inserts (Figure 12a: 'empty control') achieved high peak amplitudes. This proved to be similar to that of the more concentrated calibration sample (20 µg/ml). The calibration samples with the above-mentioned protein concentrations of 20 and 2 µg/ml gave comparable signals with the samples derived from the permeability assays (Figure 12b). In contrast, however, the two barrier models showed different evaluated protein concentrations of the target solutions. Namely, in the case of the BBB model, the biosensor signal was close to that of the 2 µg/ml calibration solution. Meanwhile, in the case of Caco-2 cells, it was lower.

As shown in Figure 12, the spike-protein concentration in the buffer, derived from the basal side of the blood-brain barrier model, was estimated to be 2 µg/ml. However, for the Caco-2 model, this concentration was lower. To estimate the accurate spike protein concentration from fluid samples, an assumption was made. Namely, the response function of the biosensor follows the Freundlich isotherm, an equation typical for a wide range of physical adsorption processes from solutions [75]:

$$\log m_{ad} = K + \left(\frac{1}{n}\right) - \log C \qquad \text{(Eq.9.)}$$

where m_{ad} is the relative adsorbed mass, and C is the bulk concentration of the analyte, whereas constant K and n are given at the corresponding temperature. Based on the measured calibration curves at the preset concentrations, K = 0,3653 and n = 3,3219. Meanwhile the values of m_{ad} and C are expressed in the units shown in Figure 12. Consequently, the concentration of the S1 spike protein subunit passing the intestinal barrier (Caco-2 cells) was found to be approximately 0.5 µg/ml using these calibration values. Such an observed reduced passage of spike protein subunit S1 in the case of the Caco-2 cell model could be attributed to either tighter connections between the cells indicated by the higher basal TEER values, or to different receptor expression and alternative passage pathways in epithelial cells.

The spike protein concentration values obtained by optical biosensing in the fluid samples derived from the permeability assay, corroborate the results obtained by ELISA (see Annex). Consequently, label-free, specific, sensitive detection of spike protein passage through barrier systems was achieved in a measurement time of only a few minutes. Furthermore, this IO MZI biosensor has the inherent portability and can be prepared in a cost-effective manner, which also facilitates its use as a POC testing tool for early, effective detection of the virus, or related

proteins. The practical usability of this optical biosensing approach is demonstrated by the fact that other similar integrated optical silicon-based interferometric biosensors have been under development for the detection of intact SARS-COV-2 virus or its subunits from saliva or nasopharyngeal fluid samples [50,76]. Such devices can be used to detect a variety of proteins, small-molecules [77], glycolipids [78] and nucleic acids in the aM-fM range [50,79].

4. Conclusion

As a first objective of my PhD work, an integrated electro-optical biosensor was designed, fabricated and its image-based, label-free, rapid bacteria detection working principle was demonstrated with live, non-virulent *E. coli* bacterial suspensions. The sensing concept was based on bacteria detection via the evanescent field, in the vicinity of waveguide structures. The sensitivity of this technique was enhanced by the application of dielectrophoresis, thus collecting the target cells on the waveguide surface, prior to detection. In the sensing process, the statistical analysis was performed based on the differences between the scattered light intensity images, where mean-square error variable was suitable to provide quantitative results. Based on this, calibration of the device could be performed reliably. The detection method does not require such resolution that is necessary to observe individual cells, since the differences in scattering patterns are providing suitable basis for efficient sensing. Through this image processing approach, the frequency of the AC field used for dielectrophoretic cell collection was optimized. Furthermore, I have shown that reliable image processing results can be obtained with the use of objective of similar magnification (x4.7) to a low-cost web camera, supporting the cost-effective implementation of this device. The performance of the presented detection concept was shown to be promising, reaching a detection limit of 10^2 CFU/ml. It is, on one hand, comparable to results obtained with other IO biosensors – e.g., OWLS, SPR, MZI – [37,80,81]; on the other hand, relevant for the concentration of some pathogens in body fluids, e.g. urine [82]. In addition, the 10-mins-long detection process, including cell collection, could be considered rapid, being considerably shorter than the time, required for performing traditional PCR or ELISA bacterial screening laboratory techniques [83]. Nevertheless, in its present form, the biosensor provided only unspecific detection. Yet, just as it was demonstrated in the case of an inflammation-mimicking fluid sample of artificial urine-containing somatic cells (hCMEC/D3 endothelial cells), selective detection of bacteria can also be achieved. One of the bases for this was the cell-size and frequency-dependent variation of the dielectrophoresis sign, and thus its effect on different cells. To overcome the limitation of the unspecific bacterium binding on the sensor surface, its functionalization can also be utilized. Moreover, the image analysis can be further developed. Nevertheless, based on the demonstration of this proof-of-concept detection method, this biosensor design has some promising aspects regarding its sensitivity, low cost of fabrication, and rapid detection process. These could all contribute to its application as a point-of-care diagnostic test in the future.

In the second objective of my studies, an integrated optical Mach-Zehnder interferometer-based biosensor was realized to be applied in a study focusing on the evaluation of the barrier-penetration capability of the SARS-CoV-2 surface spike protein S1 subunit. To model this, two *in vitro* biological barrier systems of human organs highly exposed to coronavirus infection were used. Therefore, blood-brain barrier and intestinal barrier cell-culture systems were investigated. Permeability assays were performed in inserts, then fluids within their bottom compartments were further used for quantitative detection of the amount of crossed protein by the biosensor. The presented optical biosensing approach provided a sensitive, specific, and rapid way of S1-protein sensing, whereas the device has the potential to be used as a portable diagnostic tool. For its optimal operation, the bias point of the interferometer was adjusted effectively, using the developed thermo-optical technique. Therefore, the sensitivity of the device could be maintained during the measurements. Beside the optical biosensing approach, ELISA was also performed to quantitatively determine and compare the penetration capability of the spike protein S1 subunit for both cell culture models, validating the results obtained with the biosensor at the same time. Based on the obtained results, the penetration phenomenon was verified, whereas the S1 could cross the two barriers in different amounts. Furthermore, the biosensing approach also allowed the precise quantification of such target proteins. For further studies aiming at the investigation of pathological effects of SARS-CoV-2 on human body, the applied *in vitro* barrier models, methods, and detection approaches could serve as a valuable basis. Based on the obtained results of the integrated optical Mach-Zehnder interferometer biosensor, this sensing approach was proved to be applicable for such a medical diagnostic purpose.

Acknowledgements

I would like to thank Dr. András Dér, Head of the Biomolecular Electronics Research Group, and Dr. Sándor Valkai for giving me the opportunity to work under their supervision at the Institute of Biophysics of the Biological Research Centre. I also thank them for their teaching and guidance throughout my undergraduate and doctoral years.

I would like to express my appreciation to my colleagues, Prof. Dr. Mária Deli, Head of the Biological Barriers Research Group, and Dr. Fruzsina Walter, Dr. Ana Raquel Santa Maria, Judit Vigh, Anna Kocsis and Szilvia Krekic for their work and support during our collaborations.

I would also like to thank the members of the Biomolecular Electronics and Biophotonics and Biomicrofluidics Research Groups and all the colleagues of the Institute of Biophysics. I received generous support and help from Dr. András Kincses, Ágnés Ábrahám, Dr. Krisztina Nagy, Dr. Gaszton Vizsnyiczai, Dr. Tamás Fekete, Dr. Lóránd Kelemen, László Dér, Dr. Péter Galajda, and Dr. László Zimányi.

Furthermore, I would like to thank Dr. Anna Mathesz and Dr. László Fábián, who helped me to gain insight into the research topic and gave me advice at the beginning of my research.

I am deeply thankful for the support of my family, especially my love, Adrienn Mányai, my father, Pál Petrovszki and my brother, Péter Petrovszki. Without their support this thesis would never have been accomplished. I would like to dedicate this work to my late mother.

References

1. González-Guerrero, A.B.; Maldonado, J.; Herranz, S.; Lechuga, L.M. Trends in Photonic Lab-on-Chip Interferometric Biosensors for Point-of-Care Diagnostics. *Analytical Methods* **2016**, *8*, 8380–8394, doi:10.1039/C6AY02972H.

2. PubMed Webpage, Searching for the Term "Biosensor" Available online: https://pubmed.ncbi.nlm.nih.gov/?term=biosensor (accessed on 27 January 2023).

3. Luong, J.H.T.; Male, K.B.; Glennon, J.D. Biosensor Technology: Technology Push versus Market Pull. *Biotechnol Adv* **2008**, *26*, 492–500, doi:10.1016/j.biotechadv.2008.05.007.

4. Kozma, P.; Kehl, F.; Ehrentreich-Förster, E.; Stamm, C.; Bier, F.F. Integrated Planar Optical Waveguide Interferometer Biosensors: A Comparative Review. *Biosens Bioelectron* **2014**, *58*, 287–307, doi:10.1016/j.bios.2014.02.049.

5. Merkoçi, A.; Li, C.; Lechuga, L.M.; Ozcan, A. COVID-19 Biosensing Technologies. *Biosens Bioelectron* **2021**, *178*, 113046, doi:10.1016/j.bios.2021.113046.

6. Torrijos-Morán, L.; Lisboa, B.D.; Soler, M.; Lechuga, L.M.; García-Rupérez, J. Integrated Optical Bimodal Waveguide Biosensors: Principles and Applications. *Results in Optics* **2022**, *9*, 100285, doi:10.1016/j.rio.2022.100285.

7. Chin, C.D.; Linder, V.; Sia, S.K. Lab-on-a-Chip Devices for Global Health: Past Studies and Future Opportunities. *Lab Chip* **2007**, *7*, 41–57, doi:10.1039/b611455e.

8. Ligler, F.S. Perspective on Optical Biosensors and Integrated Sensor Systems. *Anal Chem* **2009**, *81*, doi:10.1021/ac8016289.

9. Duval, D.; González-Guerrero, A.B.; Dante, S.; Osmond, J.; Monge, R.; Fernández, L.J.; Zinoviev, K.E.; Domínguez, C.; Lechuga, L.M. Nanophotonic Lab-on-a-Chip Platforms Including Novel Bimodal Interferometers, Microfluidics and Grating Couplers. *Lab Chip* **2012**, *12*, 1987, doi:10.1039/c2lc40054e.

10. Lafleur, J.P.; Jönsson, A.; Senkbeil, S.; Kutter, J.P. Recent Advances in Lab-on-a-Chip for Biosensing Applications. *Biosens Bioelectron* **2016**, *76*, 213–233, doi:10.1016/j.bios.2015.08.003.

11. Fan, X.; White, I.M.; Shopova, S.I.; Zhu, H.; Suter, J.D.; Sun, Y. Sensitive Optical Biosensors for Unlabeled Targets: A Review. *Anal Chim Acta* **2008**, *620*, 8–26, doi:10.1016/j.aca.2008.05.022.

12. Cooper, M.A. Optical Biosensors in Drug Discovery. *Nat Rev Drug Discov* **2002**, *1*, 515–528, doi:10.1038/nrd838.

13. Bahadir, E.B.; Sezgintürk, M.K. A Review on Impedimetric Biosensors. *Artif Cells Nanomed Biotechnol* **2016**, *44*, 248–262, doi:10.3109/21691401.2014.942456.

14. Luo, X.; Davis, J.J. Electrical Biosensors and the Label Free Detection of Protein Disease Biomarkers. *Chem Soc Rev* **2013**, *42*, 5944, doi:10.1039/c3cs60077g.

15. Margalit, N.; Xiang, C.; Bowers, S.M.; Bjorlin, A.; Blum, R.; Bowers, J.E. Perspective on the Future of Silicon Photonics and Electronics. *Appl Phys Lett* **2021**, *118*, 220501, doi:10.1063/5.0050117.

16. Thylén, L.; Wosinski, L. Integrated Photonics in the 21st Century. *Photonics Res* **2014**, *2*, 75, doi:10.1364/PRJ.2.000075.

17. Kogelnik, H. Theory of Optical Waveguides. In; 1988; pp. 7–88.

18. Saleh, B.E.A.; Teich, M.C. *Fundamentals of Photonics*; Wiley Series in Pure and Applied Optics; John Wiley & Sons, Inc.: New York, USA, 1991; ISBN 0471839655.

19. Fábián, L.; Mathesz, A.; Dér, A. New Trends in Biophotonics. *Acta Biologica Szegediensis* 2015, *59*.

20. Tiefenthaler, K.; Lukosz, W. Sensitivity of Grating Couplers as Integrated-Optical Chemical Sensors. *Journal of the Optical Society of America B* **1989**, *6*, 209, doi:10.1364/JOSAB.6.000209.

21. Estevez, M.C.; Alvarez, M.; Lechuga, L.M. Integrated Optical Devices for Lab-on-a-Chip Biosensing Applications. *Laser Photon Rev* **2012**, *6*, 463–487, doi:10.1002/lpor.201100025.

22. Horvath, R.; Pedersen, H.C.; Skivesen, N.; Selmeczi, D.; Larsen, N.B. Monitoring of Living Cell Attachment and Spreading Using Reverse Symmetry Waveguide Sensing. *Appl Phys Lett* **2005**, *86*, 071101, doi:10.1063/1.1862756.

23. Courjon, D.; Sarayeddine, K.; Spajer, M. Scanning Tunneling Optical Microscopy. *Opt Commun* **1989**, *71*, 23–28, doi:10.1016/0030-4018(89)90297-6.

24. Fish, K.N. Total Internal Reflection Fluorescence (TIRF) Microscopy. *Curr Protoc Cytom* **2009**, *50*, doi:10.1002/0471142956.cy1218s50.

25. Huertas, C.S.; Calvo-Lozano, O.; Mitchell, A.; Lechuga, L.M. Advanced Evanescent-Wave Optical Biosensors for the Detection of Nucleic Acids: An Analytic Perspective. *Front Chem* **2019**, *7*, doi:10.3389/fchem.2019.00724.

26. Sun, S.; He, M.; Xu, M.; Gao, S.; Chen, Z.; Zhang, X.; Ruan, Z.; Wu, X.; Zhou, L.; Liu, L.; et al. Bias-Drift-Free Mach–Zehnder Modulators Based on a Heterogeneous Silicon and Lithium Niobate Platform. *Photonics Res* **2020**, *8*, 1958, doi:10.1364/PRJ.403167.

27. Densmore, A.; Janz, S.; Ma, R.; Schmid, J.H.; Xu, D.-X.; Delâge, A.; Lapointe, J.; Vachon, M.; Cheben, P. Compact and Low Power Thermo-Optic Switch Using Folded Silicon Waveguides. *Opt Express* **2009**, *17*, doi:10.1364/oe.17.010457.

28. Sun, H.; Qiao, Q.; Guan, Q.; Zhou, G. Silicon Photonic Phase Shifters and Their Applications: A Review. *Micromachines (Basel)* **2022**, *13*, 1509, doi:10.3390/mi13091509.

29. Lifante, G. *Integrated Photonics: Fundamentals*; 2003;

30. Iizuka, K. *Elements of Photonics, Volume II*; Wiley Series in Pure and Applied Optics; John Wiley & Sons, Inc.: New York, USA, 2002; Vol. 2; ISBN 0471408158.

31. Lifante, G. Introduction to Integrated Photonics. In *Integrated Photonics: Fundamentals*; 2005.

32. Zourob, M.; Mohr, S.; Treves Brown, B.J.; Fielden, P.R.; McDonnell, M.B.; Goddard, N.J. An Integrated Optical Leaky Waveguide Sensor with Electrically Induced Concentration System for the Detection of Bacteria. *Lab Chip* **2005**, *5*, 1360–1365, doi:10.1039/b504938e.

33. Petrovszki, D.; Valkai, S.; Gora, E.; Tanner, M.; Bányai, A.; Fürjes, P.; Dér, A. An Integrated Electro-Optical Biosensor System for Rapid, Low-Cost Detection of Bacteria. *Microelectron Eng* **2021**, *239–240*, doi:10.1016/j.mee.2021.111523.

34. Horváth, R.; Pedersen, H.C.; Skivesen, N.; Selmeczi, D.; Larsen, N.B. Optical Waveguide Sensor for On-Line Monitoring of Bacteria. *Opt Lett* **2003**, *28*, 1233, doi:10.1364/ol.28.001233.

35. Cooper, I.R.; Meikle, S.T.; Standen, G.; Hanlon, G.W.; Santin, M. The Rapid and Specific Real-Time Detection of Legionella Pneumophila in Water Samples Using Optical Waveguide Lightmode Spectroscopy. *J Microbiol Methods* **2009**, *78*, 40–44, doi:https://doi.org/10.1016/j.mimet.2009.04.004.

36. Tawil, N.; Sacher, E.; Mandeville, R.; Meunier, M. Surface Plasmon Resonance Detection of E. Coli and Methicillin-Resistant S. Aureus Using Bacteriophages. *Biosens Bioelectron* **2012**, *37*, 24–29, doi:10.1016/j.bios.2012.04.048.

37. Mathesz, A.; Valkai, S.; Újvárosy, A.; Aekbote, B.; Sipos, O.; Stercz, B.; Kocsis, B.; Szabó, D.; Dér, A. Integrated Optical Biosensor for Rapid Detection of Bacteria. *Optofluidics, Microfluidics and Nanofluidics* **2015**, *2*, 15, doi:10.1515/optof-2015-0002.

38. Sarkar, D.; Gunda, N.S.K.; Jamal, I.; Mitra, S.K. Optical Biosensors with an Integrated Mach-Zehnder Interferometer for Detection of Listeria Monocytogenes. *Biomed Microdevices* **2014**, *16*, 509–520, doi:10.1007/s10544-014-9853-5.

39. Micro Identification Technologies Ltd. Official Website. MIT 1000 from Micro Imaging Technology (MIT) Product Description. **2023**.

40. Leggett, H.C.; Cornwallis, C.K.; West, S.A. Mechanisms of Pathogenesis, Infective Dose and Virulence in Human Parasites. *PLoS Pathog* **2012**, *8*, e1002512, doi:10.1371/journal.ppat.1002512.

41. Rahal, E.A.; Kazzi, N.; Nassar, F.J.; Matar, G.M. Escherichia Coli O157:H7—Clinical Aspects and Novel Treatment Approaches. *Front Cell Infect Microbiol* **2012**, *2*, doi:10.3389/fcimb.2012.00138.

42. Nalbandian, A.; Sehgal, K.; Gupta, A.; Madhavan, M. v.; McGroder, C.; Stevens, J.S.; Cook, J.R.; Nordvig, A.S.; Shalev, D.; Sehrawat, T.S.; et al. Post-Acute COVID-19 Syndrome. *Nat Med* 2021, *27*.

43. Solomon, T. Neurological Infection with SARS-CoV-2 — the Story so Far. *Nat Rev Neurol* 2021, *17*.

44. Baig, A.M. Counting the Neurological Cost of COVID-19. *Nat Rev Neurol* 2022, *18*.

45. Ogata, A.F.; Cheng, C.-A.; Desjardins, M.; Senussi, Y.; Sherman, A.C.; Powell, M.; Novack, L.; Von, S.; Li, X.; Baden, L.R.; et al. Circulating Severe Acute Respiratory Syndrome Coronavirus 2 (SARS-CoV-2) Vaccine Antigen Detected in the Plasma of MRNA-1273 Vaccine Recipients. *Clinical Infectious Diseases* **2021**, *2*, doi:10.1093/cid/ciab465.

46. Kiss, B.; Kis, Z.; Pályi, B.; Kellermayer, M.S.Z. Topography, Spike Dynamics, and Nanomechanics of Individual Native SARS-CoV-2 Virions. *Nano Lett* **2021**, *21*, doi:10.1021/acs.nanolett.0c04465.

47. Rhea, E.M.; Logsdon, A.F.; Hansen, K.M.; Williams, L.M.; Reed, M.J.; Baumann, K.K.; Holden, S.J.; Raber, J.; Banks, W.A.; Erickson, M.A. The S1 Protein of SARS-CoV-2 Crosses the Blood–Brain Barrier in Mice. *Nat Neurosci* **2021**, *24*, 368–378, doi:10.1038/s41593-020-00771-8.

48. Singh, V.; Allawadhi, P.; Khurana, A.; Banothu, A.K.; Bharani, K.K. Critical Neurological Features of COVID-19: Role of Imaging Methods and Biosensors for Effective Diagnosis. *Sensors International* **2021**, *2*, 100098, doi:10.1016/j.sintl.2021.100098.

49. Petrovszki, D.; Walter, F.R.; Vigh, J.P.; Kocsis, A.; Valkai, S.; Deli, M.A.; Dér, A. Penetration of the SARS-CoV-2 Spike Protein across the Blood–Brain Barrier, as Revealed by a Combination of a Human Cell Culture Model System and Optical Biosensing. *Biomedicines* **2022**, *10*, 188, doi:10.3390/biomedicines10010188.

50. Soler, M.; Estevez, M.C.; Cardenosa-Rubio, M.; Astua, A.; Lechuga, L.M. How Nanophotonic Label-Free Biosensors Can Contribute to Rapid and Massive Diagnostics of Respiratory Virus Infections: COVID-19 Case. *ACS Sens* **2020**, *5*, 2663–2678, doi:10.1021/acssensors.0c01180.

51. Allsoppt, D.W.E.; Milner, K.R.; Brown, A.P.; Betts, W.B. Impedance Technique for Measuring Dielectrophoretic Collection of Microbiological Particles. *J Phys D Appl Phys* **1999**, *32*, doi:10.1088/0022-3727/32/9/319.

52. Demircan, Y.; Özgür, E.; Külah, H. Dielectrophoresis: Applications and Future Outlook in Point of Care. *Electrophoresis* 2013, *34*.

53. Jen, C.P.; Weng, C.H.; Huang, C. te Three-Dimensional Focusing of Particles Using Negative Dielectrophoretic Force in a Microfluidic Chip with Insulating Microstructures and Dual Planar Microelectrodes. *Electrophoresis* **2011**, *32*, 2428–2435, doi:10.1002/elps.201100085.

54. Páez-Avilés, C.; Juanola-Feliu, E.; Punter-Villagrasa, J.; del Moral Zamora, B.; Homs-Corbera, A.; Colomer-Farrarons, J.; Miribel-Català, P.L.; Samitier, J. Combined Dielectrophoresis and Impedance Systems for Bacteria Analysis in Microfluidic On-Chip Platforms. *Sensors (Switzerland)* **2016**, *16*, doi:10.3390/s16091514.

55. Hamada, R.; Takayama, H.; Shonishi, Y.; Hisajima, T.; Mao, L.; Nakano, M.; Suehiro, J. Improvement of Dielectrophoretic Impedance Measurement Method by Bacterial Concentration Utilizing Negative Dielectrophoresis. In Proceedings of the Journal of Physics: Conference Series; 2011; Vol. 307.

56. Lapizco-Encinas, B.H.; Simmons, B.A.; Cummings, E.B.; Fintschenko, Y. Dielectrophoretic Concentration and Separation of Live and Dead Bacteria in an Array of Insulators. *Anal Chem* **2004**, *76*, 1571–1579, doi:10.1021/ac034804j.

57. Miled, M.A.; Sawan, M. Dielectrophoresis-Based Integrated Lab-on-Chip for Nano and Micro-Particles Manipulation and Capacitive Detection. In Proceedings of the IEEE Transactions on Biomedical Circuits and Systems; 2012; Vol. 6.

58. Yang, L.; Bashir, R. Electrical/Electrochemical Impedance for Rapid Detection of Foodborne Pathogenic Bacteria. *Biotechnol Adv* 2008, *26*.

59. Dastider, S.G.; Abdullah, A.; Jasim, I.; Yuksek, N.S.; Dweik, M.; Almasri, M. Low Concentration E. Coli O157:H7 Bacteria Sensing Using Microfluidic MEMS Biosensor. *Review of Scientific Instruments* **2018**, *89*, doi:10.1063/1.5043424.

60. Petrovszki, D.; Krekic, S.; Valkai, S.; Heiner, Z.; Dér, A. All-Optical Switching Demonstrated with Photoactive Yellow Protein Films. *Biosensors (Basel)* **2021**, *11*, 432, doi:10.3390/bios11110432.

61. Prajzler, V.; Nekvindova, P.-; Hybs, P.; Jerabek, V. Properties of the Optical Planar Polymer Waveguides Deposited on Printed Circuit Boards. *Radioengineering* **2015**, *24*, 442–448, doi:10.13164/re.2015.0442.

62. Microresist Technology GmbH Official Website, EpoCore & EpoClad Series Datasheet Available online: https://www.microresist.de/en/produkt/epocore-epoclad-series/ (accessed on 27 January 2023).

63. Microresist Technology GmbH Official Website, SU-8 2000 Series Datasheet Available online: https://www.microresist.de/en/produkt/su-8-2000-series/ (accessed on 27 January 2023).

64. Kayaku Advanced Materials, Inc. Official Website, Products for Waveguides Available online: https://kayakuam.com/products/waveguides/ (accessed on 27 January 2023).

65. Khan, L.B.; Read, H.M.; Ritchie, S.R.; Proft, T. Artificial Urine for Teaching Urinalysis Concepts and Diagnosis of Urinary Tract Infection in the Medical Microbiology Laboratory †. *J Microbiol Biol Educ* **2017**, *18*, 1–6, doi:10.1128/jmbe.v18i2.1325.

66. Cecchelli, R.; Aday, S.; Sevin, E.; Almeida, C.; Culot, M.; Dehouck, L.; Coisne, C.; Engelhardt, B.; Dehouck, M.P.; Ferreira, L. A Stable and Reproducible Human Blood-Brain Barrier Model Derived from Hematopoietic Stem Cells. *PLoS One* **2014**, *9*, doi:10.1371/journal.pone.0099733.

67. Santa-Maria, A.R.; Walter, F.R.; Figueiredo, R.; Kincses, A.; Vigh, J.P.; Heymans, M.; Culot, M.; Winter, P.; Gosselet, F.; Dér, A.; et al. Flow Induces Barrier and Glycocalyx-Related Genes and Negative Surface Charge in a Lab-on-a-Chip Human Blood-Brain Barrier Model. *Journal of Cerebral Blood Flow and Metabolism* **2021**, *41*, doi:10.1177/0271678X21992638.

68. Vigh, J.P.; Kincses, A.; Ozgür, B.; Walter, F.R.; Santa-Maria, A.R.; Valkai, S.; Vastag, M.; Neuhaus, W.; Brodin, B.; Dér, A.; et al. Transendothelial Electrical Resistance Measurement across the Blood–Brain Barrier: A Critical Review of Methods. *Micromachines (Basel)* **2021**, *12*, 685, doi:10.3390/mi12060685.

69. Sipos, E.; Kurunczi, A.; Fehér, A.; Penke, Z.; Fülöp, L.; Kasza, Á.; Horváth, J.; Horvát, S.; Veszelka, S.; Balogh, G.; et al. Intranasal Delivery of Human β-Amyloid Peptide in Rats: Effective Brain Targeting. *Cell Mol Neurobiol* **2010**, *30*, doi:10.1007/s10571-009-9463-6.

70. Petrovszki, D.; Krekic, S.; Valkai, S.; Heiner, Z.; Dér, A. All-Optical Switching Demonstrated with Photoactive Yellow Protein Films. *Biosensors (Basel)* **2021**, *11*, 432, doi:10.3390/bios11110432.

71. Buzhdygan, T.P.; DeOre, B.J.; Baldwin-Leclair, A.; Bullock, T.A.; McGary, H.M.; Khan, J.A.; Razmpour, R.; Hale, J.F.; Galie, P.A.; Potula, R.; et al. The SARS-CoV-2 Spike Protein Alters Barrier Function in 2D Static and 3D Microfluidic in-Vitro Models of the Human Blood–Brain Barrier. *Neurobiol Dis* **2020**, *146*, 105131, doi:10.1016/j.nbd.2020.105131.

72. DeOre, B.J.; Tran, K.A.; Andrews, A.M.; Ramirez, S.H.; Galie, P.A. SARS-CoV-2 Spike Protein Disrupts Blood–Brain Barrier Integrity via RhoA Activation. *Journal of Neuroimmune Pharmacology* **2021**, doi:10.1007/s11481-021-10029-0.

73. Zhang, L.; Zhou, L.; Bao, L.; Liu, J.; Zhu, H.; Lv, Q.; Liu, R.; Chen, W.; Tong, W.; Wei, Q.; et al. SARS-CoV-2 Crosses the Blood–Brain Barrier Accompanied with Basement Membrane Disruption without Tight Junctions Alteration. *Signal Transduct Target Ther* **2021**, *6*, 337, doi:10.1038/s41392-021-00719-9.

74. Erickson, M.A.; Rhea, E.M.; Knopp, R.C.; Banks, W.A. Interactions of SARS-CoV-2 with the Blood–Brain Barrier. *Int J Mol Sci* **2021**, *22*, 2681, doi:10.3390/ijms22052681.

75. Freundlich, H. Über Die Adsorption in Lösungen. *Zeitschrift für Physikalische Chemie* **1907**, *57U*, doi:10.1515/zpch-1907-5723.

76. Combating 2019-NCoV: Advanced Nanobiosensing Platforms for POC Global Diagnostics and Surveillance | CoNVat Project | H2020 | CORDIS | European Commission. Https://Cordis.Europa.Eu/Project/Id/101003544/ (Accessed on 29 January 2023.).

77. Chocarro-Ruiz, B.; Fernández-Gavela, A.; Herranz, S.; Lechuga, L.M. Nanophotonic Label-Free Biosensors for Environmental Monitoring. *Curr Opin Biotechnol* **2017**, *45*, 175–183, doi:10.1016/j.copbio.2017.03.016.

78. Ramirez-Priego, P.; Martens, D.; Elamin, A.A.; Soetaert, P.; van Roy, W.; Vos, R.; Anton, B.; Bockstaele, R.; Becker, H.; Singh, M.; et al. Label-Free and Real-Time Detection of Tuberculosis in Human Urine Samples Using a Nanophotonic Point-of-Care Platform. *ACS Sens* **2018**, *3*, doi:10.1021/acssensors.8b00393.

79. Huertas, C.S.; Fariña, D.; Lechuga, L.M. Direct and Label-Free Quantification of Micro-RNA-181a at Attomolar Level in Complex Media Using a Nanophotonic Biosensor. *ACS Sens* **2016**, *1*, doi:10.1021/acssensors.6b00162.

80. Massad-Ivanir, N.; Shtenberg, G.; Segal, E. Optical Detection of E. Coli Bacteria by Mesoporous Silicon Biosensors. *J Vis Exp* **2013**, 6–13, doi:10.3791/50805.

81. Chen, Y.; Liu, J.; Yang, Z.; Wilkinson, J.S.; Zhou, X. Optical Biosensors Based on Refractometric Sensing Schemes: A Review. *Biosens Bioelectron* **2019**, *144*, 111693, doi:10.1016/j.bios.2019.111693.

82. Bartlett, J.G. Laboratory Diagnosis of Urinary Tract Infections in Adult Patients. *Infectious Diseases in Clinical Practice* **2004**, *12*, 360–361, doi:10.1097/01.idc.0000144910.19687.1f.

83. Lazcka, O.; Campo, F.J. del; Muñoz, F.X. Pathogen Detection: A Perspective of Traditional Methods and Biosensors. *Biosens Bioelectron* **2007**, *22*, 1205–1217, doi:10.1016/j.bios.2006.06.036.

Annex
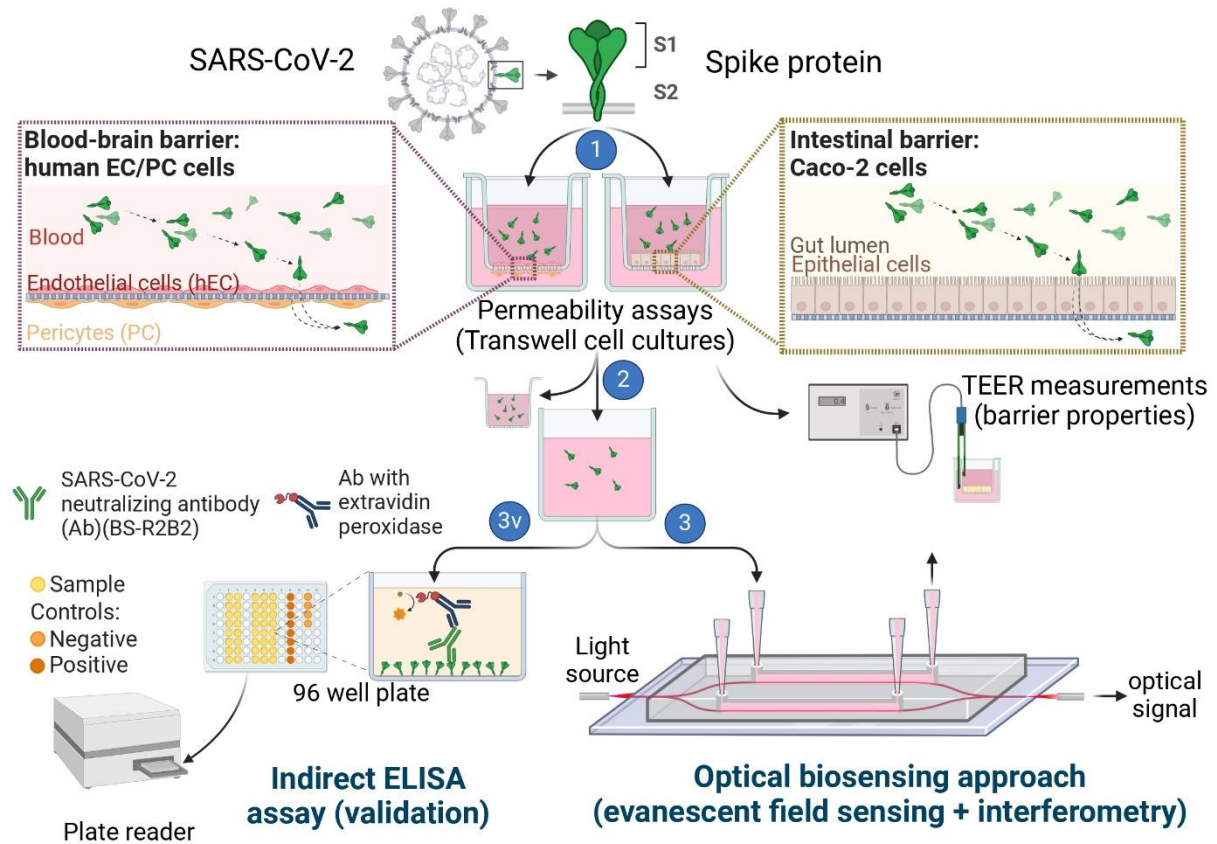
Figure A1. Workflow of the verification whether the SARS-CoV-2 surface S1 spike protein subunit could penetrate across human tissue barrier models, directly exposed to the protein: fluid sample of the S1 spike protein subunit (200 µg/ml in 0.1% BSA (bovine serum albumin) Ringer-HEPES buffer) was injected **(1)** into *in vitro* cell-culture model of the BBB (co-culture of human endothelial cells and pericytes) and the intestinal barrier (Caco-2 cells: human intestinal epithelial cells). Then, the barrier properties were followed by trans-endothelial/epithelial electrical resistance (TEER) measurements and permeability assays were performed **(2)**. To evaluate the amount of spike protein that crossed biological barrier models, an optical biosensing approach was applied **(3)**. The specific detection of the S1 protein was performed by the integrated optical Mach-Zehnder interferometer. An indirect enzyme-linked immunosorbent assay (ELISA) was used as an alternative detection technique of the target protein validating the results of the optical biosensing technique **(3v)**. The figure was created with BioRender.com.
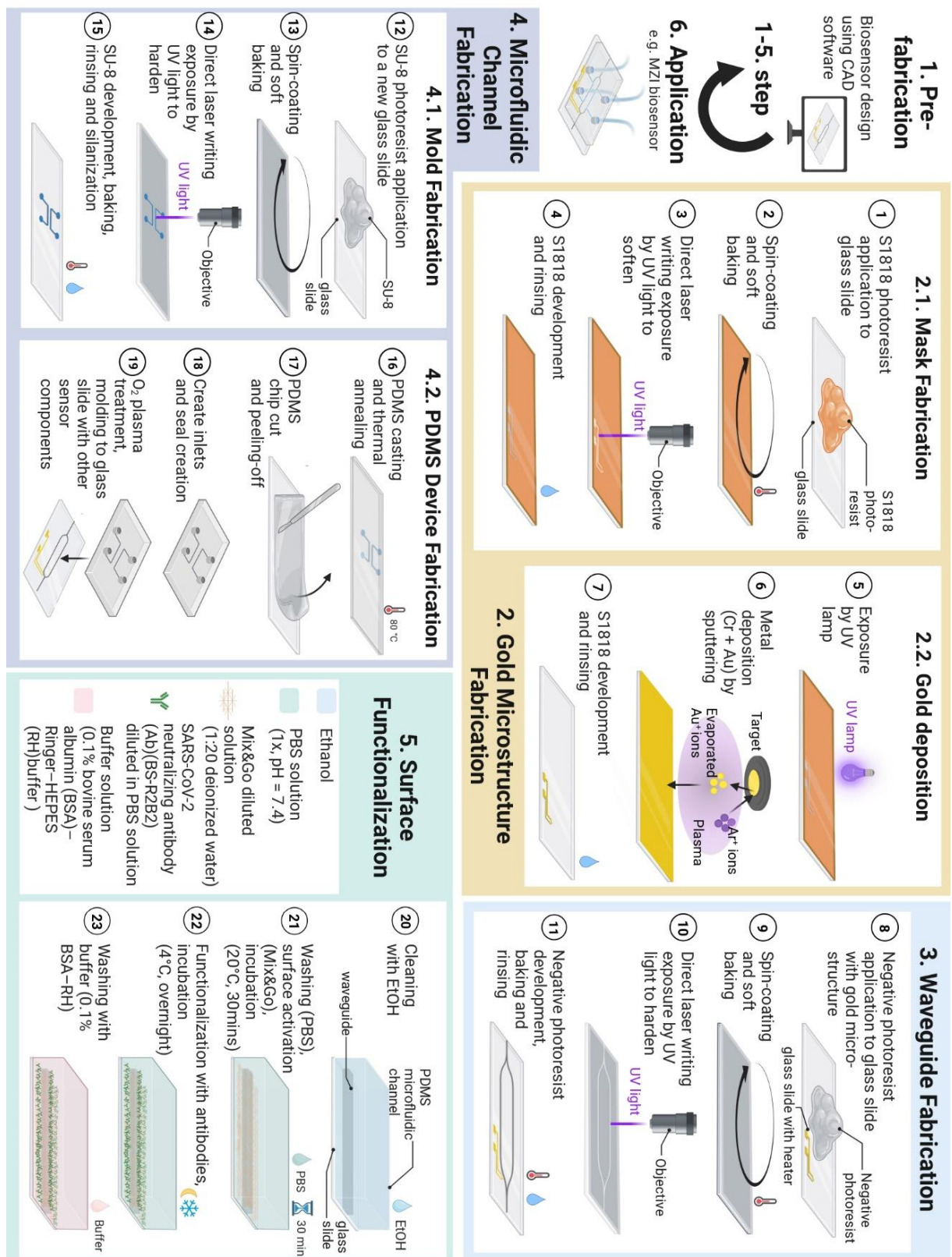
Figure A2. The detailed fabrication process of the biosensors, presented in case of the IO Mach-Zehnder interferometer device, where step 5 was also performed. Adapted from 'PDMS Microfluidic Chip Fabrication', by BioRender.com (2023). Retrieved from https://app.biorender.com/biorender-templates.

Validating the results by ELISA experiments

In addition to the application of the IO MZI biosensor, a conventional ELISA was also performed, by our colleagues from the Blood Brain Barrier Research Group, to detect the S1 subunit of the spike protein that crosses the BBB and the intestinal barrier. The results obtained by both methods could also provide a reliable and validated finding for the quantitative description of the phenomenon. In the process, TEER was measured in cell cultures following spike protein permeability assays. In this regard, treatment with 200 μg/ml spike protein did not change the TEER of the cultures compared to the negative control group assays receiving only the buffer (Figure A3a) [49].

Subsequently, both biosensor and ELISA measurements were performed with fluid samples from the lower compartment of the used inserts. The findings of ELISA proved that the S1 protein efficiently crossed the positive control, cell-free inserts. While this protein was detected reliably to pass through the cell monolayer in the BBB model, it was below the detection limit in the case of the intestinal barrier system (Figure A3b). The S1 subunit concentration results detected by ELISA for BBB model were almost identical to the biosensor measurements, by which the validation was achieved. In contrast, the amount of spike protein, passing through the intestinal epithelial cell monolayer Caco-2, was only detected by MZI measurements. Presumably, this observation is due to the difference in sensitivity between the two methods, i.e., ELISA had a higher limit of detection than the biosensor. Similarly, this difference in sensitivity was also observed for the upper limit of detection. In this case, such a measurement was performed where the spike protein passed through cell-free cell culture inserts [49].
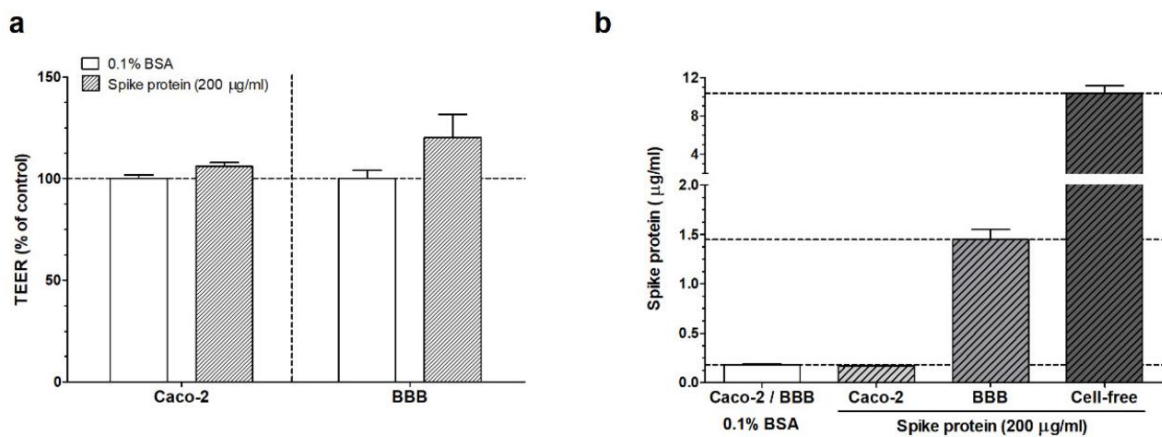

Figure A3. (a) Barrier integrity verification results after SARS-CoV-2 spike protein (200 μg/ml) treatment in 0.1% bovine serum albumin (BSA)–Ringer–HEPES buffer or only after buffer treatment (0.1% BSA), proved by trans-endothelial/epithelial electrical resistance (TEER) measurements. **(b)** Detection of S1 subunit by ELISA in samples from the bottom compartment of cell culture inserts after spike protein treatment (200 μg/ml, 30 min). Results were also obtained for permeability assay controls: positive control inserts, receiving only the carrier buffer (0.1% BSA) or negative controls, where there were no cell-cultures in the inserts ('cell-free inserts').

I.

Petrovszki D, Valkai S, Gora E, Tanner M, Bányai A, Fürjes P, & Dér A. An integrated electro-optical biosensor system for rapid, low-cost detection of bacteria. Microelectronic Engineering. 2021; 239,111523. IF: 2.662
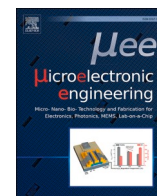
Research paper

An integrated electro-optical biosensor system for rapid, low-cost detection of bacteria

Dániel Petrovszki [a,b,*], Sándor Valkai [a], Evelin Gora [a], Martin Tanner [a], Anita Bányai [c], Péter Fürjes [c], András Dér [a]

[a] *Institute of Biophysics, Biological Research Centre, Szeged, Hungary*
[b] *Doctoral School of Multidisciplinary Medical Sciences, University of Szeged, Hungary*
[c] *Institute of Technical Physics and Materials Science, Centre for Energy Research, Budapest, Hungary*

ARTICLE INFO

ABSTRACT

In medical treatment, the detection of pathogens at an early stage of diseases is a key step to set up an appropriate diagnosis. To reach this goal, several techniques have been elaborated for point-of-care diagnostic applications. One of the state-of-the art methods is the application of biosensor devices. Label-free versions of them ensure an appropriate detection of pathogens from fluid samples by their relative sensitivity, rapidity and portability, thus offering a feasible and affordable alternative to the traditional diagnostic techniques. The aim of the present study is to fulfill these requirements with a cheap construction of an electro-optical biosensor, for application as a rapid test in clinical diagnostics. Hence, an integrated microsystem consisting of dielectrophoretic surface-electrodes, a rib waveguide and a microfluidic channel was created for label-free optical detection of bacteria from fluid samples. To model the efficiency of the sensor, we carried out quantitative measurements by observing the light scattered by living *Escherichia coli* cells located in the vicinity of the waveguide. A significant change in the scattered light pattern was observed even when objectives of moderate magnification (x10, x4.7) were used, implying that such type of sensing of the cells can be achieved by low-cost cameras, as well. The optimal frequency utilized in the process of dielectrophoretic cell-collecting was also established. With this novel system, a detection limit of ca. $10^2 CFU \times mL^{-1}$ was achieved, which is relevant to characteristic pathogen concentrations in body fluids, e.g., urine. Our further plan is to utilize this cell-gathering method in other, highly sensitive integrated optical sensor constructions, as well. The working principle of this dielectrophoretically enhanced detection of *Escherichia coli* cells from their suspensions gives us a low-cost and rapid-sensing alternative to routinely used, but time- and money-consuming other methods. Hence, we expect it to be readily applicable in point-of-care diagnostics as a basis of rapid tests to identify general pathogens from various body fluids.

1. Introduction

In different fields of everyday life, e.g. in medical treatment, food quality control, or biodefense, there is a strong need to detect or monitor pathogens as early as possible. Fortunately, several detecting and descriptive techniques are known for these purposes [1]. The conventional ones, including immunoassays and microbiology culture techniques – enzyme-linked immunosorbent assay (ELISA) or polymerase chain reaction (PCR) based systems – have been widely used. However, in regions with poor healthcare these methods are not feasible or affordable, because of their time-consuming processes – e.g., different steps of sample preparation and detection –, the high costs of reagents, or the necessity of high-tech diagnostic devices and laboratory experts. In these cases, cost-effectiveness, portability, small amount of required sample and rapid, properly sensitive and specific operation are also critical factors to ensure appropriate pathogen detection [2]. To fulfill these requirements, widespread applications have been investigated in the last two decades for point-of-care diagnostic purposes. The most popular methods apply biosensor systems with microfluidic channels. These devices can detect analytes of low concentrations from small sample volumes, thus they are widely used in the field of molecular biology, infectious disease management [3], food safety [4] and

biodefense [5]. One of their advantages compared to the conventional methods means that they can collect pathogens at the same place where the identification and measurements are carried out. Thus, it makes the detecting method easier, and reduces the time required for diagnosis, which helps finding the appropriate treatment in medical practice [6].

In these systems, various principles can be used for detection. Besides the systems using direct visualization of pathogens under the microscope, chemical-biological interactions can be used for quantification and identification by other detectors. Depending on the physical property of the captured signal, we can talk about electrical, electrochemical, optical or magnetic devices. Note that there are some cases where signal amplification is required, e.g. for optical detection purposes optical reporters, e.g. fluorophore dyes [7], metallic nanoparticles, or quantum dots [8] can be used. Moreover, another aspect of their differentiation is whether labeling is required in the detection process. While label-using techniques are usually more accurate, their cost is higher at the same time. Hence, nowadays label-free applications are also commonly used in point-of-care diagnostics.

One type of the generally used biosensors of label-free detection is based on impedance measurements. Due to their simplicity and adaptability, a lot of applications for pathogen detection can be found [9]. For reasons of portability and simplicity, these devices normally contain interdigitated microelectrode arrays to reach proper sensitivity, while keeping the size of the electrode-system reduced. To improve the sensing capability in these systems, dielectrophoresis (DEP) has been also utilized [10,11], in order to ensure appropriate analyte detection. Several studies show that this phenomenon is applicable for bacterial cell-separation or cell-concentration [12], as well as isolating bacterial cells from fluid samples [13].

Optical biosensors are used in other promising label-free sensing approaches, which are known for safety, rapidity and multipurpose capability combined with high sensitivity [14]. These devices take advantage of the different features of light to facilitate extremely sensitive detecting. In recent years, integrated optical applications have been extensively studied, where an optical waveguide is the key element in the detection process. Several studies [15,16] have shown that these sensor systems can be used for the recognition of pathogens. Although, their detection methods are very diverse, they are found very sensitive, in general. In the literature, evanescent-field sensing is the basic working principle of many widely used techniques that proved to be very good in high-sensitivity, specific detection purposes [16]. Here it is necessary to mention optical waveguide light-mode spectroscopy (OWLS) [17,18] and interferometric methods – e.g. Mach-Zehnder interferometer (MZI)-based [19,20] and surface plasmon resonance (SPR) techniques [21] – that can detect bacteria or other pathogens from fluid samples. Common to these devices is that they utilize specific adsorption onto a waveguide surface and convert the accompanying phase shift of the guided light to intensity changes measured by photodetectors. Horváth et al. demonstrated the applicability of an OWLS device by reaching a 60 cells x mm^{-2} detection limit for *Escherichia coli K12* bacteria from fluid sample [17]. This technology based on optical grating has also been applied for label-free sensing of other pathogen microorganisms, as well. Another study [18] presented an OWLS device which was used for the detection of *Legionella pneumophila* in water, where the biorecognition elements were antibodies. Besides the grating technology, interferometric detection is also among the promising label-free optical biosensing applications. Mathesz et al. presented an integrated optical interferometric biosensor, which device could detect *Escherichia coli* bacteria from fluid samples with a detection limit of $10^6 CFU \times mL^{-1}$ within a few minutes [19]. Moreover, another interferometric MZI immunosensor device showed a promising performance for the detection of *Listeria monocytogenes*, which pathogen can be lethal for humans. High specificity over other pathogen microorganisms was reached by this device. The biosensor achieved a limit of detection (LOD) of $10^5 CFU \times mL^{-1}$, which is below the infection dose [22]. In a recent review [21], emerging applications of SPR biosensors using modified detecting techniques have

been overviewed. One of them, namely, applied the SPR method to detect *E. coli O157:H7* pathogenic bacteria, using T4 bacteriophages as recognition elements, while another highly specific phage was used to detect *Staphylococcus aureus* (MRSA), as well. This system could achieve label-free, specific, rapid (less than 20-min) detection of pathogens, for concentrations of $10^5 CFU \times mL^{-1}$. In another example, an alternative version of SPR was used, where the sensing process was combined with imaging. A case study [23] showed that a charge-coupled device along with image processing methods is applicable for detection. Hence, this technique was found suitable for studying and monitoring molecular interactions in real-time, as well. In another approach, imaging-based sensing of scattered light was used in several studies – containing charge-coupled device readout systems – in order to identify and detect pathogens from fluid samples [24]. Related to this scattered light intensity detecting method, a commercially available optical sensor system, namely the MIT 1000 (Micro Identification Technologies Ltd., San Clemente, California, USA) also uses scattered light for the detection of pathogen bacteria from fluid samples. It analyses the back-scattering pattern of incident laser light both from the outer surface and from the internal part of bacteria. This manufacturer claims that 10–50 *CFU* $\times assay^{-1}$ can be detected by the device.

There are many different biosensor constructions available today, and the ones applying label-free methods are especially suited for rapid tests in medical diagnostics, hence they are in the forefront of related research. Table 1. shows a comprehensive review of the performance of the evanescent-wave based, label-free biosensing techniques, indicating the sensing method, the limit of detection (LOD) and the target pathogen microorganism.

In this paper we present a biosensing system, which can detect bacterial cells from low-volume fluid samples. This detection method combines a dielectrophoretic cell-collecting technique with evanescent-field sensing. After a detailed description of the device, we demonstrate the working principle of the system via a dielectrophoretically enhanced detection of *Escherichia coli* Dh5α cells from their suspensions, as a low-cost and rapid alternative of other, relatively sensitive methods.

2. Materials and methods

2.1. The working principle of the biosensor

2.1.1. Dielectrophoretic cell-collecting

Considering higher sensitivity, it is a crucial requirement in our sensor construction to collect the analyte particles adjacent to the sensor surface, to make them detectable by the device. To fulfill this need, we applied the phenomenon of dielectrophoresis (DEP), which is based on the dielectric polarization of particles (i.e., cells in our case). In microfluidic systems containing dielectric particles a dielectrophoretic force (DEP-force) awakes by applying inhomogeneous alternating electric field, that attracts (or repels) the analytes towards the electric field maxima or minima. If the force directs to the maximum field strength, we speak about positive dielectrophoresis, while the opposite effect is called negative dielectrophoresis [26]. The equation of DEP-force (Eq.1.) including the relative permittivity of the target particles compared to the surrounding medium and the frequency of the applied electric field can be described for spherical particles, as follows:

$$F_{DEP} = 2\pi r^3 \varepsilon_m Re\left[\frac{\left(\varepsilon_p^* - \varepsilon_m^*\right)}{\varepsilon_p^* + 2\varepsilon_m^*}\right] \nabla E_{rms}^2 \tag{1}$$

where *r* is the radius of the sphere, ε_p^*, ε_m^* are the complex permittivity for the particles and for the medium respectively, $\frac{\varepsilon_p^* - \varepsilon_m^*}{\varepsilon_p^* + 2\varepsilon_m^*}$ is the Clausius-Mossotti factor, which is a parameter of the relative polarizability of the particle, and E_{rms} is the root-mean-square of the applied alternate electric field [27].

Table 1
Recent results of various integrated optical biosensor constructions for pathogen detection.

Commercially used	Microfluidics	Type of sensor	Detection limit	Target	Sample type	Reference
Yes	No	Light scattering	$10 - 50$ $CFU \times assay^{-1}$	E. coli, Cryptosporidium, Giardia	cells from colony	http://www.micro-imaging.com
No	Yes	OWLS	$60 \, cells \times mm^{-2}$	E. coli	buffer	[17]
No	Yes	OWLS	1.3×10^4 $CFU \times mL^{-1}$	L. pneumophila	water	[18]
No	Yes	MZI	$10^6 CFU \times mL^{-1}$	E. coli	buffer	[19]
No	Yes	MZI	$10^5 CFU \times mL^{-1}$	L. monocytogenes	buffer	[22]
No	Yes	SPR	$10^3 CFU \times mL^{-1}$	MRSA, E. coli O157:H7	buffer	[25]

By adequate definition of characteristic parameters of the applied alternating electric field, the mentioned specific cell-collecting or cell-separating microfluidic devices can be designed [12]. A promising approach is to apply this cell-collecting method in biosensing systems developed for medical diagnostics.

2.1.2. Evanescent-field sensing via light scattering

One type of the integrated optical biosensors is based on evanescent-field sensing. In this case the light propagates in a miniature waveguide structure by total internal reflection and the output light intensity is influenced by any change in the environment. It can be caused by e.g. the bonding of the particles on the surface [28]. In such integrated optical systems, the propagating waves penetrate the surrounding media to a limited extent ("evanescent-field"), allowing the detection of target molecules adjacent to the waveguides (Fig. 1a)).

There are various options to carry out quantitative measurements using this method. One of them is to measure the light that the target particles – bound to the surface of the waveguide structure – scatter, while other approaches use e.g. interferometric detection [14]. Regarding the practical applications, a crucial feature of all integrated optical biosensors is their sensitivity. In case of detecting bacteria or other cells from body fluids, increasing the cell concentration on the detector surface is a crucial requirement, where the above mentioned dielectrophoretic cell-concentrating technique can play an important role.

2.2. Device fabrication

2.2.1. Combined thin-film gold electrode and integrated optical system

In the architecture of the biosensing device, the dielectrophoretic cell-collector electrode system was prepared by fabricating gold surface-electrode pairs with tilted fingers optimized for positive dielectrophoresis. The structure of this system is inspired by the design of a previous study [29], where electrode-pairs were used for cell-focusing in a microfluidic channel. Nevertheless, for the integrated sensing optical structure, a rib waveguide stripe was made within the gap of the

electrodes, as it can be seen in Fig. 1b). Hence, the cells captured in the evanescent region of the waveguide can be detected by a photodetector, since they become elementary sources of scattered light in that region. For manufacturing both the appropriate electrode system and waveguide structure, direct laser writing technique (µPG-101 machine, $\lambda = 405nm$, Heidelberg Instruments GmbH., Heidelberg, Germany) was used.

As the first step of the device fabrication, the electrodes were structured utilizing lift-off lithography technique following the protocol of the manufacturer of the applied materials. A positive S1818 photo-polymer (MicroResist Technology GmbH., Berlin, Germany) layer was spincoated (3000 rpm, 60 s) in the thickness of 2 µm on a microscope coverslip (Menzel-Gläser, Thermo Fisher Scientific, Waltham, Massachusetts, USA), which step was followed by soft baking (115 °C, 1 min). Then the photopolymer was exposed by the direct-laser writing apparatus, forming the desired structure of the tilted electrode-pairs. Afterwards, the coverslip was rinsed (90 s) in the developer solution of the photopolymer (MICROPOSIT MF-319 solution, Kayaku Advanced Materials, Inc. (formerly MicroChem Corp.), Westborough, Massachusetts, USA) and was washed by deionized (18.2 MΩ) MilliQ water (Synergy® UV Water Purification System, Merck-Millipore, Burlington, Massachusetts, USA) to remove the exposed part of the polymer. As a result, a mask was made containing the design of the electrodes. Next, the coverslip was exposed again by Mercury i-line UV light (Oriel 97,435 UV lamp, $\lambda \approx 365nm$, Newport Corp., Irvine, California, USA), in order to remove the remained part of the photopolymer from the surface by a repeatedly applied developing step. After the exposure, homogeneous chromium and gold layers were deposited by sputtering technique. During this process, the chamber was pumped to high vacuum (8×10^{-2} mbar), and Argon gas was used to generate sputtering ions during the process. At first a 10 nm thick Cr layer was deposited in order to enhance the gold layer adhesion to the glass surface. Then a 30 nm thick Au layer was deposited. Next, the mentioned developing step was performed. In this step, the coverslip was rinsed in the solution for a two-day long period to remove all the photopolymer from its surface. After that, the coverslip was dried and then was used as a substrate for the further
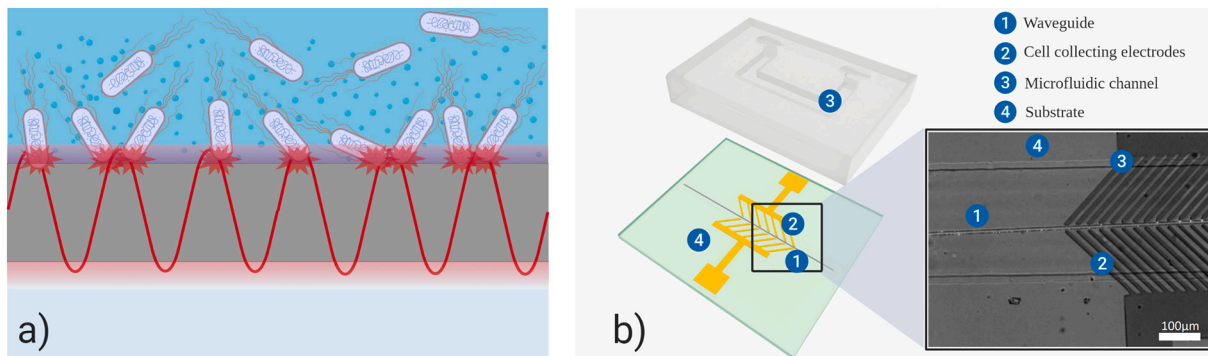

Fig. 1. a) shows the schematic illustration of the evanescent-field sensing, where the bonding of the Escherichia coli bacteria to the surface of the waveguide cause scattering of the evanescent waves of the light propagating in the waveguide. Fig. 1b) illustrates the schematic design and realization of the integrated optical biosensor system (the figure was created with Biorender.com).

steps.

Next, the integrated optical waveguide structure was fabricated. During this process the deposited substrate – containing the electrode system – was covered by a 2-μm thick negative photopolymer (Epo-Core_2, MicroResist Technology GmbH., Berlin, Germany) by spincoating (3000 rpm, 60 s). Then it was prebaked in two steps (first at 50 °C for 2 mins, then with even heating at 90 °C for 2 mins). After the coverslip was cooled down to room temperature (approx. After 30 mins), the photopolymer was exposed by direct laser writing for the rib waveguide strip localized in the 10 μm gap between the tilted electrode pairs. Afterwards, the coverslip was postbaked in two steps (first at 50 °C for 2 mins, then with even heating at 85 °C 3 mins). As in the case of pre-baking, after the substrate was cooled down to room temperature, it was rinsed (90 s) in the developer of the photopolymer (mr-Dev 600 developer solution, MicroResist Technology GmbH., Berlin, Germany) and was washed by isopropanol. After these steps of the fabrication, a combined biosensing system consisting of sensing integrated optical waveguide strip and cell-collecting electrode system was realized (Fig. 1b.)). These are the two key components of the integrated optical sensor device.

2.2.2. Microfluidic channel

In our construction, the purpose is to detect bacteria from small sample volumes. Therefore, a microfluidic channel was required to ensure the continuous flow of these fluids. During the preparation process of this PDMS (poly(dimethylsiloxane)) channel, soft lithography technique was applied following the steps described in the previous work of our research group [19]. First a mold was fabricated by using a SU-8 negative photoresist. As a first step of the fabrication, a 15-μm thick photoresist layer was spincoated on a glass substrate, and then softbaked (90 °C, 5 min). Afterwards, it was exposed through a photomask by UV light (Oriel 97,435 UV lamp, $\lambda \approx 365nm$, Newport, Corp., Irvine, California, USA). Next, a liquid PDMS prepolymer (degassed 1:10 mixture of Sylgard 184, Dow Corning, Midland, Michigan, USA) was poured over the master mold and cured for 30 min at 80 °C. Subsequently, the replica of the PDMS was peeled from the master structure and adequate holes were pierced at inlets and outlets for pipette tips. To finish the process, the PDMS was bonded above the tilted fingers region of the electrode-pairs, including the sensing rib waveguide structure in the gap between them (Fig. 1.b)).

2.3. E. coli suspension preparation

In this study, only non-virulent, living *E. coli* cell cultures of Dh5α strain were used. Prior to use, the colonies were kept on agar plates at 4 °C. For the experiments, the cells were pipetted into 3 mL LB (lysogeny broth) medium in a sterile polystyrene tube. Then the bacteria were grown overnight in a shaker incubator at 30 °C. Next morning, these cultures were diluted back 100 times. Then cells were grown until they reached the optical density of 0.4 at 600 nm (OD_{600}). In the meantime, an Eppendorf-tube was filled with 1350 μL sterile-filtrated (0.2 μm pore size cellulose acetate sterile syringe filter, VWR International, Radnor, Pennsylvania, USA) master dilution solution of LB and MilliQ deionized water (1:9 ratio). Next, 150 μL of the cell culture was pipetted into this tube and was resuspended. Note, that samples spiked by dielectric particles, e.g. LB solution, must be diluted to lower ionic strengths for the optimal working of the applied DEP collecting electrode system, the dielectric particles filled samples and to avoid undesired side-effects, i. e., electrolysis of the fluid and the damages to electrodes. Prior to the experiments, the desired concentration of *E. coli* suspensions was adjusted. The concentration of the undiluted bacteria in the LB culture was determined by plate counting technique and expressed in colony forming units per milliliter ($CFU \times mL^{-1}$).

During the experiments aiming at the size selectivity of the applied cell-collecting method, a mixture of living *E. coli* and hCMEC/D3 (Human Cerebral Microvascular Endothelial Cell Line) cell cultures was diluted by the master dilution mixture, following the same protocol that used for *E. coli* suspension dilution, but in this case negative artificial urine (pH = 5.94) was used to replace the LB in the solution (artificial urine and deionized water in the ratio of 1:9 respectively). The hCMEC/D3 (Human Cerebral Microvascular Endothelial Cell Line) cells were grown in an incubator and were diluted back prior to the mixing step. The urine solution was prepared on the basis of the protocol of negative artificial urine base solution recipe ("Case A" in the study of Khan et al. [30]), with the following modifications. Firstly, the base solutions were made by diluting 1.3609 g KH_2PO_4 (0.1 M) and 2.2823 g K_2HPO_4 (0.1 M) in 100 mL-100 mL deionized water. Then, the applied urine solution was prepared by mixing the two solutions in 2:1 ratio respectively. Finally, 7.5 mg Tween-20 (Sigma-Aldrich, St. Louis, Missouri, USA) was added to the 150 mL of the final negative artificial urine solution (pH = 5.94) to avoid aggregation.

2.4. Experimental setup

In this study, the fluid sample was pumped into the microfluidic channel at a constant flow rate by a syringe pump (SP210IWZ syringe pump, World Precision Instruments Inc., Sarasota, Florida, USA). The system was monitored by a CCD camera attached to an inverted microscope (Zeiss Axiovert 200, Jena, Germany) and connected to a computer, that was also used to capture optical images during scattered-light detecting experiments. AC electric field at various frequencies was applied for generating positive DEP, for optimizing the collecting capability of the electrode system coupled to a function generator (20 MHz function generator model 8020, Tabor Electronics Ltd., Nesher, Israel) with sinusoidal signals. Switching on and off the voltage was controlled via square wave trigger signals (TTL, 1.4 s) from a timer (Uniblitz VS14S2ZM1R1–21, Vincent Associates, Rochester, New York, USA). The light beam of a laser diode ($\lambda = 670nm$) was used for measuring and was coupled to a single-mode optical fiber (S630-HP, Thorlabs), whose other end was matched to the input of the waveguide by a micropositioner (DC-3 K, Märzhäuser Wetzlar GmbH & Co. KG, Wetzlar, Germany), and its optimal position was fixed by a photopolymer glue (OP-66-LS, Dymax Europe GmbH, Wiesbaden, Germany). Fig. 2 shows the experimental setup of the realized biosensor system.

3. Results and discussion

3.1. Dielectrophoretic cell-collecting

Regarding the sensitivity of the detection method, testing the cell-collecting capability of the thin-film electrode system was crucial. (Note, that these experiments were performed prior to the detecting experiments, and the device did not contain the detecting waveguide structure.) As a first step, we tested the particle-collecting capability and the size-wise selectivity of this method by injecting a mixture of deionized MilliQ water (Synergy® UV Water Purification System, Merck-Millipore, Burlington, Massachusetts, USA) and polystyrene beads (Polybead® Microspheres, Polysciences Inc., Warrington, Pennsylvania, USA) of different diameters (1 μm, 9 μm) into the microfluidic channel. During these experiments, the fluid sample was pumped at the flow rate of 5 μL × min^{-1}, while alternating electric field current (30 V_{p-p}, 5 MHz) was applied to achieve the desired positive dielectrophoretic collection of the target particles. The results met our expectations. Applying this method, we could attract the polystyrene beads of the desired 1 μm diameter to the surface of the gap between the electrodes, whilst it did not cause any change in the movement of the beads of 9 μm diameter in the mixture.

Based on these measurements, the next step was to replace the polystyrene bead target particles with non-virulent, living *Escherichia coli* cells, to collect pathogens from their diluted samples utilizing this phenomenon. In this case, we used bacterial suspensions of various dilutions, in order to determine the sensitivity of our system. The protocol
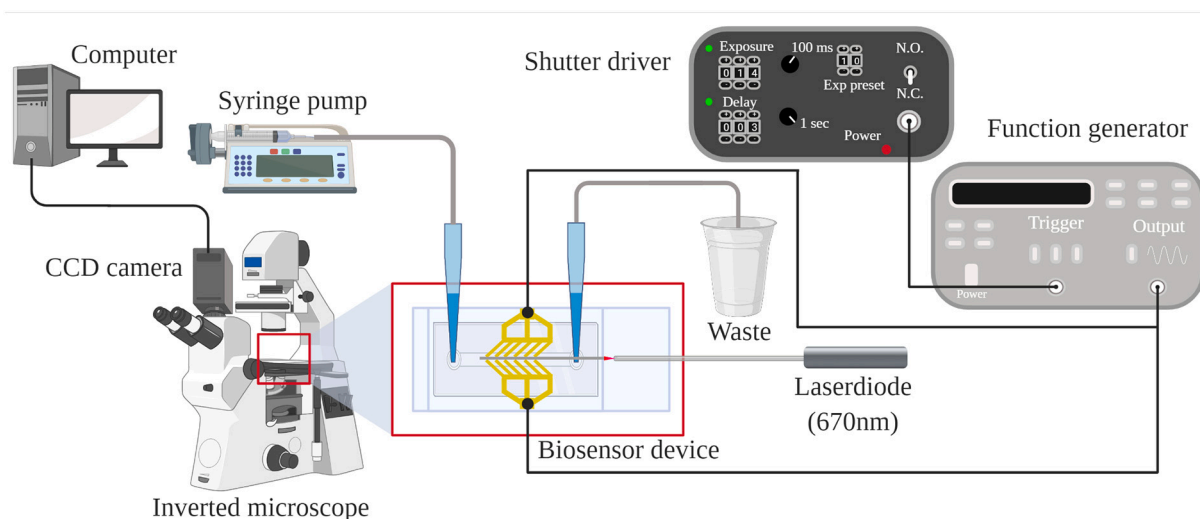
Fig. 2. Schematic illustration of the experimental setup. The sample was pumped through the microfluidic channel by a syringe pump, the red light of a laser diode was coupled to the waveguide by a single mode optic fiber, and the electrodes were connected to the signal generator controlled by a shutter-driver timer. Image capturing was carried out by the CCD camera of an inverted microscope connected to the computer, where image processing was performed. (The figure was created with BioRender.com).

of the experiment was the same as the one used in case of the polystyrene beads. During each cell-collecting process, the *E. coli* bacteria suspension was pumped at a flow rate of $5\ \mu L \times \min^{-1}$ for a half-an-hour-long period after the application of alternating electric field. First, we examined the applicability of the mentioned surface-electrode system in case of a bacterium suspension of $10^6 CFU \times mL^{-1}$ concentration. In this case effective cell-collecting could be observed shortly after the experiment started (Supplementary Experimental Data – Videos: VideoS1-Cell-collecting). Following the experiments with further diluted *E. coli* samples, we observed that a high ratio of the analyte cells was collected from the diluted suspension of bacteria of a concentration of $10^4 CFU \times mL^{-1}$ as well. Hence, this lower-concentration sample seemed applicable for our detecting purposes, to perform quantitative measurements for optimizing the crucial parameters of the detecting system, namely, to choose optimal magnification and AC frequency.

3.2. Detection via evanescent-wave scattering: Image capturing and analysis

3.2.1. Optimization of the experimental parameters

During the biosensing experiments, the measuring system included the detecting waveguide structure, too. After completing the he above-described dielectrophoretic cell-collecting process for 30-min, the alternating electric field was turned off ("OFF state") and then on ("ON state") again, by giving short, 1.4-s long pulses with three-second long pauses, hence, periodically changing the adhesion contact between the cells and the surface of the waveguide. The subsequent changes in the pattern of the scattered-light intensity image could be observed and captured, too. Based on microscopic observations, these changes correlated, and hence, were attributed to the movement of bacteria due to switching on and off the alternating electric field. (Note that during these experiments only bacterial cells were present in the suspension.) This procedure gave the basics of the quantitative detection. Note that the short duration of the pulse periods was crucial to avoid the removal
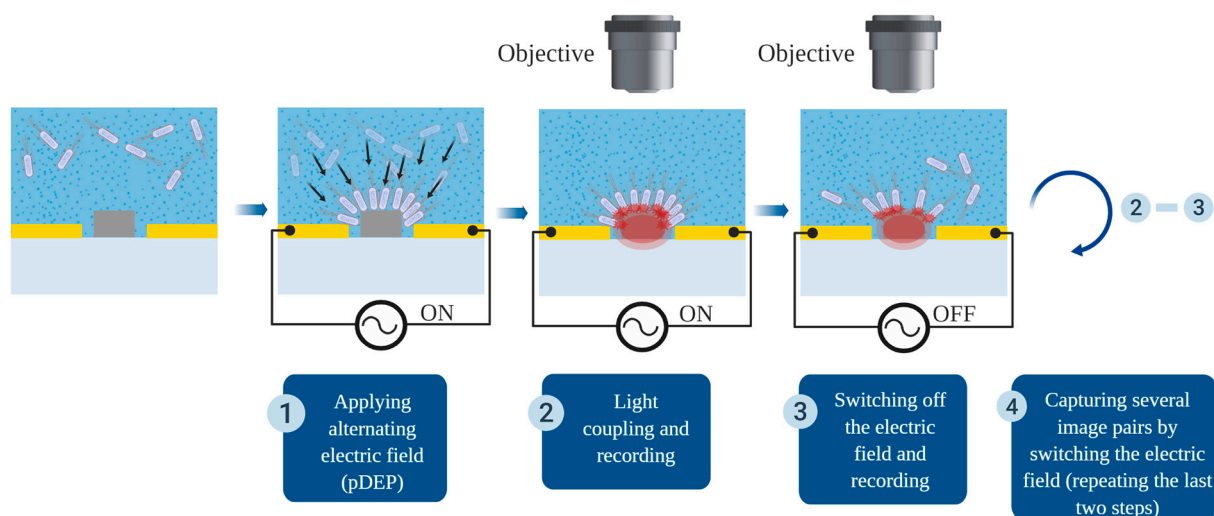

Fig. 3. The image-analysis assisted, quantitative measurement, which is based on the recorded scattered light intensity images, while the inhomogeneous alternating electric field is switched on and then off, inducing bacteria movement and change in the scattered image patterns. (The figure was created with BioRender.com.)

of collected bacteria from the sensing region. During this period of the measurement process, several image pairs were captured from the same cross-section of the system in different states (OFF and ON). The whole detection period lasted about 40 mins, including the cell-collecting step. The schematic illustration of *E. coli* cell detection based on the evanescent-wave scattering process is shown in Fig. 3. Further details of the measurements can be found in the Supplementary Experimental Data – Videos: VideoS2-Magnification-test.

During the follow-up tests, objectives of different magnifications (x4.7, x10, x20) were used for image capturing of the scattered light, in order to define the applicable resolution where the change in the scattered light intensity image is significant. For demonstration, light-intensity difference images were calculated for a diluted ($10^4 CFU \times mL^{-1}$) bacterium suspension, showing the change in the scattered light pattern (Fig. 4).

For making these measurements quantitative, image processing methods were applied, in order to determine the similarities and differences between the captured scattered light patterns. To achieve this goal, a script and a function was written in MATLAB2017b, in order to calculate appropriate variables to describe the similarities between the images. Hence, correlation and mean-squared error (MSE) values were calculated for every captured image pair, based on image processing functions of MATLAB, e.g. *corr2()* or *immse()*. To determine whether the scattered light pattern was changed significantly between the OFF and ON states of the system, the same calculations were performed also for different images recorded in the same state (OFF-state and ON-state images), which served as control groups. The results of the image analysis (number of image pairs: $n = 5$–12, Supplementary Experimental Data - Tables: TableS1-Optimization) clearly show that there was significant difference in the MSE values between the image pairs (OFF-ON images) compared to the fluctuations within control groups (Fig. 5a)-b). It could be established that significant differences for MSE values were observed in those cases, too, where the detection was carried out by objectives with less magnification (x4.7, x10) (Fig. 5a, and Supplementary Experimental Data – Tables: TableS1-Optimization).

Thereafter, a second set of experiments was carried out to optimize the collecting process in the DEP cell by determining the ideal frequency of the applied alternating electric field, where most bacteria cells can be collected (Supplementary Experimental Data – Videos: VideoS3-Frequency-test). For this purpose, the frequency range of 100 kHz to 5 MHz was applied, and, using the above protocol for quantitative image processing, it was established that the 5 MHz frequency yielded the best results for dielectrophoretic cell-collecting (Fig. 5b), and Supplementary Experimental Data – Tables: TableS1-Optimization), a process crucial from the point of view of sensitivity.

3.2.2. Determination of the sensitivity of the method

After optimizing the AC frequency and the optical magnification,

further experiments aiming to determine the detection limit of this sensing system were carried out. To this end, we used a serial dilution of samples of $10^2 - 10^6 CFU \times mL^{-1}$ concentration, to collect and detect bacteria cells from fluid samples, using the optimal measuring conditions (the objective of x20 magnification and the optimized AC parameters (30 Vp-p, 5 MHz, sinusoid signal)). Moreover, experiments revealing the kinetics of the dielectrophoretic cell-collection were also performed to reduce the time period required for determining the most significant scattered-light pattern changes. For this purpose, capturing of the scattered light intensity images was performed for each of the serial diluted bacteria suspensions, with a collecting period time of 0 ($n = 5$), 1 ($n = 10$), 3 ($n = 6$–10), 10 ($n = 19$–20) and 30 ($n = 20$) minutes (Supplementary Experimental Data – TableS2-Sensitivity). Note, that here the 0-time values correspond to reference measurements. In these cases, mean-squared-error image similarity values were calculated for each image pairs (OFF and ON state), and for each group images. Based on the image processing results, an optimal cell-collecting period time of 10 mins was estimated. Fig. 6a) shows the results ($n = 19$–20) of the scattered light intensity image processing for the serial diluted bacteria suspensions with 10-min long cell-collecting. (Further details are found in the Supplementary Experimental Data – Tables: TableS2-Sensitivity) The resulting data clearly shows that a significant difference can be found in the MSE values of the pairwise images compared to the group ones even for the lowest, $10^2 CFU \times mL^{-1}$ bacteria concentration. The tendency of this difference in the MSE values between the pairwise and group data for the bacteria samples is indicative of the collected number of bacteria, which can be used for the calibration of the sensor system. For this purpose, this difference was calculated utilizing the mean MSE values of the pairwise and group data. Since this experiment was performed on the same biosensor, a reference MSE difference value was calculated using the images from the first detection step of the process, where no bacteria cells were collected. Then this value was extracted from every MSE difference value, and the resulting differences between the MSE values of the pairwise images and the group ones are shown in Fig. 6b). A power-law function could be fitted to these values, with a multiplication factor of 0.6152, and an exponent of 0.2228. Taking into account the high goodness-of-fit value ($R^2 = 0.91$), this function can be considered to define the calibration curve for this experiment.

3.3. Experiments with artificial urine containing bacteria and somatic cells

As a pilot test focusing on the selectivity of the cell-collecting process, an artificial urine sample containing a mixture of *E. coli* and *hCMEC/D3* endothelial cell suspensions at the concentration of $10^4 CFU \times mL^{-1}$ was used to mimic an environment of inflammatory urine, infected by bacteria, and containing other cell types, too. During the experiment, an alternating electric field (30 V_{p-p} 5 MHz) was applied. At
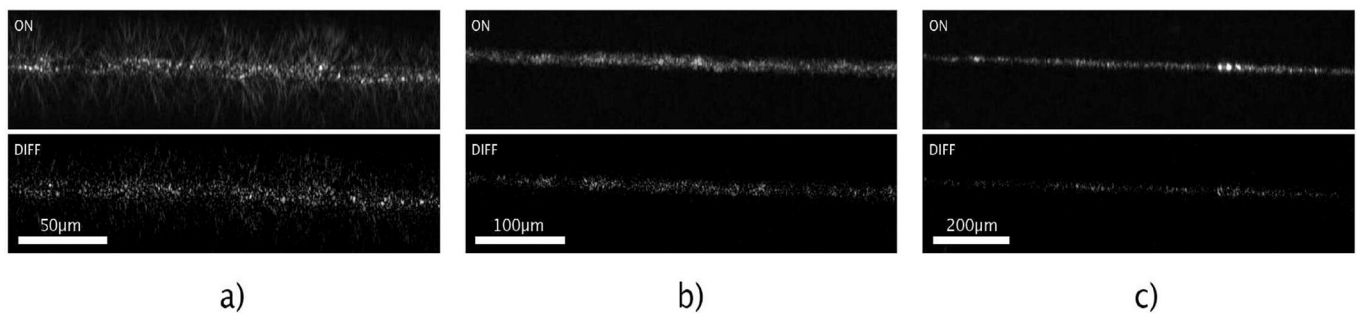

a)   b)   c)

Fig. 4. Scattered light intensity images at the same region of the biosensor system are shown after cell-collecting (10^4 CFU $\times$ mL^{-1} E. coli suspension) at given alternating electric field parameters detected by objectives of x20 (a), x10 (b), and x4.7 (c) magnifications. The upper inserts show the scattered-light intensity pattern when the electric field is applied to the electrodes (ON), the lower ones represent the scattered intensity difference between the ON and OFF states (DIFF). The images were evaluated by image processing.
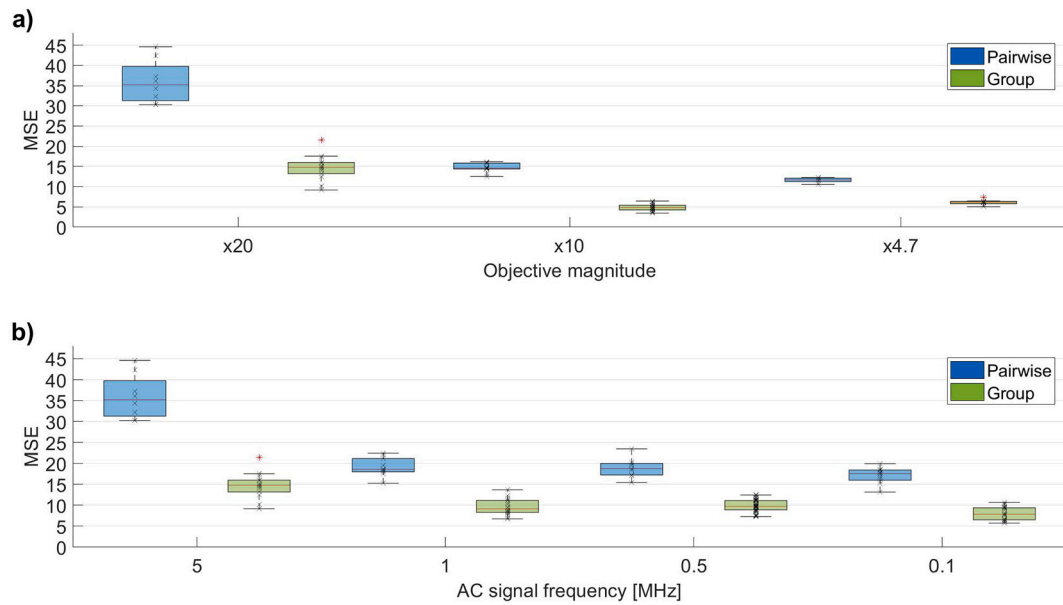
Fig. 5. Image analysis of pairwise and group results (n = 5–12) of experiments applying various objective magnifications (a)) and AC frequencies (b)) at a given E. coli concentration ($10^4 CFU \times mL^{-1}$). As a quantitative descriptor of the effects, the mean-squared errors (MSE) of the scattering patterns ("pairwise" and "group" images) were taken at the same region of the intensity images (x20 objective). The images were captured applying AC signal of 30 V_{p-p} amplitude and various frequencies in the range of 0.1–5 MHz. In the experiment aimed to optimize objective magnification, the applied electric field parameters were 30 V_{p-p} and 5 MHz.
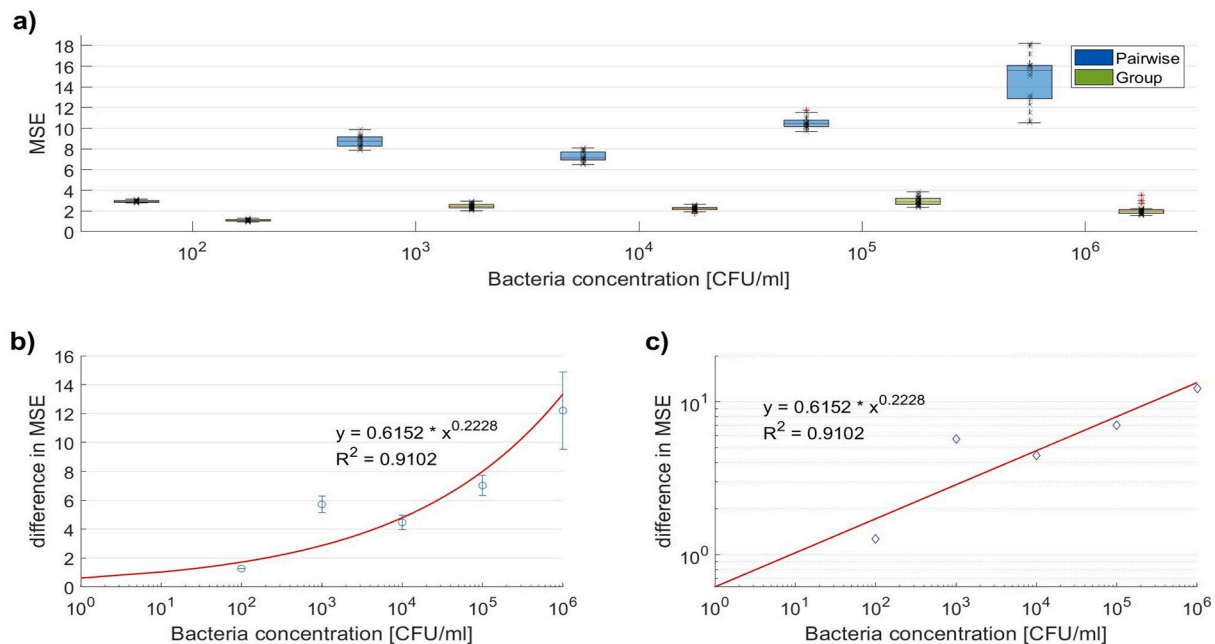
Fig. 6. Fig. 6.a) Image analysis results of pairwise and group images (n = 19–20) registered during the experiments with serial diluted bacteria suspension ($10^2 - 10^6$ CFU $\times$ mL^{-1}). As a quantitative descriptor of the image differences, mean-squared error (MSE) values between the scattering patterns were taken at the same region of the biosensor device (x20 objective). Fig. 6.b) shows the difference of the MSE values (mean±standard deviation) of the pairwise images compared to the control group ones. 6c) shows the same difference, but on a dual-logarithmic scale. 6b) and 6c) also shows that even at an extremely low bacteria concentration (10^2 CFU $\times$ mL^{-1}) a significant difference can be observed between the corresponding MSE values, defining the detection limit of this novel biosensing method. A power-law function could be fitted to the data ($R^2 = 0.91$), providing the calibration curve of the method, as well.

first, the fluid sample was pumped at a flow rate of 0.1 $\mu L \times$ min^{-1} for a couple of minutes, to observe the effect of the dielectrophoresis on the individual cells, while the sample was flowing through the channel. Due to the size-dependent behavior of the dielectrophoresis at the chosen frequency and ionic strength, collection of bacteria (~2 μm) and repelling of endothelial cells (~10 μm) was observed in the region of the electrode system, due to the size difference between the two cell types.

Next, a selective bacteria collecting was performed while the suspension was pumped at a higher, 3 $\mu L \times$ min^{-1} flow rate. During the process no endothelial cell was observed to be collected on the surface of the waveguide whereas many bacterial cells were adhered on the gap between the tilted-finger electrode pairs (Supplementary Experimental Data – Videos: VideoS4-Selectivity). The results of the pilot test proved a sort of selectivity of our method: bacteria were collected on the sensor

surface between the electrodes, while endothelial cells were flowing through the microchannel above the sensor system, not interfering with the detection of pathogens.

4. Conclusions

We presented an image-analysis assisted, label-free, rapid bacterium-detecting method, and we could demonstrate its working principle with a suspension of real, living *E. coli* bacterial cells. Applying this detection method and choosing the optimal statistical analyzing tools (e.g. determination of correlation, mean-squared error), a proper calibration of image similarities could be realized. The mean-squared error variable proved to be the most appropriate for this purpose. Using image processing methods, the optimization of the applied alternating current frequency was performed. Based on the image similarity results, we established that the biosensor construction can be used with a less sensitive detector (e.g., by a cheap camera). Note that, it was not necessary to observe individual cells utilizing this method, still, the change in the scattered light pattern seemed to be a good indicator of the presence of the analytes based on the results of the detection limit experiments. The sensitivity of the method was found to be ca. 10^2 CFU $\times$ mL^{-1}. The new technique outperforms a previous interferometric biosensor construction of our working group [19], and is relevant to characteristic pathogen concentrations in, e.g., urine [31]. Moreover, this sensitivity is comparable with other label-free optical – OWLS, MZI, SPR techniques – detection methods listed in the introduction [32,33]. The detection time of the sensor was optimized in 10 min and was found to be considerably less than the ones of traditional bacterium-detecting laboratory techniques, e.g. ELISA or PCR [34]. However, the present form of the measuring technique is restricted to monitor unspecific bonding of the analyte cells on the surface of the waveguide. Still, a pilot test with artificial urine, containing a mixture of bacterial *E. coli* cells and *hCMEC/D3* endothelial cells, proved that our sensing technique is selective for the detection of bacterial cells over somatic cells, due to the frequency- and cell-size dependent sign change of the collecting dielectrophoretic force. In forthcoming studies, we plan to functionalize the sensor surface to reach specific bacterium cell sensing and test the system under conditions where a mixture of different pathogens is present, such as in case of body fluids. However, we believe that even in its proof-of-concept form, this detection method is very promising from the point of view of its sensitivity, low cost of fabrication, and rapid detection process. Improving the image analyzing methods and optimizing the applied codes are expected to further reduce the detection limit of our technique. We hope that in the future this detecting technique can be utilized in point-of-care diagnostics.

Supplementary data to this article can be found online at https://doi.org/10.1016/j.mee.2021.111523.

Declaration of Competing Interest

The authors declare that they have no known competing financial interests or personal relationships that could have appeared to influence the work reported in this paper.

Acknowledgements

References

[1] B. Nasseri, N. Soleimani, N. Rabiee, A. Kalbasi, M. Karimi, M.R. Hamblin, Point-of-care microfluidic devices for pathogen detection, Biosens. Bioelectron. 117 (2018) 112–128, https://doi.org/10.1016/j.bios.2018.05.050.

[2] D.T. Chiu, A.J. deMello, D. Di Carlo, P.S. Doyle, C. Hansen, R.M. Maceiczyk, R.C. R. Wootton, Small but perfectly formed? Successes, challenges, and opportunities for microfluidics in the chemical and biological sciences, Chem 2 (2017) 201–223, https://doi.org/10.1016/j.chempr.2017.01.009.

[3] C.D. Chin, T. Laksanasopin, Y.K. Cheung, D. Steinmiller, V. Linder, H. Parsa, J. Wang, H. Moore, R. Rouse, G. Umviligihozo, E. Karita, L. Mwambarangwe, S. L. Braunstein, J. Van De Wijgert, R. Sahabo, J.E. Justman, H. El-Sadr, S.K. Sia, Microfluidics-based diagnostics of infectious diseases in the developing world, Nat. Med. 17 (2011) 1015–1019, https://doi.org/10.1038/nm.2408.

[4] C. Adley, Past, present and future of sensors in food production, Foods. 3 (2014) 491–510, https://doi.org/10.3390/foods3030491.

[5] P. Mehrotra, Biosensors and their applications - a review, J. Oral Biol. Craniofacial Res. 6 (2016) 153–159, https://doi.org/10.1016/j.jobcr.2015.12.002.

[6] Y. Wang, Y. Yu, X. Kong, L. Sun, Application of nanodiagnostics in point-of-care tests for infectious diseases, Int. J. Nanomedicine 12 (2017) 4789–4803, https://doi.org/10.2147/IJN.S137338.

[7] F. Gaits, K. Hahn, Shedding light on cell signaling: interpretation of FRET biosensors, Sci. STKE 2003 (2003) 1–6, https://doi.org/10.1126/stke.2003.165.pe3.

[8] G. Kim, J.H. Moon, C.Y. Moh, J. Guk Lim, A microfluidic nano-biosensor for the detection of pathogenic Salmonella, Biosens. Bioelectron. 67 (2015) 243–247, https://doi.org/10.1016/j.bios.2014.08.023.

[9] E.B. Bahadir, M.K. Sezgintürk, A review on impedimetric biosensors, Artif. Cells Nanomed. Biotechnol. 44 (2016) 248–262, https://doi.org/10.3109/21691401.2014.942456.

[10] C. Páez-Avilés, E. Juanola-Feliu, J. Punter-Villagrasa, B. Del Moral Zamora, A. Homs-Corbera, J. Colomer-Farrarons, P.L. Miribel-Català, J. Samitier, Combined dielectrophoresis and impedance systems for bacteria analysis in microfluidic on-chip platforms, Sensors (Switzerland) 16 (2016), https://doi.org/10.3390/s16091514.

[11] C.D. Chin, V. Linder, S.K. Sia, Lab-on-a-chip devices for global health: past studies and future opportunities, Lab Chip 7 (2007) 41–57, https://doi.org/10.1039/b611455e.

[12] B.H. Lapizco-Encinas, B.A. Simmons, E.B. Cummings, Y. Fintschenko, Dielectrophoretic concentration and separation of live and dead bacteria in an array of insulators, Anal. Chem. 76 (2004) 1571–1579, https://doi.org/10.1021/ac034804j.

[13] P.R.C. Gascoyne, J. Noshari, T.J. Anderson, F.F. Becker, Isolation of rare cells from cell mixtures by dielectrophoresis, Electrophoresis. 30 (2009) 1388–1398, https://doi.org/10.1002/elps.200800373.

[14] S.M. Yoo, S.Y. Lee, Optical biosensors for the detection of pathogenic microorganisms, Trends Biotechnol. 34 (2016) 7–25, https://doi.org/10.1016/j.tibtech.2015.09.012.

[15] P. Kozma, F. Kehl, E. Ehrentreich-förster, C. Stamm, F.F. Bier, Biosensors and bioelectronics integrated planar optical waveguide interferometer biosensors : a comparative review, Biosens. Bioelectron. 58 (2014) 287–307, https://doi.org/10.1016/j.bios.2014.02.049.

[16] B. Chocarro-Ruiz, A. Fernández-Gavela, S. Herranz, L.M. Lechuga, Nanophotonic label-free biosensors for environmental monitoring, Curr. Opin. Biotechnol. 45 (2017) 175–183, https://doi.org/10.1016/j.copbio.2017.03.016.

[17] R. Horváth, H.C. Pedersen, N. Skivesen, D. Selmeczi, N.B. Larsen, Optical waveguide sensor for on-line monitoring of bacteria, Opt. Lett. 28 (2003) 1233, https://doi.org/10.1364/ol.28.001233.

[18] I.R. Cooper, S.T. Meikle, G. Standen, G.W. Hanlon, M. Santin, The rapid and specific real-time detection of *Legionella pneumophila* in water samples using optical waveguide lightmode spectroscopy, J. Microbiol. Methods 78 (2009) 40–44, https://doi.org/10.1016/j.mimet.2009.04.004.

[19] A. Mathesz, S. Valkai, A. Újvárosy, B. Aekbote, O. Sipos, B. Stercz, B. Kocsis, D. Szabó, A. Dér, Integrated optical biosensor for rapid detection of bacteria, Optofluid. Microfluid. Nanofluidics 2 (2015) 15, https://doi.org/10.1515/optof-2015-0002.

[20] M. Angelopoulou, P.S. Petrou, E. Makarona, W. Haasnoot, I. Moser, G. Jobst, D. Goustouridis, M. Lees, K. Kalatzi, I. Raptis, K. Misiakos, S.E. Kakabakos, Ultrafast multiplexed-allergen detection through advanced fluidic design and monolithic interferometric silicon chips, Anal. Chem. 90 (2018) 9559–9567, https://doi.org/10.1021/acs.analchem.8b02321.

[21] Z. Liao, Y. Zhang, Y. Li, Y. Miao, S. Gao, F. Lin, Y. Deng, L. Geng, Microfluidic chip coupled with optical biosensors for simultaneous detection of multiple analytes: a review, Biosens. Bioelectron. 126 (2019) 697–706, https://doi.org/10.1016/j.bios.2018.11.032.

[22] D. Sarkar, N.S.K. Gunda, I. Jamal, S.K. Mitra, Optical biosensors with an integrated Mach-Zehnder interferometer for detection of listeria monocytogenes, Biomed. Microdevices 16 (2014) 509–520, https://doi.org/10.1007/s10544-014-9853-5.

[23] G. Steiner, Surface plasmon resonance imaging, Anal. Bioanal. Chem. 379 (2004) 328–331, https://doi.org/10.1007/s00216-004-2636-8.

[24] M. Zourob, S. Mohr, B.J. Treves Brown, P.R. Fielden, M.B. McDonnell, N. J. Goddard, An integrated optical leaky waveguide sensor with electrically induced concentration system for the detection of bacteria, Lab Chip 5 (2005) 1360–1365, https://doi.org/10.1039/b504938e.

[25] N. Tawil, E. Sacher, R. Mandeville, M. Meunier, Surface plasmon resonance detection of E. coli and methicillin-resistant *S. aureus* using bacteriophages,

Biosens. Bioelectron. 37 (2012) 24–29, https://doi.org/10.1016/j.bios.2012.04.048.

[26] C. Yu, J. Vykoukal, D.M. Vykoukal, J.A. Schwartz, L. Shi, P.R.C. Gascoyne, A three-dimensional dielectrophoretic particle focusing channel for microcytometry applications, J. Microelectromech. Syst. 14 (2005) 480–487, https://doi.org/10.1109/JMEMS.2005.844839.

[27] C.P. Jen, C.H. Weng, C. Te Huang, Three-dimensional focusing of particles using negative dielectrophoretic force in a microfluidic chip with insulating microstructures and dual planar microelectrodes, Electrophoresis 32 (2011) 2428–2435, https://doi.org/10.1002/elps.201100085.

[28] A.M. Hutchinson, Evanescent wave biosensors, Mol. Biotechnol. 3 (1995) 47–54, https://doi.org/10.1007/bf02821334.

[29] S.G. Dastider, A. Abdullah, I. Jasim, N.S. Yuksek, M. Dweik, M. Almasri, Low concentration E. coli O157:H7 bacteria sensing using microfluidic MEMS biosensor, Rev. Sci. Instrum. 89 (2018), https://doi.org/10.1063/1.5043424.

[30] L.B. Khan, H.M. Read, S.R. Ritchie, T. Proft, Artificial urine for teaching urinalysis concepts and diagnosis of urinary tract infection in the medical microbiology laboratory †, J. Microbiol. Biol. Educ. 18 (2017) 1–6, https://doi.org/10.1128/jmbe.v18i2.1325.

[31] J.G. Bartlett, Laboratory diagnosis of urinary tract infections in adult patients, Infect. Dis. Clin. Pract. 12 (2004) 360–361, https://doi.org/10.1097/01.idc.0000144910.19687.1f.

[32] N. Massad-Ivanir, G. Shtenberg, E. Segal, Optical detection of E. coli bacteria by mesoporous silicon biosensors, J. Vis. Exp. (2013) 6–13, https://doi.org/10.3791/50805.

[33] Y. Chen, J. Liu, Z. Yang, J.S. Wilkinson, X. Zhou, Optical biosensors based on refractometric sensing schemes: a review, Biosens. Bioelectron. 144 (2019) 111693, https://doi.org/10.1016/j.bios.2019.111693.

[34] O. Lazcka, F.J. Del Campo, F.X. Muñoz, Pathogen detection: a perspective of traditional methods and biosensors, Biosens. Bioelectron. 22 (2007) 1205–1217, https://doi.org/10.1016/j.bios.2006.06.036.

II.

Petrovszki D*, Krekic S*, Valkai, S, Heiner Z, & Dér A. All-Optical Switching Demonstrated with Photoactive Yellow Protein Films. Biosensors. 2021; 11(11),432. IF: 5.743

All-Optical Switching Demonstrated with Photoactive Yellow Protein Films

Dániel Petrovszki [1,2,†] **, Szilvia Krekic** [1,2,†] **, Sándor Valkai** [1] **, Zsuzsanna Heiner** [3] **and András Dér** [1,*]

1   Institute of Biophysics, Biological Research Centre, Eötvös Loránd Research Network, 6726 Szeged, Hungary; petrovszki.daniel@brc.hu (D.P.); krekic.szilvia@brc.hu (S.K.); valkai.sandor@brc.hu (S.V.)
2   Doctoral School of Multidisciplinary Medical Sciences, University of Szeged, 6720 Szeged, Hungary
3   School of Analytical Sciences Adlershof, Humboldt-Universität zu Berlin, 12489 Berlin, Germany; heinerzs@hu-berlin.de
*   Correspondence: der.andras@brc.hu
†   These authors contributed equally to this work: Dániel Petrovszki and Szilvia Krekic.

Abstract: Integrated optics (IO) is a field of photonics which focuses on manufacturing circuits similar to those in integrated electronics, but that work on an optical basis to establish means of faster data transfer and processing. Currently, the biggest task in IO is finding or manufacturing materials with the proper nonlinear optical characteristics to implement as active components in IO circuits. Using biological materials in IO has recently been proposed, the first material to be investigated for this purpose being the protein bacteriorhodopsin; however, since then, other proteins have also been considered, such as the photoactive yellow protein (PYP). In our current work, we directly demonstrate the all-optical switching capabilities of PYP films combined with an IO Mach–Zehnder interferometer (MZI) for the first time. By exploiting photoreactions in the reaction cycle of PYP, we also show how a combination of exciting light beams can introduce an extra degree of freedom to control the operation of the device. Based on our results, we discuss how the special advantages of PYP can be utilized in future IO applications.

Keywords: optical switching; integrated optics; photonics; photoactive yellow protein

1. Introduction

Integrated optics (IO) is a new alternative method of information transfer analogous to integrated electronics; however, the speed of the system at hand is dependent on the nonlinear optical (NLO) material that is applied as the active element of the IO circuit. Several materials are being developed and used in hybrid systems—mostly nonlinear crystals with π-conjugated electron systems [1,2]. It is among the long-term goals in optical telecommunication to find proper NLO materials that make possible all-optical IO switching at the proper efficiencies and speeds. Earlier works suggested the consideration of materials of biological origin for these purposes [3]. First, it was shown that (slow) spectral changes accompanying the photocycle of the chromoprotein bacteriorhodopsin (bR) are sufficient to achieve IO switching [4–6], making bR a promising candidate for IO applications. Eventually, it was also demonstrated that the primary events of the bR photocycle allow for ultrafast (sub-picosecond) switching as well [7].

The application of biological materials is appealing because of their easy availability and exceptional NLO properties [8]. Recently, another light-sensitive biomaterial, the photoactive yellow protein (PYP) [9,10], has garnered interest for IO applications because of its fast photocycle in solution and its large light-induced refractive index change in dried films [11]. PYP, being water-soluble and smaller than the bR membrane patches used previously, potentially enables its combination with special IO passive elements where the application of bR is not possible (e.g., in porous silicon structures). Based on our previous experiments, the PYP in film form could be a viable option for all-optical

switching experiments, as adding glycerol to the protein solution before drying the film helps maintain the integrity of the photocycle even in low humidity environments, allowing for the formation of the intermediate states [12], which accompanies refractive index changes of the film [11]. The photocycle of PYP consists of two main intermediates, the red-shifted pR and the blue-shifted pB (further distinguishing pR_1, pR_2, pB_1 and pB_2) [10]. By illuminating PYP with blue light, the photocycle takes place in a matter of milliseconds in solution. A study has shown that illuminating PYP during the photocycle's pB intermediate with violet light can cause a short circuit in the photocycle, making PYP return to the ground state via a faster route [13].

In this communication, our main motivation was to demonstrate that the spectral changes of the PYP photocycle can accompany refractive index changes sufficient for IO switching (similar to how it has been shown earlier for bR [4]), using the combination of a PYP film as an active NLO component and a proper integrated optical structure. Active IO elements can be implemented by utilizing a number of structures—interferometers [8,14], grating couplers [14,15], ring resonators [16], etc. The Mach–Zehnder interferometer (MZI) is one of the simplest IO passive devices, consisting of a bifurcated linear IO waveguide structure forming two arms. By adsorbing a transparent NLO material on top of the arms, adlayers are formed that can alter the effective refractive index, thus creating a phase difference between the arms joining at the output of the device, manifesting in intensity changes at the MZI's output. This principle is often used for biosensing applications, such as sensing bacteria or proteins in action, as well [17,18]. Hence, we performed all-optical switching experiments using an IO MZI, with a PYP adlayer as an active NLO component, for the first time. For the excitation of the sample, we used continuous illumination with two different laser wavelengths, targeting both the protein's pG ground state and pB intermediate state, demonstrating the different modalities of the switching capability of PYP-containing IO devices. Our results underpin that, besides bR, the chromoprotein PYP can also be considered as a promising NLO material for future, high-profile IO applications.

2. Materials and Methods

2.1. PYP Sample Preparation

The preparation method for PYP has been discussed elsewhere [10,11], but a brief summary will be given here as well. To prevent the cracking of the PYP films, 87% glycerol solution was added to the protein solution at 1:49 ratio. It was then allowed to dry in a laboratory environment (33% RH, 20 °C) for at least 24 h. By using glycerol as a ballast material, we secured the relative humidity inside the sample at ~80%, still allowing for the photocycle to take place [10,11].

2.2. IO Mach–Zehnder Interferometer Biosensor Fabrication

The fabrication method of the integrated optical Mach–Zehnder interferometer was based on the process used in one of our previous works [19], following the protocol of the manufacturer of the applied materials. The mentioned process was modified, considering the parameters used in several steps, to reach the desired thickness of the components of the device.

It should be kept in mind that MZIs have a sinusoidal transmission function (TMF), allowing for an approximate linear response of the device only in the vicinity of the inflexion points of the TMF and that this is where the bias point should be adjusted prior to the measurements. There are several methods to accomplish this task, in most cases via tuning the optical path length along one of the arms. Previously, we have used an optical solution [19]; however, here, controlled heating near one of the branches of the MZI was applied. By using a surface-sputtered heating wire close to the reference arm of the MZI, we can modify the environment's temperature and thus tune the device's bias point. According to our experience, the heating effects remained restricted to the area of the heating wire that was more than 1600 μm away from the proximal adlayer area (and even further away from the distal ones), leaving enough space for dissipation. This

solution resulted in an improved stability of the bias point during the measurements. In order to accomplish this task, a glass substrate covered by a gold heating wire structure was used, based on the method applied for surface electrode fabrication [19]. As a first step of the device fabrication, a 20 nm thick surface gold heating wire (1 kΩ resistance) capable of performing MZI's bias-point tuning was prepared on a microscope coverslip (Menzel-Gläser, Thermo Fisher Scientific, Waltham, MA, USA). Then, a rib waveguide stripe (SU-8 2002, MicroResist Technology GmbH., Berlin, Germany) of 2×2 µm was made on the mentioned glass substrate, forming the sensing optical interferometer structure in such a way that one of the arms was placed in the vicinity of the wire, as can be seen in Figure 1a.
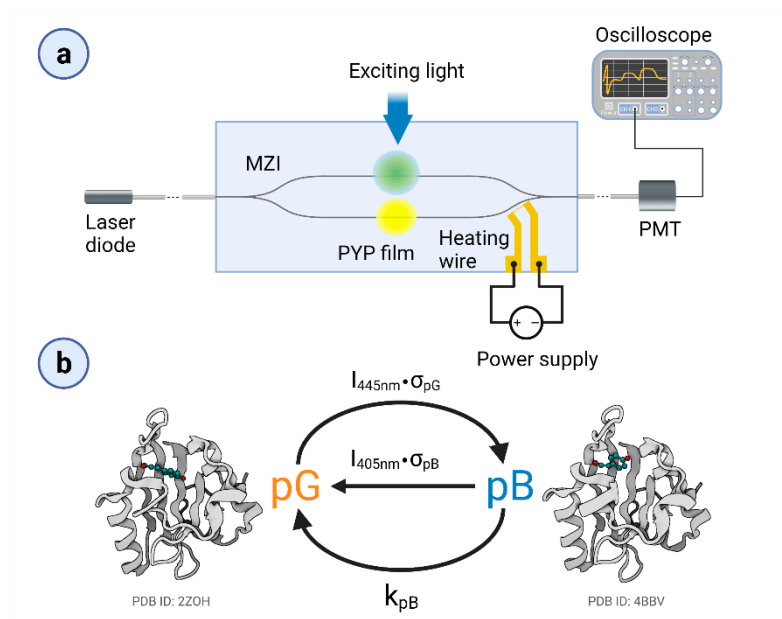
Figure 1. (**a**) Schematic representation of the measuring IO device, the MZI with the PYP adlayer and the heating wire for bias-point adjustment. (**b**) Simplified photocycle of the PYP film, with the ground state (pG) and the rate-limiting intermediate (pB). (Schematic PDB-structures are indicated for demonstration.) Long, continuous excitation with blue light results in the development of a pG–pB equilibrium. The figure was created by Biorender.com.

In the device's ready-to-use construction, the substrate was glued on a microscope slide (Menzel-Gläser, Thermo Fisher Scientific, Waltham, MA, USA) using NOA81 optical adhesive by exposing the layer with a mercury arc lamp (100W, HBO 100 Zeiss, Jena, Germany). To apply the tuning capability of the heating wire, electric wires were connected by droplets of conducting epoxy (CW2400 CircuitWorks® Conductive Epoxy, Chemtronics, Kennesaw, GA, USA) to the side contact pads of the gold structure. These were connected to the DC power supply (VLP 2403pro, Conrad Electronic, Hirschau, Germany), to perform the bias-point tuning.

2.3. Experimental Setup

A schematic representation of the experimental setup can be seen in Figure 1a. As a measuring light (referred to as a probe light), we used a green laser diode (532 nm, 50 mW, Roithner, Wien, Austria), which was coupled inside the single mode MZI by a single-mode optical fiber (S630-HP, Thorlabs GmbH, Lübeck, Germany). The fiber was positioned to the MZI's input with a micropositioner (DC-3K, Märzhäuser Wetzlar GmbH & Co. KG, Steindorf, Germany) and its optimal position was fixed with photopolymer glue (OP-66-LS, Dymax Europe GmbH, Wiesbaden, Germany). The same method was used for coupling the light out from the device. The stock solution of the PYP–glycerol mixture was pipetted on both arms of the interferometer, in ~1 mm diameter patches, before drying. To excite

and control the PYP photocycle, we used two different continuous laser beams (445 nm, 4/44 mW and 405 nm, 21.7 mW at the sample). The scheme of the simplified photocycle model is shown in Figure 1b. The duration of excitation was varied between 2 and 14 s. PYP films were deposited on both arms of the MZI but only one of them was excited at a time. For tuning the MZI's bias point, the voltage of the heating wire was varied between 0–4.6 V.

To measure the transfer characteristics of the MZI, its output was coupled to an optical fiber guiding the measuring light into a photomultiplier tube (H5783-01, Hamamatsu, Japan), from which the signal was transmitted to and recorded by a digital oscilloscope (LeCroy 9310-L, LeCroy, Chestnut Ridge, NY, USA). The voltage on the heating wire was controlled by a variable DC power supply (VLP 2403pro, Konrad Electronics, Hirschau, Germany). During each measurement, the ambient temperature was kept at 23 °C, with a relative humidity of 33%.

3. Results

3.1. Calibration of the MZI Bias Point

We first measured the transmission characteristics of our MZI by steadily increasing the voltage applied to the heating wire from 0 V to 3.5 V while detecting the intensity of the 633 nm probe light at the output of the interferometer (Figure 2). The heating caused a local thermal dilatation of the nearby waveguide area, resulting in an increase of the effective optical path length of the reference arm of the MZI, thereby introducing a phase difference between the light beams interfering with each other at the joint of the output side. The MZI's sensitivity is proportional to the first derivative of the sinusoidal transmission function, meaning that the sensitivity is smaller at the extremes, while it is the highest at the mean light intensity, compensated to an artificial zero output level by an offset voltage of the amplifier ("zero-intensity points" in Figure 2), where the derivative is the largest. By fine-tuning the power dissipated by the heating wire, one can adjust the bias point of the interferometer, before measurements, to one of these points of maximal sensitivity. One should note that changes in the ambient conditions (such as temperature and humidity) might cause a baseline drift (and an accompanying sensitivity change), so a careful control of these parameters is necessary to perform the experiments. In our case, the baseline drift could be kept on a negligible level during the time scale of the experiments (typically the 10-s to several minutes scale) by using the method of stationary local electric heating. The slight baseline drifts that still occurred during the present experiments could be attributed, rather, to local heating effects due to the several-second-long illumination of PYP films. Note that similar phenomena were observed while performing analogous experiments with bR, too [4]. Such effects, however, should play even less of role in future fast-switching experiments.

3.2. Demonstration of All-Optical Switching

To demonstrate all-optical switching, the intensity changes of the probe light were monitored, while PYP was excited by 405 nm continuous illumination. Prior to illumination, the bias point was properly adjusted to the "zero" level (Figure 2) by tuning the heating voltage to 4 V and keeping it constant during the whole period of detecting the output intensity of the MZI over time. The wavelength of the probe light was chosen to be 532 nm, so as to stay outside of the absorption range of the ground state and the intermediates of the PYP photocycle, respectively (Figure S2a), while still being in the high-refractive-index regime near the absorption peaks (Figure S2c). We used a 2 s long illumination and a subsequent 2 s break, during which no exciting light reached the sample. The significant changes of the measuring light level between the light and dark periods indicate that all-optical switching works properly (Figure 3) and that the bias point at 4 V heating voltage suffered only negligible drift. According to a brief interpretation of the observed phenomena based on a simplified reaction scheme of the PYP photocycle (Figure 1b), a steady-state equilibrium between the ground state (pG) and the rate-limiting

intermediate (pB) was formed about 2 s after excitation, in accordance with our earlier results [11], establishing a corresponding refractive index change of the protein-film ad-layer (Figure S2c). After another 2 s of the dark period, most of the protein returned to the ground state, which, upon re-excitation, yielded the same signal as when exciting the sample for the first time (Figure 3), demonstrating the repeatability of switching. (A more detailed explanation of the effects is given below, in the Discussion section.)
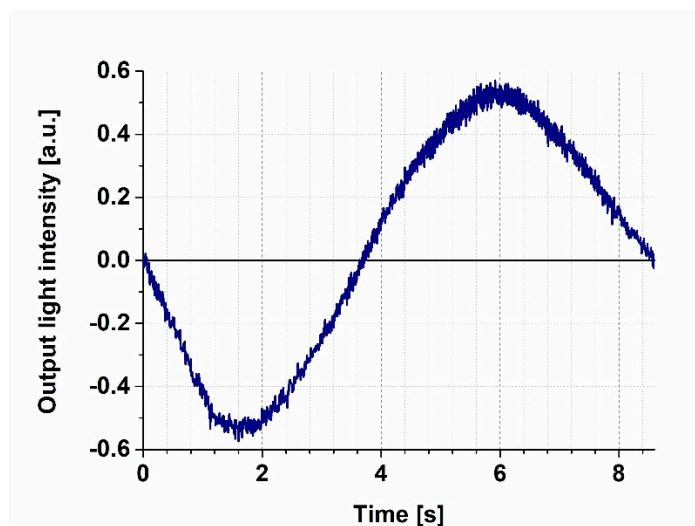
Figure 2. Transmission function of the MZI recorded by a 532 nm probe light, while increasing the heating voltage steadily from 0 to 4.6 V. Prior to each switching experiment, the bias point was adjusted to the zero level.
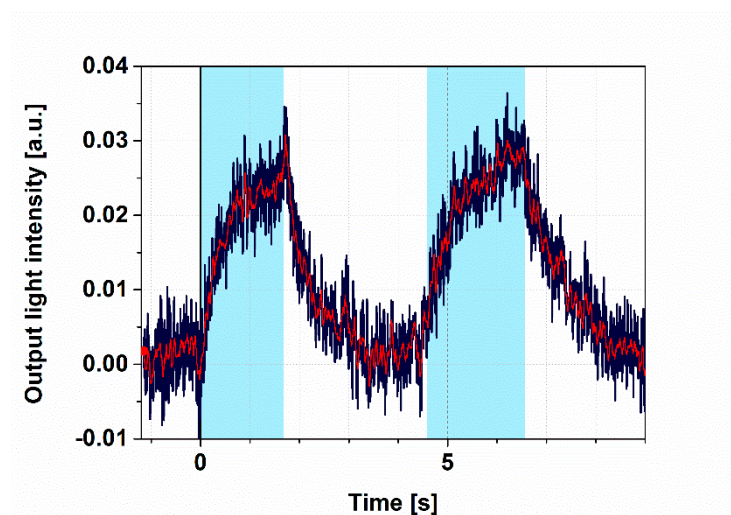
Figure 3. Demonstration of switching I. Light intensity measured at the MZI's output with two consecutive 4 s square-wave excitations. Excitation light: 445 nm, 4 mW; probe light: 532 nm; duty cycle: 50%; heating voltage: 4 V for adjusting the bias point. The blue line represents the original signal, while the red line corresponds to the filtered one. Cyan color shades indicate the periods of 445 nm illumination.

3.3. Controlling the Photocycle of PYP by Two Excitation Lights

The photocycle of PYP contains at least one light-induced shortcutting route, namely, a preferential excitation of pB drives back the molecule to the pG state [13], as shown schematically in Figure 1b. This phenomenon offers another degree of freedom to control PYP-based all-optical switching. Here, we demonstrate this opportunity by a combination of quasi-permanent illuminations.

First, we excited the PYP film with a weak (4 mW), 445 nm light for 3 s, which was followed by a relaxation in the dark, then another 3 s excitation at 405 nm (Figure 4a). Here, we can see that illuminations at both wavelengths were able to effectively excite the protein in the ground state and accumulate pB, as explained before, in agreement with its absorption spectrum (Figure S1a). The size difference of the two signals can be attributed to the much higher intensity of the 405 nm light (27 mW) that was overcompensating for the higher absorption cross section at 445 nm (4 mW).

(a)   (b)
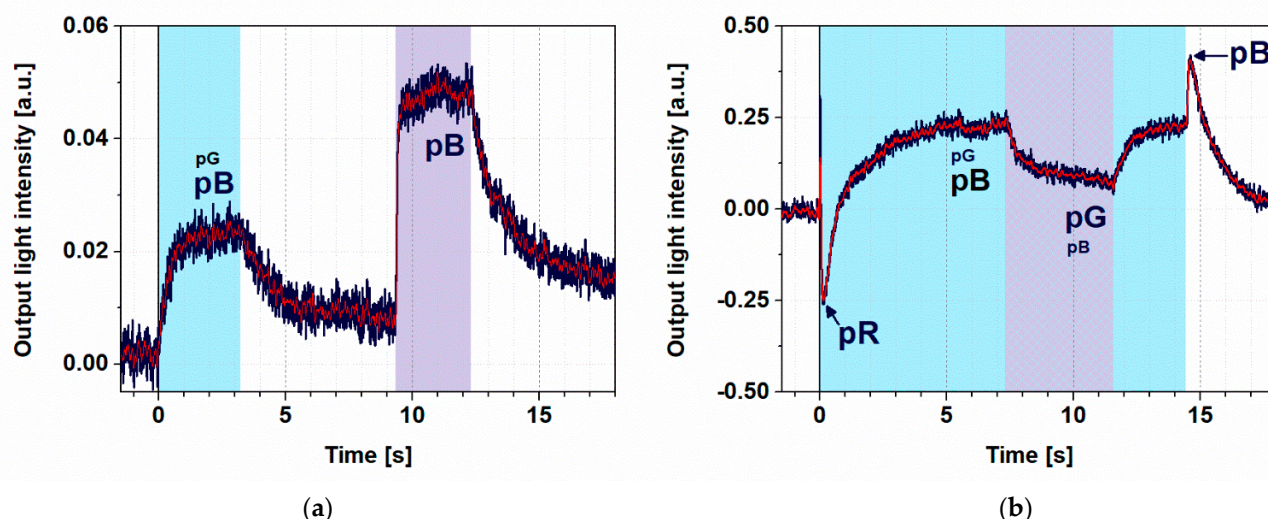
Figure 4. Demonstration of switching II. (**a**) Light intensity measured at output of the MZI, when the sample was first illuminated by a 445 nm (4 mW) excitation beam for 3 s. Then, after a dark period of 6 s, PYP was re-excited with a 405 nm illumination (27 mW) for 3 s. The bias voltage was set to 2.1 V. (**b**) Measured output signal of the MZI with 14 s excitation by a strong (44 mW) and continuous 445 nm light while, from 7 s, also exciting the film for 4 s by a 405 nm continuous light. The blue line represents the measured data, while the red is the filtered curve. The wavelength of the probe light propagating in the MZI was 532 nm in both cases. Color shades indicate the periods and wavelengths of illumination (cyan and violet for 445 nm and 405 nm, respectively, striped pattern for both). To facilitate understanding of the observed effects, we have now also indicated the states of the photocycle of PYP contributing to a greater or lesser extent (indicated by the size of the caption) to the actual effect, represented by different phases of the registered traces.

When, however, a strong 445 nm excitation was used (44 mW), a higher-level steady state was formed and the subsequently superimposed 405 nm excitation resulted in a quenching of the effect (Figure 4b), demonstrating that switching effects based on PYP films can be further controlled by a combination of illuminations. A more detailed explanation of the kinetic effects is given in the next section.

4. Discussion

4.1. Model Calculations

To interpret the registered kinetic traces, let us consider a typical scheme for photoexcitable disordered systems, where a primary absorption is followed by thermally driven processes, such as the stabilization of the light-induced conformational change and a subsequent relaxation [20–22]. While a single-photon absorption process is considered extremely fast, on the level of population of atoms or molecules the primary reaction is described by a rate constant that is proportional to the excitation light intensity (I) and an efficiency factor (σ), including the absorption cross section; on the other hand, the thermal processes are assumed to be light-independent [7,20–22]. This general scheme holds for light-driven chromoproteins as well; however, here, the thermally induced relaxation process is usually more complex than, e.g., in semiconductors [7]. (For PYP, such a complex, though not complete, model is shown in Figure S1 and the corresponding kinetic equations are shown

in Supporting Information.) Note, however, that in a first-order unidirectional reaction scheme, the slowest (rate-limiting) transitions dominate the kinetics. If, e.g., the I·σ for a light-driven reaction is much smaller than the rate constants of the subsequent thermal transitions, the contribution of the latter to the transient or equilibrium population of the intermediate states is negligible. Hence, at the relatively low light intensity levels provided by the continuous-wave lasers used in our experiments, we consider a simplified photo-cycle scheme, keeping only the ground state (pG) and the rate-limiting pB intermediate, accumulating to the largest extent under such circumstances (Figure 1b). (The differential equation system describing the kinetics is also reduced in this case, accordingly.) For the light-induced reactions under stationary illumination at 445 and 405 nm, we can introduce the quasi-first-order rate constants $I_{445nm} \cdot \sigma_{pG}$ and $I_{405nm} \cdot \sigma_{pB}$, respectively. (Here I_{445nm} and I_{405nm} denote the continuous blue and violet light intensities, while σ_{pG} and σ_{pB} include the absorption cross sections and the quantum efficiencies of the light-induced photocycle reactions at 445 and 405 nm, respectively.) The rate constant of the thermally induced decay of the pB intermediate is denoted by k_{pB}. Under continuous blue-light illumination (and in the absence of violet light), the equilibrium concentration of pG and pB can be expressed as follows:

$$[pB] = PG_0 \cdot I_{445nm} \cdot \frac{\sigma_{pG}}{I_{445nm} \cdot \sigma_{pG} + k_{pB}} \text{ and } [pG] = PG_0 \cdot I_{445nm} \cdot \frac{k_{pB}}{\left(I_{445nm} \cdot \sigma_{pG} + k_{pB} \right)}, \quad (1)$$

where [pG] and [pB] are concentrations of the ground state and the pB intermediate, respectively, while $PG_0 = [pG] + [pB]$ and $d[pG]/dt = d[pB]/dt = 0$.

If both the blue and the violet lights are present, the photocycle scheme becomes somewhat more complex: the pG to pB transition will now be driven by the sum of two rate constants ($I_{445nm} \cdot \sigma_{pG} + I_{405nm} \cdot \sigma_{pG405}$), where σ_{pG405} stands for the absorption cross section of pG at 405 nm. The apparent rate constant of the pB to pG transition will be similarly modified to $I_{445nm} \cdot \sigma_{pB445nm} + I_{405nm} \cdot \sigma_{pG}$. It is, however, evident from Figure S2a, that $\sigma_{pG405} < \sigma_{pG}$, while on the other hand, $\sigma_{pB445nm} << \sigma_{pB}$. Being the blue and violet excitation light intensities of the same order of magnitude, we can end up with the following formula for the approximate concentrations of PYP states under two-color excitation:

$$[pB] = PG_0 \cdot I_{445nm} \cdot \frac{\sigma_{pG}}{\left(I_{445nm} \cdot * \sigma_{pG} + I_{405nm} \cdot \sigma_{pB} + k_{pB} \right)}, \text{ and } [pG] = PG_0 \cdot I_{445nm} \cdot \frac{k_{pB}}{\left(I_{445nm} \cdot \sigma_{pG} + I_{405nm} \cdot \sigma_{pB} + k_{pB} \right)}. \quad (2)$$

When exciting the pG ground state—which has an absorption maximum at 446 nm—with sufficiently high light intensity (i.e., if $I_{445nm} \cdot \sigma_{pG} >> k_{pB}$), a steady-state equilibrium between pG and pB is established according to (1), with the PYP primarily being in the pB state, since the $I_{445nm} \cdot \sigma_{pG}$ contribution is dominating the k_{pB} kinetic constant. From what we have seen in previous experiments, too [12], the steady state forms in the matter of a few seconds under such conditions, while the protein returns fully to the ground state after excitation ceases. If we use two different wavelengths for exciting the sample, choosing one to target, rather, pG, and another to target, rather, the pB intermediate, we can shift the concentration ratio of intermediates in the formed steady state. By introducing $I_{405nm} \cdot \sigma_{pB}$ into the rate equation we preferentially excite the dominant pB state, inducing a shortcut reaction back into pG [13]. The equilibrium concentration of pB and pG in this case are given by equation (2). The absorption spectra of the ground and intermediate states of the photocycle are shown in Figure S2a, from which, the corresponding difference absorption spectra can be determined (Figure S2b) and the refractive index difference spectra can be calculated according to the Kramers–Kronig relations [23] (Figure S2c).

The corresponding light-induced refractive index change of the PYP adlayer adsorbed on the MZI induces a phase shift in the measuring arm of the MZI, resulting in an intensity change at the output. The steady state, formed by using both excitation wavelengths simultaneously, has a different refractive index than that formed by illuminating the film at

only one wavelength. This phenomenon makes a detectable output intensity difference between the two states, which is utilized in our switching experiments. The transient positive and negative peaks in Figure 4b must have different routes. The latter we attribute to a transient accumulation of pR, a red-shifted photocycle intermediate (Figure S1), at high 445 nm intensities before decaying to pB, dominating the steady state [10]. On the other hand, the positive peak followed by the switch-off is probably due to a shortcutting effect of the 445 nm light itself, exciting the accumulating intermediate(s) at high intensities.

4.2. Evaluation of Kinetics

Although, in the equations presented in this chapter, we deal only with steady-state concentrations and did not intend to solve the complex, coupled differential equation system describing the photocycle kinetics (Supporting Information), some straightforward statements can still be made for the kinetics of rate-limiting reactions. In case of all transitions to the dark state after illumination, e.g., the slowest rate of the thermal reactions of the photocycle, namely, the pB to pG transition, is supposed to determine the time constant of relaxation. In fact, the results of the exponential fitting of these phases in Figures 3 and 4 all show a similar value within the estimated uncertainty limits of the experiments and evaluation (1.2 ± 0.2 s). This value is actually also congruent with the findings of earlier measurements on similar samples [12]. In the case of transitions to light-driven equilibria of various photocycle intermediates, on the other hand, the observed rates are always a mixture of virtual rate constants, due to the illumination driving the initial population towards a new equilibrium ($I^*\sigma$) and a thermal rate constant (k), i.e., $k_{virtual} = I^*\sigma + k$, as is discussed above, too. This means that these transitions should normally be faster than the ones discussed before. In fact, fitting the rising phases of the light-induced signals yields shorter time constants (τ_{rise}) than the ones corresponding to relaxations. In addition, the rates belonging to the same transitions normally increase by increasing intensity of excitation, as expected from the above equation ($\tau_{rise} = 600 \pm 100$ ms for the 4 mW excitation at 445 nm and $\tau_{rise} = 200 \pm 40$ ms for the 27 mW excitation at 405 nm. (Note that in the latter case, the higher intensity overcompensated the smaller absorption cross section (σ).) The kinetics of the PYP photocycle, however, get more complex when light-induced back-reactions are also involved, either due to a simultaneous excitation at two wavelengths, or to an excitation of more than one intermediate by the same excitation light (Figure 4b). The latter occurs, e.g., when a high-intensity illumination can compete with the pR to pB decay, resulting in the accumulation of pR. However, because of the highly overlapping spectra of pG and PR, the 445 nm excitation light drives back a considerable population of pR to pG before being able to get further to pB, following the normal pathway of the photocycle. This effect actually results in a slow-down of the formation of pB populations, even at high intensities of the excitation light. Right after switching off the strong 445 nm illumination (Figure 4b, near 14 ms), however, we see a fast rise (40 ms), which is due to the population of molecules that have been driven out from the ground state (pG) and, in the absence of a back-reaction, reach the pB state rapidly.

Although establishing a comprehensive model for the in-depth, quantitative description of the phenomena is beyond the scope of this short, application-oriented study, we could show that the PYP photocycle can be controlled by various illuminations. This allows for a sort of dynamic "programing" of PYP-based NLO materials by light, a potentially utilizable feature in future IO applications. According to our experiments, the light-induced intensity changes accompanying the PYP photocycle cover a major part of the full dynamic range of the Mach–Zehnder interferometer (Figures 2 and 4b), clearly proving the IO switching ability of PYP-based NLO films. Comparing the results with those of switching experiments carried out on a Mach–Zehnder interferometer structure doped by bR films also shows that the quality of the traces obtained by the two experiments are rather similar [4].

4.3. On the Opportunity of Increasing Switching Speed

Based on the present results and those of some recent publications [12,24], it can also be envisioned that, similarly to the case of bR, ultrafast all-optical switching by PYP films as NLO materials should be feasible. On the one hand, the kinetics analysis of our results under 4.2 implies that increasing the intensity of the excitation light increases the switching speed as well. However, we also saw that at higher light intensities, one should consider a more detailed photocycle scheme, including the faster-forming and decaying intermediates (Figure S1). On the other hand, Konold et al. have recently shown that large absorption changes occur in PYP samples after a strong, 50 fs excitation, still in the femtosecond time scale [24], where a blue-shifted intermediate (called "ES", after "excited state") develops. On the ns to μs time scale, it transforms to a red-shifted intermediate (pR) (Figure S1), which is known to transform later to a blue-shifted pB in the course of milliseconds [25] at room temperature (Figure S1). The absorption spectra of the pR and pB intermediates have been determined from kinetic experiments [25] (Figure S2a). From the Kramers–Kronig relations of optics, connecting the real and imaginary parts of the complex refractive index, one can then calculate the corresponding refractive index spectra [23] (Figure S2c). Although the full absorption spectrum of the ES intermediate has not been published yet, the relative sizes of the light-induced differential spectra of ES, pR and pB (Figure S2b) imply that the amplitude of the refractive index change associated to the pG to ES transition will most probably exceed those of the pG to pR and pG to pB transitions. Since the results of the present paper prove that refractive index changes associated with the pG to pB transition are sufficient for integrated optical switching, it can be safely stated that it should be also true for the pG to ES transition, which takes place on the femtosecond time scale, similar to the bR-I transition of bacteriorhodopsin [7]. Hence, it can be anticipated that an ultrafast integrated optical switching based on the primary phototransition of PYP should also be feasible to demonstrate at high-intensity short-pulse excitations with a proper femtosecond setup.

5. Conclusions and Outlook

Our results demonstrate that dried films of PYP can be used for all-optical IO switching because of the favorable nonlinear optical properties of the protein film. For PYP, being water-soluble and smaller than the bR membrane patches used previously theoretically enables its combination with special IO passive elements where the application of bR is not possible (e.g., with porous silicon—pSi—structures). According to a solid functionalization protocol developed for pSi structures, they can accommodate a variety of soluble proteins; as it has already been demonstrated for a couple of proteins of various sizes and compositions [26,27], so it is expected to be achievable for PYP as well.

The small size and water solubility are not the only properties that distinguish PYP from bR and allow for its unique applications. Another important feature is the different spectral range of the main absorption bands and refractive index changes, which are blue shifted in PYP by ca. 100 nm as compared to bR, making a complementary spectral range available for IO operations using biophotonic film as active, nonlinear optical materials.

For utilization in telecommunication, however, much faster switching procedures are usually required, since the present state of the art for solid-state NLO materials is in the subnanosecond range [28]. Similarly to the case of bacteriorhodopsin [7], the light-induced primary photocycle reactions of PYP [24] theoretically allow for such a short switching time regime, whose demonstration should be the subject of follow-up papers.

on the 1 ms to 100 ms time scale (Khoroshyy et al., Krekic et al., 2019). Both pR and pB can be driven back by photoexcitation to pG. A differential equation system describing the kinetics of the concentrations of the photocycle intermediates is also presented. Figure S2. (a) Absorption spectra of the ground state (pG, black), an early intermediate (pR, red) and the rate-limiting intermediate (pB, blue) of the PYP photocycle, as determined from absorption kinetic experiments (Khoroshyy et al.). (b) Difference-absorption spectra of pR (red) and pB (blue), as compared to the ground state (pG). (c) Calculated change of the refractive index spectrum upon the rate-limiting pG → pB transition (underlying the effects described in the main body of the paper), using the Kramers–Kronig relations. For more details, see Fábián et al.

Author Contributions: A.D. created the research idea. The MZI was prepared by D.P. The measuring setup was designed and built by S.V., D.P. and A.D. The PYP sample was prepared by S.K. The measurements were done by D.P., S.K., S.V. and A.D. The quantitative evaluation of the measurements was done by Z.H. The manuscript was written by S.K., D.P., S.V., Z.H. and A.D. All authors have read and agreed to the published version of the manuscript.

Conflicts of Interest: The authors declare no conflict of interest or state.

References

1. Hales, J.M.; Matichak, J.; Barlow, S.; Ohira, S.; Yesudas, K.; Brédas, J.L.; Perry, J.W.; Marder, S.R. Design of polymethine dyes with large third-order optical nonlinearities and loss figures of merit. *Science* **2010**, *327*, 1485–1488. [CrossRef]
2. Hu, X.; Jiang, P.; Ding, C.; Yang, H.; Gong, Q. Picosecond and low-power all-optical switching based on an organic photonic-bandgap microcavity. *Nat. Photonics* **2008**, *2*, 185. [CrossRef]
3. Fábián, L.; Mathesz, A.; Dér, A. New trends in biophotonics. *Acta Biol. Szeged.* **2015**, *59* (Suppl. S2), 189–202.
4. Dér, A.; Valkai, S.; Fábián, L.; Ormos, P.; Ramsden, J.J.; Wolff, E.K. Integrated Optical Switching Based on the Protein Bacteriorhodopsin†. *Photochem. Photobiol.* **2007**, *83*, 393–396. [CrossRef]
5. Ormos, P.; Fábián, L.; Oroszi, L.; Wolff, E.K.; Ramsden, J.J.; Dér, A. Protein-based integrated optical switching and modulation. *Appl. Phys. Lett.* **2002**, *80*, 4060–4062. [CrossRef]
6. Roy, S.; Sethi, P.; Topolancik, J.; Vollmer, F. All-optical reversible logic gates with optically controlled bacteriorhodopsin protein-coated microresonators. *Adv. Opt. Technol.* **2012**, 727206. [CrossRef]
7. Fábián, L.; Heiner, Z.; Mero, M.; Kiss, M.; Wolff, E.K.; Ormos, P.; Osvay, K.; Dér, A. Protein-based ultrafast photonic switching. *Opt. Express* **2011**, *19*, 18861–18870. [CrossRef]
8. Mathesz, A.; Fábián, L.; Valkai, S.; Alexandre, D.; Marques, P.V.; Ormos, P.; Wolff, E.K.; Dér, A. High-speed integrated optical logic based on the protein bacteriorhodopsin. *Biosens. Bioelectron.* **2013**, *46*, 48–52. [CrossRef] [PubMed]
9. Meyer, T.E. Isolation and characterization of soluble cytochromes, ferredoxins and other chromophoric proteins from the halophilic phototrophic bacterium Ectothiorhodospira halophila. *Biochim. Et Biophys. Acta (BBA)-Bioenerg.* **1985**, *806*, 175–183. [CrossRef]
10. Meyer, T.E.; Yakali, E.; Cusanovich, M.A.; Tollin, G. Properties of a water-soluble, yellow protein isolated from a halophilic phototrophic bacterium that has photochemical activity analogous to sensory rhodopsin. *Biochemistry* **1987**, *26*, 418–423. [CrossRef]
11. Krekic, S.; Zakar, T.; Gombos, Z.; Valkai, S.; Mero, M.; Zimányi, L.; Heiner, Z.; Dér, A. Nonlinear Optical Investigation of Microbial Chromoproteins. *Front. Plant Sci.* **2020**, *11*, 1567. [CrossRef] [PubMed]
12. Krekic, S.; Nagy, D.; Taneva, S.G.; Fábián, L.; Zimányi, L.; Dér, A. Spectrokinetic characterization of photoactive yellow protein films for integrated optical applications. *Eur. Biophys. J.* **2019**, *48*, 465–473. [CrossRef]
13. Hendriks, J.; van Stokkum, I.H.; Crielaard, W.; Hellingwerf, K.J. Kinetics of and intermediates in a photocycle branching reaction of the photoactive yellow protein from Ectothiorhodospira halophila. *FEBS Lett.* **1999**, *458*, 252–256. [CrossRef]
14. Fábián, L.; Wolff, E.K.; Oroszi, L.; Ormos, P.; Dér, A. Fast integrated optical switching by the protein bacteriorhodopsin. *Appl. Phys. Lett.* **2010**, *97*, 023305. [CrossRef]
15. Korposh, S.; James, S.; Partridge, M.; Sichka, M.; Tatam, R. All-optical switching based on optical fibre long period gratings modified bacteriorhodopsin. *Opt. Laser Technol.* **2018**, *101*, 162–171. [CrossRef]
16. Topolancik, J.; Vollmer, F. All-optical switching in the near infrared with bacteriorhodopsin-coated microcavities. *Appl. Phys. Lett.* **2006**, *89*, 184103. [CrossRef]
17. Mathesz, A.; Valkai, S.; Újvárosy, A.; Aekbote, B.; Sipos, O.; Stercz, B.; Kocsis, B.; Szabó, D.; Dér, A. Integrated optical biosensor for rapid detection of bacteria. *Optofluid. Microfluid. Nanofluid.* **2015**, *2*, 15–21. [CrossRef]

18. Jankovics, H.; Kovacs, B.; Saftics, A.; Gerecsei, T.; Tóth, É.; Szekacs, I.; Vonderviszt, F.; Horvath, R. Grating-coupled interferometry reveals binding kinetics and affinities of Ni ions to genetically engineered protein layers. *Sci. Rep.* **2020**, *10*, 22253. [CrossRef]

19. Dér, A.; Valkai, S.; Mathesz, A.; Andó, I.; Wolff, E.K.; Ormos, P. Protein-based all-optical sensor device. *Sens. Actuators B Chem.* **2010**, *151*, 26–29. [CrossRef]

20. Abdulhalim, I. Model for Photoinduced Defects and Photorefractivity in Optical Fibers. *App. Phys. Lett.* **1995**, *66*, 3248–3250. [CrossRef]

21. Abdulhalim, I. Kinetic model for photoinduced and thermally induced creation and annihilation of metastable defects in hydrogenated amorphous silicon. *J. Appl. Phys.* **1995**, *77*, 1897–1901. [CrossRef]

22. Abdulhalim, I.; Gelbaor, M.; Klebanov, M.; Lyubin, V. Photoinduced phenomena in nano-dimensional glassy As2S3 films. *Opt. Mater. Express* **2011**, *1*, 1192–1201. [CrossRef]

23. Fábián, L.; Krekic, S.; Tóth-Boconádi, R.; Taneva, S.G.; Bálint, A.M.; Nánai, L.; Dér, A. Integrated optical investigation of two light-sensitive proteins. *AIP Conf. Proc.* **2017**, *1796*, 040001.

24. Konold, P.E.; Arik, E.; Weißenborn, J.; Arents, J.C.; Hellingwerf, K.J.; van Stokkum, I.H.; Kennis, J.T.; Groot, M.L. Confinement in crystal lattice alters entire photocycle pathway of the Photoactive Yellow Protein. *Nat. Commun.* **2020**, *11*, 4248. [CrossRef] [PubMed]

25. Khoroshyy, P.; Dér, A.; Zimányi, L. Effect of Hofmeister cosolutes on the photocycle of photoactive yellow protein at moderately alkaline pH. *J. Photochem. Photobiol. B Biol.* **2013**, *120*, 111–119. [CrossRef] [PubMed]

26. Hajdu, K.; Gergely, C.; Martin, M.; Zimányi, L.; Agarwal, V.; Palestino, G.; Hernádi, K.; Németh, Z.; Nagy, L. Light-harvesting bio-nanomaterial using porous silicon and photosynthetic reaction center. *Nanoscale Res. Lett.* **2012**, *7*, 400. [CrossRef]

27. Palestino, G.; Martin, M.; Agarwal, V.; Legros, R.; Cloitre, T.; Zimányi, L.; Gergely, C. Detection and light enhancement of glucose oxidase adsorbed on porous silicon microcavities. *Phys. Status Solidi C* **2009**, *6*, 1624–1628. [CrossRef]

28. Lin, G.R.; Su, S.P.; Wu, C.L.; Lin, Y.H.; Huang, B.J.; Wang, H.Y.; Tsai, C.T.; Wu, C.I.; Chi, Y.C. Si-rich SiNx based Kerr switch enables optical data conversion up to 12 Gbit/s. *Sci. Rep.* **2015**, *5*, 9611. [CrossRef]

III.

Petrovszki D*, Walter FR*, Vigh JP, Kocsis A, Valkai S, Deli MA, & Dér A. Penetration of the SARS-CoV-2 Spike Protein across the Blood–Brain Barrier, as Revealed by a Combination of a Human Cell Culture Model System and Optical Biosensing. Biomedicines. 2022; 10(1), 188. IF: 4.757

Article

Penetration of the SARS-CoV-2 Spike Protein across the Blood–Brain Barrier, as Revealed by a Combination of a Human Cell Culture Model System and Optical Biosensing

Dániel Petrovszki [1,2,†], Fruzsina R. Walter [1,†], Judit P. Vigh [1,3], Anna Kocsis [1], Sándor Valkai [1], Mária A. Deli [1,*] and András Dér [1,*]

1   Institute of Biophysics, Biological Research Centre, ELKH, Temesvári Krt. 62, H-6726 Szeged, Hungary; petrovszki.daniel@brc.hu (D.P.); walter.fruzsina@brc.hu (F.R.W.); vigh.judit@brc.hu (J.P.V.); annabrief@gmail.com (A.K.); valkai.sandor@brc.hu (S.V.)
2   Doctoral School of Multidisciplinary Medical Sciences, University of Szeged, Dóm Tér 9, H-6720 Szeged, Hungary
3   Doctoral School of Biology, University of Szeged, Közép Fasor 52, H-6726 Szeged, Hungary
*   Correspondence: deli.maria@brc.hu (M.A.D.); der.andras@brc.hu (A.D.)
†   These authors contributed equally to this work.

Abstract: Since the outbreak of the global pandemic caused by severe acute respiratory coronavirus 2 (SARS-CoV-2), several clinical aspects of the disease have come into attention. Besides its primary route of infection through the respiratory system, SARS-CoV-2 is known to have neuroinvasive capacity, causing multiple neurological symptoms with increased neuroinflammation and blood–brain barrier (BBB) damage. The viral spike protein disseminates via circulation during infection, and when reaching the brain could possibly cross the BBB, which was demonstrated in mice. Therefore, its medical relevance is of high importance. The aim of this study was to evaluate the barrier penetration of the S1 subunit of spike protein in model systems of human organs highly exposed to the infection. For this purpose, in vitro human BBB and intestinal barrier cell–culture systems were investigated by an optical biosensing method. We found that spike protein crossed the human brain endothelial cell barrier effectively. Additionally, spike protein passage was found in a lower amount for the intestinal barrier cell layer. These observations were corroborated with parallel specific ELISAs. The findings on the BBB model could provide a further basis for studies focusing on the mechanism and consequences of spike protein penetration across the BBB to the brain.

Keywords: biosensor; Caco-2 cells; coronavirus spike protein; human brain endothelial cell; integrated optics; Mach–Zehnder interferometer; permeability; tissue barriers

1. Introduction

1.1. Scientific Background and Purpose of the Study

At the end of 2019, a novel respiratory coronavirus was reported by Chinese authorities, which we know now as the severe acute respiratory syndrome coronavirus 2 (SARS-CoV-2), causing a global pandemic. Infection occurs primarily by the inhalation of the virus, which can spread through epithelial and endothelial barriers to multiple organs, leading to systemic inflammation [1]. It has been established that the binding of the CoV-2 spike glycoprotein to angiotensin-converting enzyme 2 (ACE2) triggers penetration of the virus into endothelial and epithelial cells [2]. While the S1 subunit of the spike protein is responsible for anchoring the virion by binding to the ACE2 cellular receptor of the host cell, the S2 subunit enhances the fusion of the viral and the host cell membranes. The fusion is mediated by the S2 subunit that is activated by the transmembrane protease serine 2 (TMPRSS2) cleaving the spike protein at the S1/S2 sites (Figure 1).
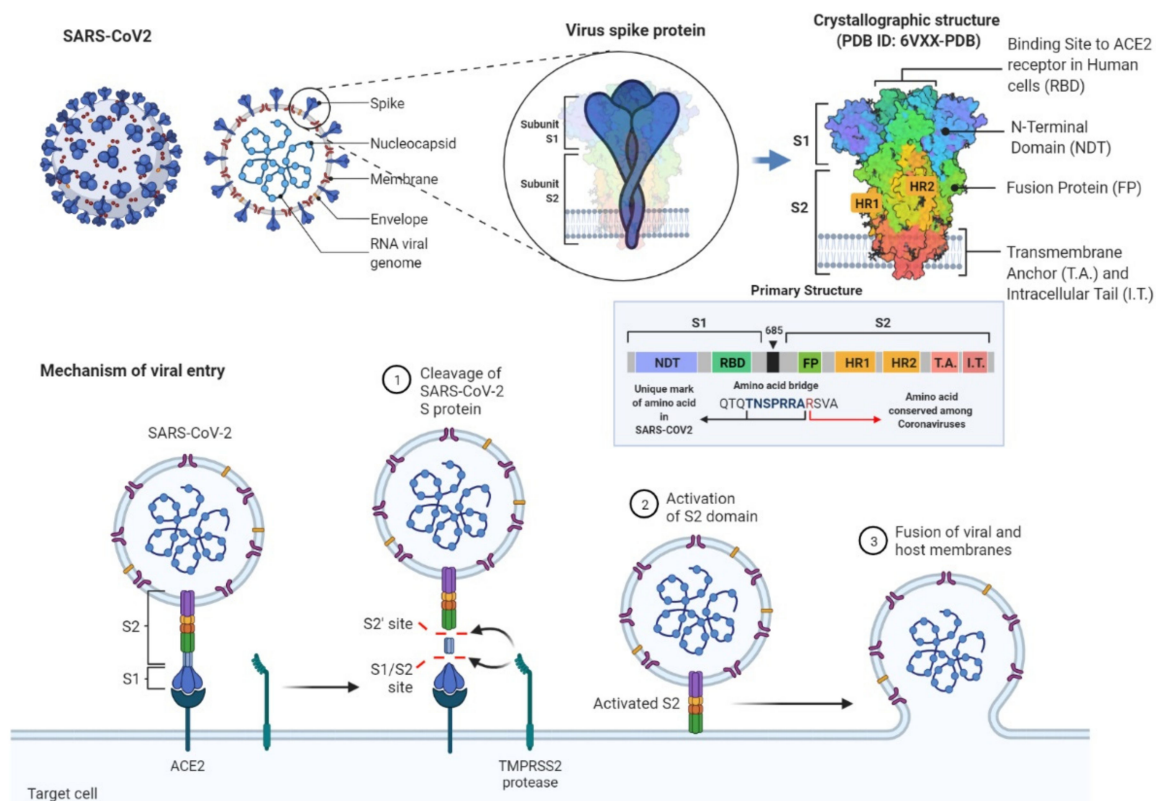
Figure 1. The schematic representation of the SARS-CoV-2 and its surface spike protein structure with their structural descriptions and detailed mechanisms of the viral entry to cells during infection. Spike protein plays a crucial role in this process. While S1 subunit is responsible for anchoring the virion by binding to the cellular receptor angiotensin-converting enzyme 2 (ACE2) of the host cell, S2 subunit enhances the fusion of the viral and the host cell membranes. The fusion is mediated by the S2 subunit that is activated by the transmembrane protease serine 2 (TMPRSS2) cleaving the spike protein at the S1/S2 sites. Adapted from "An In-depth Look into the Structure of the SARS-CoV2 Spike Glycoprotein", "Human Coronavirus Structure" and "Mechanism of SARS-CoV-2 Viral Entry" by BioRender.com (accessed on 30 November 2021) [3].

It is well known that, among other targets, SARS-CoV-2 has a strong neuroinvasive capacity causing multiple neurological symptoms [4] with increased blood–brain barrier (BBB) damage and neuroinflammation [5]. There are some indications, however, that not only the SARS-CoV-2 virus but also its S1 spike glycoprotein alone may be responsible for a major part of these problems [6–12]. It has been shown that the CoV-2 spike protein or its subunits can be relatively easily detached from the virion, due to enzymatic cleavage [6] or heat stress [7]. As a corollary, S1 spike protein subunits can be detected from the blood, and S1 protein serum levels are associated with the severity of the disease [8]. Moreover, the S1 spike protein can activate platelet aggregation [9], leading to symptoms similar to heparin-induced thrombocytopenia [10]. The Toll-like receptor signaling pathway can be stimulated in macrophages [11], and endothelial function can be impaired via a similar route by the S1 spike protein [12].

Due to the medical relevance and the pathological importance of the S1 spike protein, its detection in the blood stream during infection has come into attention by different methods. It has been shown that the S1 protein of the SARS-CoV-2 crosses the BBB in mice, both when administered intranasally or intravenously [13]; however, the penetration of the S1 spike protein has not been proven on human models of biological barriers. In our present study, we investigated the passage of the SARS-CoV-2 S1 spike protein across cell culture models of the blood–brain and intestinal barriers by using a sensitive optical biosensor system.

1.2. Methodological Background

Several highly accurate laboratory methods to detect the virus, and monitor its worldwide propagation, have become a part of the everyday life. By now, people have become acquainted with real-time PCR, as one of the most accurate laboratory techniques to identify the virus even at the early stages of infection in patients [14]. Serological tests have also been widely used in clinical practice during the consecutive waves of the disease.

In order to identify the S1 spike protein being in the focus of the present study, alternative methods are required, based for example on specific antigen–antibody interactions [15]. These techniques are also advantageous to substitute tests requiring laboratory-intensive environment to monitor the spreading of the virus in real-time, even in regions of less-developed healthcare [14,16–18]. In such cases, point-of-care diagnostic techniques are preferred to perform rapid, sensitive, and specific detection of the pathogen. Consequently, several biosensor applications as point-of-care diagnostic devices have been developed to provide a good alternative to more complex tests in clinical diagnostics.

In recent years, optical biosensors, more specifically, portable, integrated optical sensor devices, where an optical waveguide is the key element of the detection process, emerged as promising approaches. Most of these devices perform label-free detection, which does not affect their sensitivity significantly but makes them cost-effective. The working principle of such optical biosensors relies on different ways of physical transduction, including interferometry, resonator, or plasmonic techniques [19–21]. These sensors translate the capture of an analyte to a measurable change of an optical property, such as refractive index, intensity, or resonance shift, via resonator or interferometric methods. Among optical biosensing platforms, integrated optical Mach–Zehnder interferometer (MZI) is a commonly used interferometric construction, due to its high sensitivity and portability. In this system, the detection is based on the specific binding of the target molecule to the measuring arm of the interferometer made up by a waveguide structure. To reach specificity, the waveguide surface is functionalized by recognition elements, such as receptors, antibodies, or enzymes [21]. Binding of the analyte causes an effective refractive index change in the detection region of the measuring arm, caused by structural changes of the adlayer in the evanescent field of the waveguide. Therefore, a phase difference arises between the propagating waves in the measuring and reference arms, resulting in a change of the output light intensity (For more detail, see Materials and Methods).

1.3. Structural Outline of the Paper

The aim of the present study was to investigate and verify whether the SARS-CoV-2 surface S1 spike protein subunit, circulating in the human body during viral infection, could penetrate across tissue barriers directly exposed to the protein. To achieve this goal, the S1 spike protein subunit and in vitro models of the BBB (co-culture of human endothelial cells and pericytes) and the intestinal barrier (Caco-2 cells) were used. To investigate the penetration of S1 proteins across the barrier models permeability assays were performed. To evaluate the amount of spike protein that crossed biological barrier models, an optical biosensing approach was applied. An enzyme-linked immunosorbent assay (ELISA) was used as an alternative detection technique of the target protein validating the results of the optical biosensing technique. After a detailed description of the sensor device, the characterization of the cell culture models is presented, followed by the functionalization of the sensor detection surface, the optical biosensing method, and ELISA immunoassay experiments.

2. Materials and Methods

2.1. Integrated Optical Mach—Zehnder Interferometer

2.1.1. Fabrication of the Biosensor

The sensor devices used in this study were fabricated and improved based on the construction of the integrated optical MZI interferometer biosensor described in detail in a previous study of our research group [22]. The waveguide structure was made by direct

laser writing technique (μPG-101 machine, $\lambda = 375$ nm, Heidelberg Instruments GmbH, Heidelberg, Germany), as was previously described [23]. To improve the waveguiding performance of the photopolymer structure, the glass substrate was covered with an adhesion promoter layer (Surpass 3000, MicroResist Technology GmbH, Berlin, Germany) by dip coating, following the protocol of the manufacturer. A microfluidic channel was fabricated and integrated in the final form of the sensor device to work with fluid samples [24]. As in our previous study [22], heating was used for setting the bias point prior to the measurements by applying DC voltage on a substrate-bound 20 nm thick gold microheater structure. To improve its adherence to the substrate 10 nm thick Cr was deposited followed by the deposition of the desired gold layer, as was described in one of our latest works [23]. The heater was placed to leave enough space for dissipation, so that the heating of the fluid sample and the measuring arm of the interferometer was avoided, while stabile bias point tuning was achieved.

2.1.2. Biofunctionalization of the Waveguide Structure

To perform specific S1 spike protein detection, the waveguide structure of the interferometer was functionalized in the microchannel. Both interferometer arms, having equal optical length for sensing, were functionalized with antibodies to be capable of specific detection. During the process of the functionalization, the microfluidic channels of the biosensor were filled up by pumping a syringe with a volume of 1 mL (SP210IWZ syringe pump, World Precision Instruments Inc., Sarasota, FL, USA). Firstly, the PDMS microfluidic channels were cleaned with ethanol. Then the microchannels were filled with antibody activation reagent solution of diluted Mix&Go™ at a 1:20 ratio of the stock solution (Mix&Go™ Biosensor, AnteoTech Ltd., Brisbane, Australia) and deionized (18.2 MΩ) MilliQ water (Synergy® UV Water Purification System, Merck-Millipore, Burlington, MA, USA). Incubation lasted for 30 min to enhance the functionalization of waveguide surfaces. Next, the channels were washed by PBS solution ($1\times$, pH = 7.4). The functionalization was performed by filling up the channels with the antibody solution (MonoRab™ SARS-CoV-2 Neutralizing Antibody (BS-R2B2) (Cat. No.: A02051-100), mAb, Rabbit, GenScript, Piscataway, NJ, USA, diluted with $1\times$PBS at a final concentration of 5 μg/mL) and incubation at 4 °C, overnight. Next day the devices with antibody layers on the waveguide surfaces were washed with a buffer solution (0.1% bovine serum albumin (BSA)–Ringer–HEPES (RH) buffer (150 mM of NaCl, 5.2 mM of KCl, 2.2 mM of $CaCl_2 \cdot 2H_2O$, 0.2 mM of $MgCl_2 \cdot 6H_2O$, 6 mM of $NaHCO_3$, 2.8 mM of D-glucose, 5 mM of HEPES, pH 7.4)) to remove the unbound antibodies and to match the local refractive index in the vicinity of the waveguides for both arms. After this last step the functionalized sensors became ready to use.

2.1.3. Measurement with the Device

Once the sensor fabrication and functionalization had been completed, the biosensor was prepared for measurements. The construction of the sensor, the techniques of the measuring light coupling, the bias point tuning, and the output signal transmission apparatus were employed from our previous work [13]. As a light source a visible red laser diode (658 nm, 100 mW, RLT650-100MGS, Roithner Lasertechnik GmbH, Vienna, Austria) was used. The continuous flow of the samples was performed the same way as during the functionalization step. The schematic representation of the experimental setup and the integrated optical MZI sensor can be seen in Figure 2.
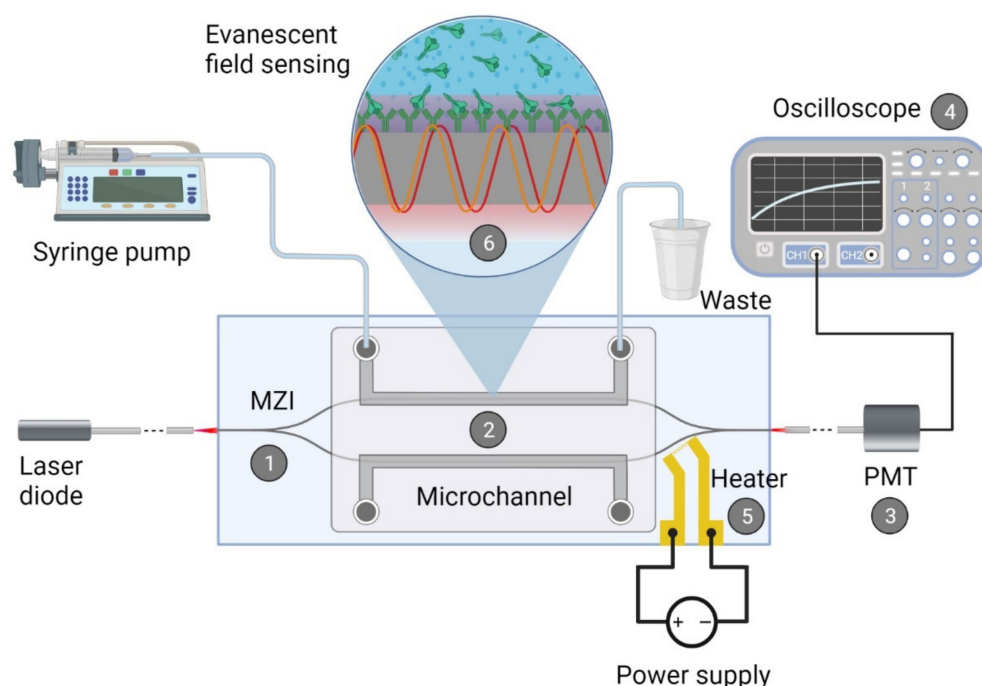
Figure 2. Schematic representation of the biosensor device: the integrated optical Mach–Zehnder interferometer (MZI) for sensing the analyte (1), the microfluidic apparatus (syringe pump, tubes, PDMS microchannel) for fluid sample providing (2), the signal processing unit, namely a photomultiplier tubes (PMT) detector (3) with an oscilloscope (4), the microheater structure for bias point tuning (5). The working principle of the device is also presented: the evanescent field detection is based on the phase difference in the propagating light of the measuring arm (yellow waves) compared to the ones of the reference arm (red waves) (6). Phase difference can be induced by the binding of the target spike protein S1 subunit to the antibody-covered surface of the measuring arm. The figure was created with BioRender.com.

Prior to the measurements, higher and lower flow rates were applied for filling up the microchannels with the buffer or target protein solutions (30 μL/min and 3 μL/min, respectively). As a starting point of the experiments, the bias point of the integrated optical MZI was adjusted, as has been described previously in detail [22]. To obtain valid detection results by the interferometer, the signal levels and the phase-shifting effect of the microheater at a given applied voltage were set (Figure S1); therefore, output signals obtained from distinct sensors possessing slightly different sensitivities are comparable. The reason behind this lies in the differences in light coupling efficiencies and waveguide structure finesse of such devices. For setting the bias point of the sensor response to the inflexion point on the transmission function, typically 1.0–1.5 V was applied. The adverse effects of bias point drifting on the signal response show the importance of the bias calibration (Figure S2). During this study, the baseline could be kept stable with negligible drift during the measurements on the time scale of several minutes, by using the local heating technique. The results obtained with this experimental setup were analyzed and plotted by MATLAB 2020b software (MathWorks, Natick, MA, USA).

2.2. Cell Culture Models and Barrier Integrity Measurements

2.2.1. Cell Culture Models of Biological Barriers

To examine the passage of the spike protein S1 subunit across the BBB we assembled a co-culture model, which consists of human endothelial cells (hEC) and bovine brain pericytes [25,26]. hECs are derived from human umbilical cord blood stem cells and cultured as described previously. Procedure of blood collection was approved by the French Ministry of Higher Education and Research (CODECOH Number DC2011-1321).

Informed consent was obtained from the infants' parents (Béthune Maternity Hospital, Béthune, France). The study was conducted according to the World Medical Association Declaration of Helsinki. hECs arrived at our laboratory at passage number 5 and were grown on 0.2% gelatin (Sigma, part of the Merck Group, Darmstadt, Germany)-coated cell culture dishes (Corning Costar; Corning, NY, USA) and were used at passage number 7 in all experiments. hECs were kept in endothelial cell culture medium (ECM, ScienCell, Carlsbad, CA, USA) supplemented with 5% fetal bovine serum (FBS; Sigma), 1% endothelial cell growth supplement (ECGS, ScienCell) and gentamycin (Sigma, 50 µg/mL). Bovine brain pericytes were cultured on 0.2% gelatin -oated dishes (Corning Costar) in Dulbecco's modified Eagle's medium (DMEM, Life Technologies, Thermo Fisher Scientific, Waltham, MA, USA) supplemented with 20% FBS (Sigma), 1% Glutamax (Life Technologies Co., Carlsbad, CA, USA) and gentamicin (50 µg/mL). For both cells when cultures reached confluency, cells were gently trypsinized until cells rounded up, trypsin was removed, and cells were collected and counted in hEC culture medium. To assemble the BBB co-culture model cell culture inserts (Millicell Millipore, MCSP24H48, PET, 3 µm pore size, 24-well format) were coated with a 1:48 ratio of growth factor-reduced Matrigel (Corning) in DMEM in the top compartment (1 h, room temperature). The lower side of the membrane was coated with 0.2% gelatin (20 min, 37 °C). Inserts were dried, and then pericytes were seeded to the bottom of the inserts at a cell number of 5×10^3 cells/insert. Cells were left to adhere for two hours, and then the insert was turned into a 24-well plate (Greiner, Kremsmünster, Austria), and hECs were seeded into the Matrigel-coated top compartment at a cell number of 1.3×10^4 cells/insert. Cells were kept in a co-culture for 4 days while they were fed every 2 days.

To test the passage of the spike protein S1 subunit on an alternative biological barrier, we established an in vitro model of the intestinal barrier using the human Caco-2 intestinal epithelial cell line (ATCC cat. No. HTB-37; Manassas, VA, USA). Caco-2 cells were cultured in DMEM with stable glutamine (Life Technologies) supplemented with 10% FBS (PAN-Biotech GmbH, Aidenbach, Germany) and gentamicin (50 µg/mL). All plastic culture surfaces were coated with 0.05% collagen type I in sterile distilled water. To establish the epithelial barrier model cell culture inserts (Millicell Millipore, MCSP24H48, PET, 3 µm pore size, 24-well format) were coated with collagen type I, and 3×10^4 Caco-2 cells/insert were seeded. Cells were kept on the inserts for 10–12 days and were fed every two days.

2.2.2. Transendothelial Electrical Resistance Measurement

To follow the development of barrier properties on both in vitro models, transendothelial electrical resistance (TEER) was registered every second day before medium change. Plates containing the cells were kept on a heating pad set to 37 °C during the measurement to avoid any fluctuation in the values. For the TEER measurement an EVOM Volt/Ohm Meter with a 24-well cup chamber setup was used (ENDOHM-6G; World Precision Instruments, Sarasota, FL, USA). TEER values were calculated with the subtraction of the background of cell-free inserts ($60\ \Omega\ cm^2$) relative to the surface of the cell culture insert ($0.33\ cm^2$) and corrected to the shunt resistance of the insert as described before [27]. TEER values were therefore expressed in ($\Omega\ cm^2$).

2.3. Spike Protein S1 Subunit Permeability Assays

To examine whether the SARS-CoV-2 spike protein S1 subunit (Genscript, Z03501-100, Piscataway, NJ, USA) crosses the BBB and the intestinal epithelial barrier we established these two models on cell culture inserts as described above. When the TEER reached $34.6 \pm 1.9\ \Omega\ cm^2$ for the BBB model and $367.76 \pm 36.8\ \Omega\ cm^2$ for the Caco-2 model, cells were used in the experiments. Passage of spike protein from the top compartment to the bottom compartment of the cell culture inserts was performed in a 0.1% BSA-RH buffer. BSA was present in all samples to avoid attachment of the spike protein to the plastic surfaces. Microcentrifuge tubes and plate wells were also pre-incubated with 0.1% BSA-RH to avoid attachment of the spike protein. During the experiment low-bind pipette tips were

used. SARS-CoV-2 spike protein was added to the top compartment of the cell culture inserts (200 μg/mL, 70 μL), while the bottom compartment contained 530 μL low-bind pipette tips buffer. To minimize any unstirred water layer on the surface of the cell layers the plates were kept on a horizontal shaker (150 rpm, Biosan, Riga, Latvia) during the 30 min permeability period. Control cells received only 0.1% BSA-RH buffer. The passage of the SARS-CoV-2 spike protein S1 subunit was also tested on cell-free inserts. Directly after the assay TEER was measured on all inserts and samples were collected from both the top and the bottom compartments and used for the biosensing and ELISA experiments. Permeability assay with fluorescent markers to verify barrier integrity was also performed on control cultures (for protocol and results see Supplementary Material).

2.4. Determination of the Passage of SARS-CoV-2 Spike Protein S1 Subunit across Biological Barriers with Elisa

In addition to the biosensing method we validated the passage of the spike protein S1 subunit across the BBB and the intestinal barrier with a traditional method. For this we developed an ELISA, similarly as described previously [28]. All steps were performed at room temperature unless otherwise indicated. Between most incubations a washing step with a wash buffer (TBS buffer and BSA, 10 mM of TRIS-HCl, 150 mM of NaCl and 0.5% BSA at pH = 7.4) was performed. First Nunc MaxiSorp flat-bottom plates (Life Technologies) were pre-treated with a 10% AnteoBind Biosensor solution (AnteoTech Ltd., Brisbane, Australia) for 30 min, then this solution was removed, and plates were dried under laminar flow. Dilution series from the SARS-CoV-2 spike protein stock was prepared between concentrations of 0–20 μg/mL in carbonate buffer (45.3 mM of $NaHCO_3$ and 18.2 mM of Na_2CO_3 in distilled water, pH = 9.6). Besides the dilution series, samples from the bottom compartments of spike protein treated and control inserts (50 μL/well) were also added to the plate in triplicates and were incubated overnight at 4 °C. The next day, wells were blocked with 1% BSA-5% normal goat serum in TBS buffer for 2 h. After this step the primary antibody (MonoRab SARS-CoV-2 Neutralizing Antibody (BS-R2B2), 1 μg/mL, Genscript, A02051) was added to all wells and was incubated for 2 h followed by the biotin conjugated goat anti-rabbit secondary antibody (0.3 μg/mL, Vector Laboratories Ltd., Burlingame, CA, USA, antibody ID: AB_2313606) for 1 h. To finish the ELISA extravidin peroxidase (0.5 μg/mL, Vector Laboratories Ltd.) was added to each well for 30 min. ELISA substrate tablets containing o-phenylenediamine dihydrochloride (OPD, Life Technologies) were dissolved in 10 mL of citrate buffer (63 mM of $Na_2HPO_4 \cdot 2H_2O$, 26.6 mM of citric acid in distilled water, pH = 6) and mixed with 3% H_2O_2 solution (25 μL). The substrate solution was pipetted to all wells in a 100 μL/well volume. Yellow color developed within 10 min. The reaction was stopped with 4 N H_2SO_4 (50 μL/well). Absorbance was detected with a multiwell plate reader (Fluostar Optima, BMG Labtech, Ortenberg, Germany) at 492 nm. Dilution series data were plotted, and spike protein concentration of each sample was determined based on the calibration curve of the assay (Figure S3).

2.5. Statistical Analysis

Data were plotted and analyzed using Excel software (Microsoft, Redmond, WA, USA) and GraphPad Prism 5.0 Software (GraphPad, San Diego, CA, USA). Data are presented as means ± SEM, where relevant. Experiments were repeated at least twice.

3. Results

3.1. Measurement of the Passage of the SARS-CoV-2 Spike Protein S1 Subunit across Biological Barriers

3.1.1. Integrated Optical Interferometric Biosensor

The biosensor system was calibrated with control samples of two characteristic spike protein concentrations (2 and 20 μg/mL in 0.1% BSA-RH buffer, Figure 3). For the detection of the target spike protein S1 subunit, samples from the bottom compartments of the permeability assays across the BBB and Caco-2 models were introduced into the measuring

arm of the MZI sensor. The upper or the lower arm of the interferometer was referred to as the measuring arm, while the other one remained intact. After each measurement, the corresponding microchannel was leached out with the buffer and could serve as a reference arm for further measurements with the same sensor. Note that as an intrinsic feature of such interferometric detection, the sign of the obtained signal depended on which branch of the interferometer was used as a measuring arm (Figure S4). For the sake of easier comparison, signals are always shown with positive sign. Figure 3 shows the results obtained from the detection of the different solutions: 0.1% BSA-RH buffer, calibration solutions, and samples from permeability assays on both barrier cell culture models and cell-free inserts.
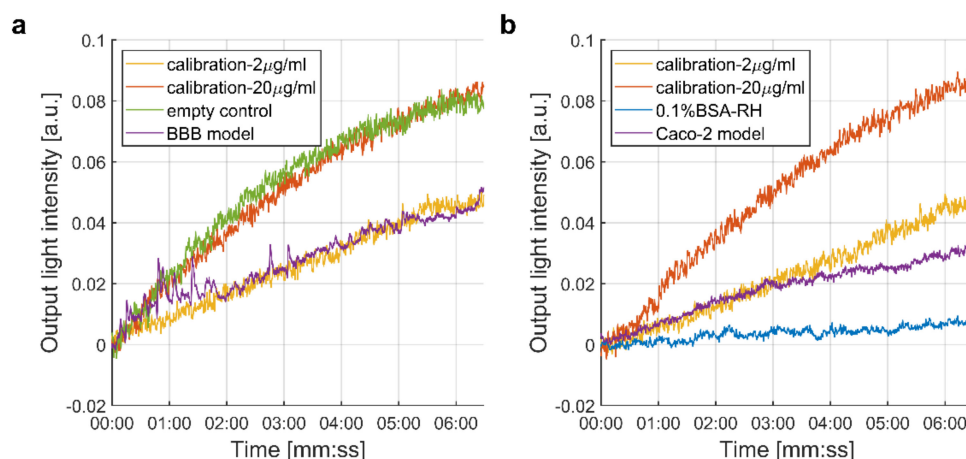

Figure 3. Results of the interferometric biosensing by the integrated optical MZI sensor. Both graphs show the signals detected after the introduction of the calibration samples (2 and 20 µg/mL). (**a**) Results obtained from samples after the passage of the spike protein S1 subunit across cell-free cell culture inserts and the BBB model. (**b**) Signals detected from buffer (0.1% BSA-RH) or samples after the permeability of the spike protein through the Caco-2 monolayer.

The control buffer solution lacking the target protein (Figure 3b: 0.1% BSA-RH) evoked no significant change in the output intensity, and these signals were measured as a background. Calibration samples with 2 and 20 µg/mL protein concentrations showed suitable signals to compare them to samples obtained from the permeability assays (Figure 3b). In case of the cell-free cell culture inserts (Figure 3a: empty control), we observed a similar signal amplitude as for the calibration sample 20 µg/mL. The evaluated protein concentrations of the target solutions, on the other hand, were different for the two barrier models. In case of the BBB model, the signal obtained with the biosensor was close to the signal of the 2 µg/mL calibration concentration; however, in the case of the Caco-2 layer, the signal was lower, in line with findings of the control ELISA experiments (see under Section 3.1.2).

3.1.2. ELISA Experiments

To validate the results obtained by the biosensing method, we also developed a more traditional ELISA for the detection of the spike protein S1 subunit crossing the BBB and intestinal barrier models. After the spike protein passage assay, TEER was measured, and samples from the bottom compartments of all inserts were collected and used in the biosensing measurements and for the ELISA.

First, we could conclude that the treatment with 200 µg/mL of SARS-CoV-2 spike protein did not change the TEER of the cultures compared to the control group, which only received the 0.1% BSA-RH buffer (Figure 4a). Permeability for fluorescent markers across control groups also showed a tight barrier for both models (Figure S5). We found, that during our measurements the spike protein S1 subunit crossed cell-free inserts effectively. In the ELISA, spike protein passage was found for brain endothelial monolayers, while the

signal measured for the intestinal barrier system was under the detection limit (Figure 4b). These results corroborate the findings of the MZI measurements.
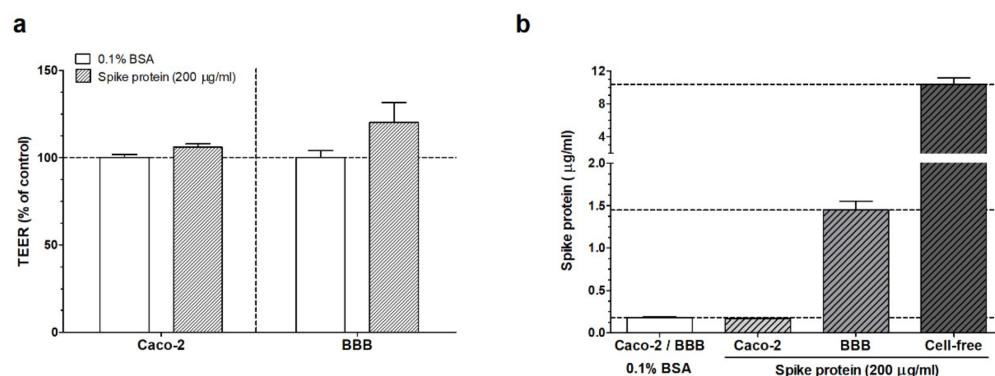

Figure 4. (**a**) Results of the transendothelial–transepithelial electrical resistance (TEER) measurement after SARS-CoV-2 spike protein (200 µg/mL) treatment in 0.1% bovine serum albumin (BSA)–Ringer–HEPES buffer or only after buffer treatment (0.1% BSA). (**b**) Detection of spike protein S1 subunit by ELISA in samples from the bottom compartment of cell culture inserts after spike protein treatment (200 µg/mL, 30 min). We also indicate results for inserts, which received only the carrier buffer (0.1% BSA) or the results of passage of spike protein across cell-free inserts. Caco-2: human intestinal epithelial cells. BBB: blood–brain barrier model.

4. Discussion

In this study, we investigated the penetration of the well-known surface spike protein S1 subunit of the worldwide pandemic causing SARS-CoV-2 coronavirus through the BBB and the intestinal epithelial barrier systems. The detection of the target spike S1 protein was performed with a portable optical biosensor with rapid interferometric detection as a sensitive technique using an integrated optical Mach–Zehnder device. The results were validated with a traditional ELISA measurement.

4.1. Interaction of SARS-CoV-2 and Spike Protein S1 Subunit with Biological Barriers

Here we investigated the passage of the SARS-CoV-2 spike protein S1 subunit across a human brain endothelial cell-based culture BBB model for the first time. Previously it was shown that spike protein treatment alters barrier integrity and induces the activation of endothelial cells [29,30]. During our investigation short-term spike protein S1 subunit treatment did not change the resistance of the BBB model.

The mechanism of virus or viral protein passage across the BBB or epithelial barriers has been studied before and therefore was not in the focus of the current study. Recently it has been found that SARS-CoV-2 crosses mouse and hamster primary brain endothelial cell culture models by a transcellular pathway without changing tight junction expression [31]. It was suggested that S1 subunit crosses the BBB via adsorptive-mediated transcytosis in mice [13], whereas ACE2 receptors were also found to be important in brain uptake in mice [13]. We previously found that the hECs used in the present model [25] express ACE2 only in a very low amount [26]. An extensive review of the SARS-CoV-2 virus and spike protein interactions and alternative passage mechanisms across the BBB was published [32].

Since gastrointestinal symptoms are also observed in COVID-19 we introduced an intestinal barrier culture system to our experimental setup. We found that TEER had not changed after short-term treatment with the spike protein in this epithelial model. In the biosensor measurement we detected the passage of the spike protein across this barrier, which was lower compared to the BBB model's permeability. Previously it was shown that the Caco-2 cells express the ACE2 receptor, which makes them an appropriate model to study the spike protein passage [33]. The observed difference in the spike protein S1 subunit passage for this culture model could be due to, on the one hand, the basal TEER values, and on the other hand, the distinct receptor expression and alternative routes of passage in

epithelial cells. Our study may provide a deeper insight in the barrier function alterations and a quantitative verification of the spike protein penetration across the biological barriers.

4.2. Integrated Optical MZI Biosensor

The application of the optical biosensor construction as a sensitive, rapid, and portable way of detecting the target spike protein from fluid samples is one of the strengths of this study. Investigations focusing on the early, effective detection of the virus and its antigens have been in the center of attention [34]. By this label-free, cost-effective approach, the evaluation of the spike protein S1 subunit concentration could be achieved within few minutes. This biosensing approach allowed the investigation of human cell culture model systems of biological barriers. To evaluate the accurate spike protein concentration of the fluid samples, we assumed that the response function of our biosensor followed the Freundlich isotherm, a typical equation valid for a wide range of physical adsorption processes from solutions [35]:

$$log(m_{ad}) = K + (1/n) \cdot logC \qquad (1)$$

where m_{ad} and C are the relative adsorbed mass and the bulk concentration of the analyte, while K and n are constants at the given temperature. From the calibration curves measured at the preadjusted concentrations, $K = 0.3653$ and $n = 3.3219$ were obtained, if m_{ad} and C are measured in units given in Figure 3. Using these calibration values, the concentration of the spike protein S1 subunit that crossed the intestinal barrier (Caco-2 cells) was found to be approximately 0.5 µg/mL.

These results show the applicability of this optical biosensing technique for the detection of SARS-CoV-2 surface spike proteins. Such an interferometric, sensing approach is also represented in an ongoing, EU-funded (European Commission), large research project (CoNVat) tackling the COVID-19 pandemic. In that project, a silicone bimodal interferometric sensor is being employed and developed for the detection of the intact virus from nasopharyngeal and saliva samples, as a point-of-care testing device [21,36]. Moreover, various silicone interferometric biosensors have been used for diagnostic purposes for small-molecule [37], protein, glycolipid [38] and nucleic acid detection in the aM-fM range [21,39].

Our results and the above-mentioned studies clearly implicate that integrated optical biosensor platforms have the capability of sensing the spike protein in a scenario of human biological barrier penetration studies. The investigation of BBB models is crucial to understand the neuroinvading consequence of spike protein exposure, the development of neurological anomalies [29]. Therefore, these cell culture studies could be useful model systems for further experiments aiming at the mechanisms of spike protein-associated pathologies.

4.3. ELISA

The results obtained by the biosensor measurements were also validated by the ELISA. We observed that spike protein S1 subunit concentrations detected by the ELISA were very similar to the biosensor measurements in the case of the BBB model. This corroborates the results we obtained with both methods. The spike protein passage across the Caco-2 intestinal epithelial cell monolayer was in the detection limit range during the MZI measurements, but it was not detectable by the ELISA. We hypothesize that this occurred due to the different sensitivity of the methods, and we reached the lower detection limit in the ELISA earlier than in the biosensor device. This sensitivity difference was also visible close to the upper detection limit when we measured the passage of the spike protein across the cell-free cell culture inserts.

5. Conclusions

This study was focused on a basic evaluation of the barrier penetration capability of the SARS-CoV-2 surface spike protein S1 subunit across two barrier model systems of

human organs highly exposed to coronavirus infection. Cell culture systems of the BBB and the intestinal barriers were investigated in this context. Based on the results of the optical biosensing and immunoassay approaches, it was established that spike protein S1 subunit could cross both cell culture models of the barriers but in different amounts. These results and the established models and methods could be valuable for further studies on the pathological effects of SARS-CoV-2 related to the human body.

Supplementary Materials: The following are available online at https://www.mdpi.com/article/10.3390/biomedicines10010188/s1, Methods: description of barrier integrity permeability studies. Figure S1: The demonstration of the bias point calibration process with the Mach–Zehnder interferometer (MZI) output intensity values during the biasing process and during the measurement. Figure S2: Sinusoidal transmission function curve of the Mach–Zehnder interferometer with the highlighted, ideal inflexion points for biasing on it in a function of the applied voltage, applied for the thermal phase shifting ($U_{\pi/2}$, U_π, $U_{3\pi/2}$ etc.). Figure S3: ELISA calibration. Figure S4: Demonstration of the intrinsic feature of such interferometric detection. Figure S5: Permeability of the Caco-2 intestinal barrier culture monolayer and the human endothelial cell (hEC)-pericyte blood–brain barrier co-culture model.

Author Contributions: A.D. and M.A.D. created the research idea. The MZI biosensor was prepared by D.P. The optical biosensor measuring setup was designed and built by S.V., D.P. and A.D. The BBB and the Caco-2 cell culture model assays were prepared by J.P.V., A.K. and F.R.W. The calibration and control samples were prepared by J.P.V. and F.R.W. The barrier integrity, spike protein permeability, and ELISAs were performed by J.P.V., A.K., F.R.W. and M.A.D. The measurements with the biosensor were carried out by D.P., S.V. and A.D. The quantitative evaluation of the measurements with the biosensor system was performed by D.P. The results obtained with the barrier integrity, spike protein permeability, and ELISAs were evaluated by J.P.V., A.K. and F.R.W. The original draft of the manuscript was written by D.P., F.R.W. and A.D. Manuscript review and editing was performed by M.A.D. Supervision and funding were provided by A.D. and M.A.D. All authors have read and agreed to the published version of the manuscript.

Institutional Review Board Statement: hECs are derived from human umbilical cord blood stem cells. Procedure of blood collection was approved by the French Ministry of Higher Education and Research (CODECOH Number DC2011-1321).

Informed Consent Statement: Informed consent was obtained from the infants' parents (Béthune Maternity Hospital, Béthune, France). The study was conducted according to the World Medical Association Declaration of Helsinki.

Data Availability Statement: The original data are available upon request from the corresponding author.

Conflicts of Interest: The authors declare no conflict of interest or state.

References

1. Gustafson, D.; Raju, S.; Wu, R.; Ching, C.; Veitch, S.; Rathnakumar, K.; Boudreau, E.; Howe, K.L.; Fish, J.E. Overcoming barriers: The endothelium as a linchpin of coronavirus disease 2019 pathogenesis? *Arterioscler. Thromb. Vasc. Biol.* **2020**, *40*, 1818–1829. [CrossRef] [PubMed]
2. Zhou, P.; Yang, X.L.; Wang, X.G.; Hu, B.; Zhang, L.; Zhang, W.; Si, H.R.; Zhu, Y.; Li, B.; Huang, C.L.; et al. A pneumonia outbreak associated with a new coronavirus of probable bat origin. *Nature* **2020**, *579*, 270–273. [CrossRef] [PubMed]
3. Biorender.com. Templates. Available online: https://app.biorender.com/biorender-templates (accessed on 30 November 2021).
4. De Sousa, A.K.; de Aguiar Magalhães, D.; dos Santos Ferreira, J.; dos Reis Barbosa, A.L. SARS-CoV-2-mediated encephalitis: Role of AT2R receptors in the blood-brain barrier. *Med. Hypotheses* **2020**, *144*, 110213. [CrossRef] [PubMed]

5. Schwabenland, M.; Salié, H.; Tanevski, J.; Killmer, S.; Lago, M.S.; Schlaak, A.E.; Mayer, L.; Matschke, J.; Püschel, K.; Fitzek, A.; et al. Deep spatial profiling of human COVID-19 brains reveals neuroinflammation with distinct microanatomical microglia-T-cell interactions. *Immunity* **2021**, *54*, 1594–1610.e11. [CrossRef] [PubMed]

6. Ogata, A.F.; Cheng, C.-A.; Desjardins, M.; Senussi, Y.; Sherman, A.C.; Powell, M.; Novack, L.; Von, S.; Li, X.; Baden, L.R.; et al. Circulating Severe Acute Respiratory Syndrome Coronavirus 2 (SARS-CoV-2) Vaccine Antigen Detected in the Plasma of mRNA-1273 Vaccine Recipients. *Clin. Infect. Dis.* **2021**, *2*, ciab465. [CrossRef]

7. Kiss, B.; Kis, Z.; Pályi, B.; Kellermayer, M.S.Z. Topography, Spike Dynamics, and Nanomechanics of Individual Native SARS-CoV-2 Virions. *Nano Lett.* **2021**, *21*, 2675–2680. [CrossRef]

8. Ogata, A.F.; Maley, A.M.; Wu, C.; Gilboa, T.; Norman, M.; Lazarovits, R.; Mao, C.-P.; Newton, G.; Chang, M.; Nguyen, K.; et al. Ultra-Sensitive Serial Profiling of SARS-CoV-2 Antigens and Antibodies in Plasma to Understand Disease Progression in COVID-19 Patients with Severe Disease. *Clin. Chem.* **2020**, *66*, 1562–1572. [CrossRef]

9. Zhang, S.; Liu, Y.; Wang, X.; Yang, L.; Li, H.; Wang, Y.; Liu, M.; Zhao, X.; Xie, Y.; Yang, Y.; et al. SARS-CoV-2 binds platelet ACE2 to enhance thrombosis in COVID-19. *J. Hematol. Oncol.* **2020**, *13*, 120. [CrossRef]

10. Greinacher, A.; Thiele, T.; Warkentin, T.E.; Weisser, K. A Prothrombotic Thrombocytopenic Disorder Resembling Heparin-Induced Thrombocytopenia Following Coronavirus-19 Vaccination. *Res. Sq.* **2021**. preprint.

11. Shirato, K.; Kizaki, T. SARS-CoV-2 spike protein S1 subunit induces pro-inflammatory responses via toll-like receptor 4 signaling in murine and human macrophages. *Heliyon* **2021**, *7*, e06187. [CrossRef]

12. Lei, Y.; Zhang, J.; Schiavon, C.R.; He, M.; Chen, L.; Shen, H.; Zhang, Y.; Yin, Q.; Cho, Y.; Andrade, L.; et al. SARS-CoV-2 Spike Protein Impairs Endothelial Function via Downregulation of ACE 2. *Circ. Res.* **2021**, *128*, 1323–1326. [CrossRef]

13. Rhea, E.M.; Logsdon, A.F.; Hansen, K.M.; Williams, L.M.; Reed, M.J.; Baumann, K.K.; Holden, S.J.; Raber, J.; Banks, W.A.; Erickson, M.A. The S1 protein of SARS-CoV-2 crosses the blood–brain barrier in mice. *Nat. Neurosci.* **2021**, *24*, 368–378. [CrossRef]

14. Zhong, J.F.; Weiner, L.P.; Burke, K.; Taylor, C.R. Viral RNA extraction for in-the-field analysis. *J. Virol. Methods* **2007**, *144*, 98–102. [CrossRef]

15. Asghari, A.; Wang, C.; Yoo, K.M.; Rostamian, A.; Xu, X.; Shin, J.-D.; Dalir, H.; Chen, R.T. Fast, accurate, point-of-care COVID-19 pandemic diagnosis enabled through advanced lab-on-chip optical biosensors: Opportunities and challenges. *Appl. Phys. Rev.* **2021**, *8*, 031313. [CrossRef]

16. Kaltenboeck, B.; Wang, C. Advances in Real-Time PCR: Application to Clinical Laboratory Diagnostics. In *Advances in Clinical Chemistry*; Academic Press: Cambridge, MA, USA, 2005; Volume 40, pp. 219–259. ISBN 0120103400.

17. Nagasse-Sugahara, T.K.; Kisielius, J.J.; Ueda-Ito, M.; Curti, S.P.; Figueiredo, C.A.; Cruz, Á.S.; Silva, M.M.J.; Ramos, C.H.; Silva, M.C.C.; Sakurai, T.; et al. Human vaccinia-like virus outbreaks in São Paulo and Goiás States, Brazil: Virus detection, isolation and identification. *Rev. Inst. Med. Trop. Sao Paulo* **2004**, *46*, 315–322. [CrossRef]

18. Gibbs, S.E.J.; Ellis, A.E.; Mead, D.G.; Allison, A.B.; Moulton, J.K.; Howerth, E.W.; Stallknecht, D.E. West Nile virus detection in the organs of naturally infected blue jays (*Cyanocitta cristata*). *J. Wildl. Dis.* **2005**, *41*, 354–362. [CrossRef]

19. Cheung, A.Y.; Wu, H. Overexpression of an Arabidopsis Formin Stimulates Supernumerary Actin Cable Formation from Pollen Tube Cell Membrane. *Plant Cell* **2004**, *16*, 257. [CrossRef]

20. Nguyen, H.H.; Park, J.; Kang, S.; Kim, M. Surface plasmon resonance: A versatile technique for biosensor applications. *Sensors* **2015**, *15*, 10481–10510. [CrossRef]

21. Soler, M.; Estevez, M.C.; Cardenosa-Rubio, M.; Astua, A.; Lechuga, L.M. How Nanophotonic Label-Free Biosensors Can Contribute to Rapid and Massive Diagnostics of Respiratory Virus Infections: COVID-19 Case. *ACS Sens.* **2020**, *5*, 2663–2678. [CrossRef]

22. Petrovszki, D.; Krekic, S.; Valkai, S.; Heiner, Z.; Dér, A. All-Optical Switching Demonstrated with Photoactive Yellow Protein Films. *Biosensors* **2021**, *11*, 432. [CrossRef]

23. Petrovszki, D.; Valkai, S.; Gora, E.; Tanner, M.; Bányai, A.; Fürjes, P.; Dér, A. An integrated electro-optical biosensor system for rapid, low-cost detection of bacteria. *Microelectron. Eng.* **2021**, *239–240*, 111523. [CrossRef]

24. Mathesz, A.; Valkai, S.; Újvárosy, A.; Aekbote, B.; Sipos, O.; Stercz, B.; Kocsis, B.; Szabó, D.; Dér, A. Integrated optical biosensor for rapid detection of bacteria. *Optofluid. Microfluid. Nanofluid.* **2015**, *2*, 15. [CrossRef]

25. Cecchelli, R.; Aday, S.; Sevin, E.; Almeida, C.; Culot, M.; Dehouck, L.; Coisne, C.; Engelhardt, B.; Dehouck, M.P.; Ferreira, L. A stable and reproducible human blood-brain barrier model derived from hematopoietic stem cells. *PLoS ONE* **2014**, *9*, e99733. [CrossRef]

26. Santa-Maria, A.R.; Walter, F.R.; Figueiredo, R.; Kincses, A.; Vigh, J.P.; Heymans, M.; Culot, M.; Winter, P.; Gosselet, F.; Dér, A.; et al. Flow induces barrier and glycocalyx-related genes and negative surface charge in a lab-on-a-chip human blood-brain barrier model. *J. Cereb. Blood Flow Metab.* **2021**, *41*, 0271678X21992638. [CrossRef]

27. Vigh, J.P.; Kincses, A.; Ozgür, B.; Walter, F.R.; Santa-Maria, A.R.; Valkai, S.; Vastag, M.; Neuhaus, W.; Brodin, B.; Dér, A.; et al. Transendothelial Electrical Resistance Measurement across the Blood–Brain Barrier: A Critical Review of Methods. *Micromachines* **2021**, *12*, 685. [CrossRef]

28. Sipos, E.; Kurunczi, A.; Fehér, A.; Penke, Z.; Fülöp, L.; Kasza, Á.; Horváth, J.; Horvát, S.; Veszelka, S.; Balogh, G.; et al. Intranasal delivery of human β-amyloid peptide in rats: Effective brain targeting. *Cell. Mol. Neurobiol.* **2010**, *30*, 405–413. [CrossRef]

29. Buzhdygan, T.P.; DeOre, B.J.; Baldwin-Leclair, A.; Bullock, T.A.; McGary, H.M.; Khan, J.A.; Razmpour, R.; Hale, J.F.; Galie, P.A.; Potula, R.; et al. The SARS-CoV-2 spike protein alters barrier function in 2D static and 3D microfluidic in-vitro models of the human blood–brain barrier. *Neurobiol. Dis.* **2020**, *146*, 105131. [CrossRef]

30. DeOre, B.J.; Tran, K.A.; Andrews, A.M.; Ramirez, S.H.; Galie, P.A. SARS-CoV-2 Spike Protein Disrupts Blood–Brain Barrier Integrity via RhoA Activation. *J. Neuroimmune Pharmacol.* **2021**, *16*, 722–728. [CrossRef] [PubMed]

31. Zhang, L.; Zhou, L.; Bao, L.; Liu, J.; Zhu, H.; Lv, Q.; Liu, R.; Chen, W.; Tong, W.; Wei, Q.; et al. SARS-CoV-2 crosses the blood–brain barrier accompanied with basement membrane disruption without tight junctions alteration. *Signal Transduct. Target. Ther.* **2021**, *6*, 337. [CrossRef] [PubMed]

32. Erickson, M.A.; Rhea, E.M.; Knopp, R.C.; Banks, W.A. Interactions of SARS-CoV-2 with the Blood–Brain Barrier. *Int. J. Mol. Sci.* **2021**, *22*, 2681. [CrossRef] [PubMed]

33. Knyazev, E.; Nersisyan, S.; Tonevitsky, A. Endocytosis and Transcytosis of SARS-CoV-2 across the Intestinal Epithelium and Other Tissue Barriers. *Front. Immunol.* **2021**, *12*, 3639. [CrossRef]

34. Singh, V.; Allawadhi, P.; Khurana, A.; Banothu, A.K.; Bharani, K.K. Critical neurological features of COVID-19: Role of imaging methods and biosensors for effective diagnosis. *Sens. Int.* **2021**, *2*, 100098. [CrossRef]

35. Freundlich, H. Uber die adsorption in Losungen. *Z. Phys. Chem.* **1906**, *57*, 385–470. [CrossRef]

36. Combating 2019-nCoV: Advanced Nanobiosensing Platforms for POC Global Diagnostics and Surveillance | CoNVat Project | H2020 | CORDIS | European Commission. Available online: https://cordis.europa.eu/project/id/101003544 (accessed on 28 November 2021).

37. Chocarro-Ruiz, B.; Fernández-Gavela, A.; Herranz, S.; Lechuga, L.M. Nanophotonic label-free biosensors for environmental monitoring. *Curr. Opin. Biotechnol.* **2017**, *45*, 175–183. [CrossRef]

38. Ramirez-Priego, P.; Martens, D.; Elamin, A.A.; Soetaert, P.; Van Roy, W.; Vos, R.; Anton, B.; Bockstaele, R.; Becker, H.; Singh, M.; et al. Label-Free and Real-Time Detection of Tuberculosis in Human Urine Samples Using a Nanophotonic Point-of-Care Platform. *ACS Sens.* **2018**, *3*, 2079–2086. [CrossRef]

39. Huertas, C.S.; Fariña, D.; Lechuga, L.M. Direct and Label-Free Quantification of Micro-RNA-181a at Attomolar Level in Complex Media Using a Nanophotonic Biosensor. *ACS Sens.* **2016**, *1*, 162. [CrossRef]